Title
The Electron-Phonon Interaction from First Principles

Author
Noffsinger, Jesse Dean

Publication Date
2011

The Electron-Phonon Interaction from First Principles

by

Jesse Dean Noffsinger

A dissertation submitted in partial satisfaction of the
requirements for the degree of
Doctor of Philosophy
in
Physics
in the
Graduate Division
of the
University of California, Berkeley

Committee in charge:

Professor Marvin L. Cohen, Chair
Professor John Clarke
Professor Norman Phillips

Spring 2011

The Electron-Phonon Interaction from First Principles

Abstract

The Electron-Phonon Interaction from First Principles

by

Jesse Dean Noffsinger

Doctor of Philosophy in Physics

University of California, Berkeley

Professor Marvin L. Cohen, Chair

In this thesis the ground state electronic properties, lattice dynamics, electron-phonon coupling and superconductivity of a variety materials are investigated from first principles. The first chapter provides an introduction to the material and concepts of this thesis as well as motivation for the work done herein. Additionally, an overview is given on the theoretical background governing the calculations of this work. This includes overviews of the topics of density functional theory, the pseudopotential approximation, density functional perturbation theory, and applications of these approaches to the calculations of superconductivity. In the second chapter the mechanics of actually performing calculations within the methodology of chapter one are explained. This is accomplished through a detailed description of the computer software `EPW`. This software has been developed to allow computationally efficient approaches for calculating the electron-phonon interaction. A description of the software package, the particular quantities which it calculates and example calculations are given. The following two chapters present the results of calculations regarding electron-phonon coupling and superconductivity in bulk carbon compounds. The occurrence or absence of superconductivity is found to be related in these compounds to Fermi surface nesting and carrier concentrations. In chapter five we investigate the role of the fluorine dopant in the recently discovered (1111) Fe-pnictide superconductors. Contrary to the results of the literature published shortly after the discovery of these compounds, the presence of the dopant is found to actually result in a net *decrease* in the electron concentration on the Fe-plane within the local density approximation to density functional theory. In the two chapters which follow, we investigate the limits of two dimensional superconductivity in the recent experiments on ultra-thin Pb samples. Chapter six details calculations on freestanding Pb slabs constructed as thin as two monolayers. A useful formula predicting the electron-coupling strength and therefore estimating the superconducting transition temperature is developed. While in the next section a superconducting system is investigated wherein the important Pb-Si(111) interaction in ultra-thin Pb layers is taken into account. The observed superconductivity is explained by electron-phonon coupling and isotropic Migdal-Eliashberg theory. The observance of superconductivity in the nearly two-dimensional material is shown not to conflict with the predictions of the Mermin-Wagner theorem. In the final chapter, the phonon-assisted absorption of bulk silicon is calculated from first-principles. The calculated results are found to be in excellent agreement with experiment, and lead the way for the possibility of many first-principle studies on phonon-assisted optical processes in important technological devices.

To my wife,

for all of her love and support.

Contents

List of Figures

List of Tables

Acknowledgments

First and foremost, I would like to thank my thesis advisor, Prof. Marvin L. Cohen. His wisdom and guidance throughout my time as a graduate student has proved invaluable. Having a mentor who truly has had my best interests in mind has made all the difference in my life.

To Feliciano Giustino, who taught me nearly everything I know about the nitty-gritty of computational physics, and brought a gust of fresh air to the fifth floor of Birge Hall.

Additionally, I'd like to thank all of the graduate students and post-doctoral fellows who devoted long hours explaining to me the minutia which has been so important to my understanding of condensed matter physics. I fear that if I attempt to give credit by name to everyone who deserves my thanks that I will inevitably neglect important people.

Chapter 1

Introduction and Theory

1.1 Overview

This thesis describes work done in the field of computational condensed matter physics. In general, first-principles calculations aim to provide insight by computing physical properties of materials usign only the chemical or atomic configurations as inputs. Through the use of modern computers, many quantum mechanical problems which require a vast amount of computational power are now tractable. However, despite having an analytic form for the interactions between electrons and nuclei, the computation of emergent behavior in complex systems has remained a difficult task. Because a bulk system contains an extremely large number of electrons and atomic cores, the number of degrees of freedom necessary to describe such a system are far too large to solve the many-particle Schrodinger equation. While first-principles calculations performed without any simplifying approximations are still beyond the abililty of current computational physics, with the use of a few important physical approximations computational physicists are able to arrive at satisfying results to many interesting problems.

The electron-phonon interaction is responsible for many observed phenomena such as Peirls instability, the Kohn effect, temperature dependent electrical resisitivity as well as conventional superconductivity. Traditionally, the calculation of the electron-phonon interaction from first principles has been extremely computationally expensive and often impractical for some materials. While indirect measurements of the electron-phonon interaction are sometimes available through, for example, angle-resolved photoemission spectra, precise computation has been challenging. Recent developments have lead to the ability to more accurately and efficiently calculate the electron-phonon interaction. These developments include the supported releases of software to calculate lattice dynamical properties as well as to obtain maximally-localized basis sets of Wannier functions. These have been combined within a framework, developed in the research groups of Marvin L. Cohen and Steven G. Louie in the Physics department at The University of California, Berkeley, to allow for the precise computation of the electron-phonon interaction in condensed matter systems.

Applications of density functional theory, maximally-localized Wannier functions, density functional perturbation theory and Migdal-Eliashberg theory are presented in the following chapters. A great deal of the time spent to complete the calculations of this thesis was spent on software developement. Specifically the software addition to the `Quantum ESPRESSO` package, `EPW`, was developed in conjunction with the theoretical calculations of this work. `EPW`, *the Electron-Phonon interaction through Wannier functions*, is described in Chapter 2 and presents a new, highly computationally efficient method for the calculation of electron-phonon related properties in solid state systems. In fact, the results of Chapters 3, 4, 6, 7 and 8 crucially depended upon the techniques developed to obtain the electron-phonon interaction via the localization of Wannier functions.

The following sections in this chapter are meant to give a general background to the methods utilized in this thesis. The sections in this chapter present a working overview of density functional theory, pseudopotentials, density functional perturbation theory, and superconductivity. Thorough coverage of the theoretical methods can be found in Refs. [1, 2, 3, 4, 5, 6, 7, 8, 9].

1.2 Density functional theory and pseudopotentials

Density functional theory (DFT) provides a practical framework within which it is possible to compute many properties of the complicated many-body systems examined in the field of solid state physics. The foundations of DFT were set forth in a pair of well-known papers; P. Hohenberg and W. Kohn [10] and W. Kohn and L. J. Sham [11]. These documents contain much of the formalism used in modern-day electronic structure calculations. The essential premise of DFT is that many interesting and important properties of a material are a function of only the ground state electronic density. The total energy is one such property of interest. Within this framework, details of the *extremely cumbersome* total many-body wavefunction are not computed. This fact, in and of itself, makes modern computations possible.

Before considering the simplifications which come with DFT, we look at the quantum mechanical problem of describing the electrons in a solid. In this case, we solve the Schrodinger equation (Eqn 1.1) to obtain the ground-state wavefunction.

$$\hat{H}\Psi = E\Psi \tag{1.1}$$

This wavefunction is the total wavefunction of the electrons in the system. It therefore contains large amounts of information through the electronic coordinates $\mathbf{r}_i$.

$$\Psi = \Psi(\mathbf{r}_1, \mathbf{r}_2, ...\mathbf{r}_2) \tag{1.2}$$

In atomic units, the Hamiltonian of the electrons in the presence of an external potential $V_{ext}(\mathbf{r})$ is given by Eqn 1.3.

$$\hat{H} = -\frac{1}{2}\sum_i \nabla_i^2 + \sum_i V_{ext}(\mathbf{r}_i) + \frac{1}{2}\sum_{i,j\neq i} \frac{1}{|\mathbf{r}_i - \mathbf{r}_j|} \tag{1.3}$$

Here the first term is the kinetic energy $\hat{T}$, the second is the energy arising from the interaction with the external potential $\hat{V}_{ext}$, and the final term is the Coulomb electron-electron interaction $\hat{V}_{ee}$.

Unfortunately, solving Eqn. 1.3 is not a tractable problem for nearly any condensed matter system. Instead, within DFT the problem is recast in terms of the total electronic density which is a sum over occupied states (Eqn 1.4).

$$n(\mathbf{r}) = \sum_{\sigma\mathbf{k}i} f(\epsilon_{\mathbf{k}i\sigma})|\psi_{\mathbf{k}i\sigma}(\mathbf{r})|^2 \tag{1.4}$$

The normalization condition in place to determine the chemical potential is such that the total integrated charge density is equal to the number of electrons in the system (Eqn. 1.5).

$$\int n(\mathbf{r})d\mathbf{r} = N \tag{1.5}$$

By describing a solid state system in terms of the electronic density we can replace the complicated many-body problem of interacting electrons with a different, simpler problem. The new problem yields a set of independent-particle equations for a non-interacting system where all of the complicated physics of the many-body interaction is taken into account through an exchange-correlation potential.

The exchange correlation potential is the functional derivative of the exchange correlation energy with respect to the electron density (Eqn. 1.6).

$$v_{xc} = \frac{\delta E_{xc}}{\delta n(\mathbf{r})} \tag{1.6}$$

This exchange-correlation energy is the sum of the electronic exchange energy and the correlation energy.

$$E_{xc}[n] = E_x[n] + E_c[n] \tag{1.7}$$

The Hartree energy $E_H[n]$ arising from the Coulomb self-interaction of the total charge density is given Eqn 1.8. Additionally, the Hartree potential is the variational derivative of this Hartree energy with respect to the charge density $v_H = \delta E_H/\delta n$.

$$E_H = \frac{1}{2}\int\int dr'dr\frac{n(r)n(r')}{|r-r'|} \tag{1.8}$$

Putting the above terms together along with the kinetic energy $T[n]$ and the energy arising from any external potential, the total Kohn-Sham energy functional of the charge density is then given by Eqn 1.9.

$$E_{KS}[n] = T[n] + E_H[n] + E_{xc}[n] + \int V_{ext}(\mathbf{r})n(\mathbf{r})d\mathbf{r} \tag{1.9}$$

The goal, then, is to determine the charge density configuration which minimizes the total energy. This charge density is determined self-consistently by solving for the system in the independent Kohn-Sham particle picture. The self-consistent approach can be realized through the Schrodinger-like Kohn-Sham equation (Eqn 1.10).

$$(H_{KS} - \epsilon_i)\psi_i(\mathbf{r}) = 0 \tag{1.10}$$

The form of the Hamiltonian is

$$H_{KS} = -\frac{1}{2}\nabla^2 + v_{xc}(\mathbf{r}) + v_H(\mathbf{r}) + v_{ext}(\mathbf{r}). \tag{1.11}$$

In Eqn 1.10 ϵ_i are the quasiparticle eigenvalues. The independent particle wavefunctions $\psi_i(\mathbf{r})$ are the eigenfunctions which satisfy Eqn 1.10. In practice these equations are solved self-consistently and numerically. In practice these calculations are performed using a particular basis set to describe the wavefunctions. A commonly utilized basis set is made up of plane-waves as in Eqn 1.12.

$$\psi(\mathbf{r}) = \sum_{\mathbf{G}} C_{\mathbf{G}} e^{i(\mathbf{G}\cdot\mathbf{r})} \tag{1.12}$$

The **G**-vectors used in this expansion are the Bloch-space reciprocal lattice vectors defined within a periodic system, while the $C_{\mathbf{G}}$ are the Fourier coefficients. This method allows the users a simple method of increasing the convergence of a numerical simulation by simply increasing the magnitude of the largest **G**-vectors used in constructing the wavefunctions.

Despite the successes of DFT, calculations which involve solving for the density comprised of all the electrons present in a system remain extremely cumbersome for a variety of reasons. As chemical elements become heavier the total number of closed-shell electrons bound to the ionic cores grows rapidly. These electrons near the nuclear core are generally bound at energy scales of tens of electron volts or more. Consequently they are very nearly unaffected by the dynamics of the valence electrons which determine most properties of interest in a solid. Additionally, as many calculations are performed with the electronic wavefunctions expressed within a planewave basis, the total number of planewaves necessary to describe a system depends upon the smallest length scale which must be described. The length scales of the wavefunctions of core elecrons are much shorter than those which compose e.g. the interatomic bonds. Therefore a computational tool which removes the need to describe core electrons will speed up electronic calculations to a great degree. The calculations of this thesis and nearly all modern *ab initio* calculations, the tool employed is the pseudopotential.

If we assume that the dynamics of the core and valence electrons are separate, we can solve the problem of the core electrons using the same core potential which is present in an isolated atom. The valence electrons are then left as the only particles of interest. This leaves only the valence electrons as of interest for electronic calculations. Within density functional theory, a self-consistent solution to the Kohn-Sham equation (Eqn 1.10) expressed in radial coordinates yields the angular momentum components of the desired pseudopotential. In Eqn 1.13, the effective single electron potential $V_{eff}(r)$ is the sum of the nuclear Coloumb potential, Hartree potential and exchange-correlation potential arising from the self-consistent core charge density.

$$\left(-\frac{1}{2}\frac{d^2}{dr^2} + \frac{l(l+1)}{2r^2} + V_{eff}[n(r)]\right) rR_{nl}(r) = \epsilon_{nl} rR_{nl}(r) \tag{1.13}$$

The radial component of the pseudo-wavefunction can be compared to the all-electron solutions. Outside of a cutoff radius, the wavefunctions should be identical.

$$R_{nl}^{all-electron}(r) = R_l^{pseudo} \qquad \text{when } r > r_{cutoff} \tag{1.14}$$

Besides matching perfectly outside of the cutoff radius, the electronic eigenvalues of the pseudo and all-electron wavefunctions are to be the same.

$$\epsilon_{nl}^{all-electron}(r) = \epsilon_l^{pseudo} \tag{1.15}$$

Additionally, R_l^{pseudo} should be nodeless. As the number of wavefunctions required to describe the valence state is reduced, there is no orthonormality condition which prevents a set of nodeless pseudo-wavefunctions from describing the electronic states.

In the case of the commonly used norm-conserving pseudopotential, one final constraint is placed upon the pseudized wavefunctions. The integrated charge inside the cutoff radius should be the same as the all-electron case. This constraint forces the pseudo-wavefunctions to be normalized, hence the label "norm-conserving pseudopotential." Developed relatively recently, ultra-soft pseudopotentials relax this final criteria. These particular pseudopotentials have the significant benefit of faster numerical convergence. This is a result of the ability to use a smaller basis set to construct the wavefunctions. As a trade-off to their convergence properties, software code developement which utilizes ultra-soft pseudopotentials is slightly more complicated as additional terms arising from the reduced core charge must be introduced to the matrix elements.

1.3 Density functional perturbation theory

Lattice vibrations are responsible for many observed phenomena such as the Raman spectra, neutron-diffraction data, specific heat, thermal conductivity, thermal expansion, and bear heavily on other phenomena such as conventional phonon-mediated superconductivity and finite temperature resistivity. Density functional perturbation theory (DFPT) is the state-of-the-art method for calculating lattice dynamics from first-principles in condensed matter systems.

Density functional perturbation theory is a method of applying linear perturbation theory within density functional theory. The aim of DFPT is to calculate the derivatives of the total energy within a system based upon a periodic perturbation of the crystal lattice. Possibly the greatest advantage of DFPT over other methods of calculating crystal vibrations such as the frozen-phonon method is that the perturbation may take on any wavevector. This freedom allows one to avoid the need of using cumbersome supercells to calculate phonon eigenfrequencies at arbitrary wavevectors.

The array of derivatives calculated through DFPT leads to a dynamical matrix which can be diagonalized to yield the phonon eigenfrequencies and eigenmodes. The central approximation which allows for the application of DFPT in materials is the *Born-Oppenheimer approximation*[12]. This approximation asserts that the motion of the electrons, because of their relatively light mass as compared to the nuclear cores, is rapid enough that from the standpoint of the electrons the atomic cores are stationary. Under this approximation, the total wavefunction of a system is then separable into the product of the electronic and nuclear parts (Eqn 1.16).

$$\Psi_{total}(\mathbf{r}_1, \mathbf{r}_2, .., \mathbf{r}_n, \mathbf{R}_1, \mathbf{R}_2, .., \mathbf{R}_m) = \psi_{electronic}(\mathbf{r}_1, \mathbf{r}_2, .., \mathbf{r}_n) \times \psi_{nuclear}(\mathbf{R}_1, \mathbf{R}_2, .., \mathbf{R}_m) \tag{1.16}$$

The electronic coordinates are denoted by $\mathbf{r}_i$ and the atomic coordinates $\mathbf{R}_j$. Therefore, as the atomic positions are methodically perturbed, the electronic ground state and total energy can be computed as a function of these perturbations.

To begin, the derivatives of the total energy with respect to the atomic positions are obtained through the Hellman-Feynman theorem and are given by Eqns. 1.17, 1.18 [13].

$$\frac{\partial E}{\partial R_j} = \int \frac{\partial V_{R_j}(r)}{\partial R_j} n_R(r) dr \tag{1.17}$$

$$\frac{\partial^2 E}{\partial R_i \partial R_j} = \int \frac{\partial^2 V_{R_j}(r)}{\partial R_i \partial R_j} n_{R_j}(r) dr + \int \frac{\partial n_R(r)}{\partial R_i} \frac{\partial V_R(r)}{\partial R_j} dr \tag{1.18}$$

The change in electron density with an atomic perturbation $\partial n/\partial R_i$ can be obtained by linearizing the equations of Section 1.2. The resulting Eqns. 1.19,1.20,1.21 are equivalent to the Kohn-Sham equations in a perturbed system. These equations, solved self-consistently, lead to the matrix of force constants known as the dynamical matirx.

$$\Delta n(r) = 4 \sum_n \psi_n^*(r) \Delta\psi_n(r) \tag{1.19}$$

$$(H_{SCF} - \epsilon_n)|\Delta\psi_n\rangle = -(\Delta V_{SCF} - \Delta\epsilon_n)|\psi_n\rangle \tag{1.20}$$

$$\Delta V_{SCF}(r) = \Delta V(r) + \frac{1}{2} \int \frac{\Delta n(r')}{|r - r'|} dr' + \frac{dv_{xc}(n)}{dn}|_{n=n(r)} \Delta n(r) \tag{1.21}$$

It is traditional to express the perturbation to a wavefunction $\Delta\psi_n(r)$ as a sum over all states of the system as in first order perturbation theory. However, a self-consistent solution to Eqns. 1.19, 1.20, and 1.21 requires knowledge only of the occupied states and therefore the computational cost of a perturbative step is similar to that of calculating the ground state charge density.

Once the variation of the density with respect to atomic perturbation has been calculated for the symmetry-reduced set of irreducible representations of the crystal in question, the dynamical matrix is constructed. The eigenfrequencies ω are then determined from the dynamical matrix by Eqn. 1.22. The eigenvectors of the dynamical matrix give the real-space motion of the atoms associated with a particular phonon wavevector and frequency.

$$\det \left| \frac{1}{\sqrt{M_I M_J}} \frac{\partial^2 E(R)}{\partial R_I \partial R_J} - \omega^2 \right| = 0 \tag{1.22}$$

An additional feature of DFPT is that the derivative of the self-consistent potential $V_{SCF}(r)$ with respect to a phonon perturbation is computed as a part of the protocol of a DFPT calculation. This perturbation is the integrand of the electron-phonon matrix elements $g^{\nu}_{mn}(k,q) = \langle \psi_{km} | \Delta V_{q\nu} | \psi_{k+q,n} \rangle$ which is central to the calculations of this thesis.

1.4 Electron-phonon Superconductivity

Since the observation of a vanishing resistivity in liquid-He cooled Hg by H. K. Onnes in 1911 [14], vast amounts of effort have gone into the field of superconductivity. Despite the observation of superconductivity in many other elements and compounds, as well as various insights into the problem [15, 16], it was not until the seminal papers of Bardeen, Cooper and Schrieffer (BCS), published in 1957 and resulting in a Nobel Prize that a comprehensive theory of superconductivity was developed [17, 18].

It was shown that the Fermi sea is unstable against a pairing of electrons in the presence of any non-zero attractive interaction. In the finite-temperature BCS ground state, a fraction of the electrons are condensed into a coherent superfluid, while the remaining electrons exist in a normal state. As the temperature is raised through the superconducting transition temperature T_c, the fraction of electrons in the superfluid state goes to zero, and the system as a whole undergoes a second-order phase transition.

In the weak-coupling limit of BCS theory, a perturbation to the non-interacting electronic Hamiltonian is introduced which couples electrons of opposite spin and momentum. At finite temperatures, an integral equation of the superconducting order parameter Δ_k is obtained (Eqn 1.23).

$$\Delta_k = -\sum_{k'} V_{kk'} \frac{\Delta_{k'}}{2E_{k'}} \tanh \frac{\beta E_{k'}}{2} \tag{1.23}$$

Here $E_k = (\epsilon_k^2 + \Delta_k^2)^{1/2}$ and ϵ_k are the electronic energy eigenvalues while $\beta = 1/k_B T$. Equation 1.23 can then be solved for the transition temperature which occurs as $\Delta \to 0$, under a simple approximation that the pairing interaction is constant and present on energy scales less than Θ_D. This results in an oft-cited BCS expression for T_c given by Eqn 1.24.

$$T_c = 1.13\Theta_D \; exp\,(-1/N(0)V) \tag{1.24}$$

A thorough understanding of superconductivity inherently necessitates that the problem be reframed within a many-body approach. Within conventional phonon-mediated superconductivity, we can examine supeconductivity through a Green's function approach to electron-phonon coupling. In the Green's function approach, the interaction between electrons and phonons is treated through the electron-phonon vertex g. The many-body interaction which contributes to the electron and phonon self-energy can be computed from the diagrams of Figure 1.1.

The evaluation of these diagrams leads to expressions which require the knowledge of the electron-phonon matrix elements, electronic eigenvalues, and phonon eigenfrequencies.

Of particular interest in the computation of the total electron-phonon coupling is the phonon linewidth γ_q and the imaginary part of the phonon self-energy Π_q, as seen

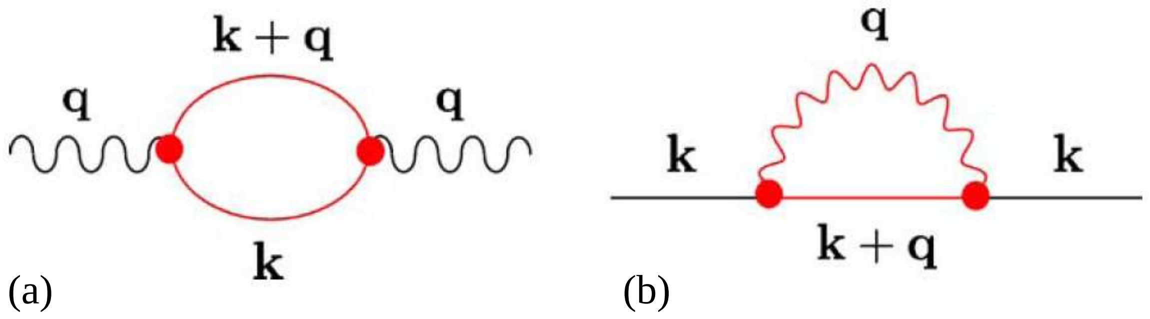

Figure 1.1: Schematic diagrams of the (a) electron self-energy and (b) phonon self-energy as calculated through the Green's function approach to the electron-phonon interaction.

in Fig 1.1(a). Additionally, the electron self-energy of quasiparticles on the Fermi surface depicted in Fig 1.1(b) can be observed through angle-resolved photoemission [19]. As has been demonstrated in Refs. [7, 8], the Eliashberg spectral function $\alpha^2 F$ is expressed as a sum over the contributions from scattering processes which connect electrons through phonons on the Fermi surface.

$$\alpha^2 F(\omega) = \frac{1}{N_q} \sum_{\mathbf{q}\nu} \delta(\omega - \omega_{q\nu}) \frac{1}{N_{\mathrm{F}} \omega_{\mathbf{q}\nu}} \sum_{mn,\mathbf{k}} w_{\mathbf{k}} |g^{\nu}_{mn}(\mathbf{k}, \mathbf{q})|^2 \delta(\epsilon_{n\mathbf{k}}) \delta(\epsilon_{m\mathbf{k}+\mathbf{q}}), \tag{1.25}$$

The total electron-phonon coupling parameter λ is then an integral over the Eliashber spectral function.

$$\lambda = 2 \int \frac{\alpha^2 F(\omega')}{\omega'} d\omega' \tag{1.26}$$

Due to the extensive efforts of McMillan [20], a semi-empirical formula was developed which relates the superconducting transition temperature T_c to the total electron-phonon coupling strength λ, a characteristic phonon frequency ω_{log} and the strength of the Coulomb repulsion μ^*.

$$T_c = \frac{\omega_{log}}{1.2}\, exp \left(- \frac{-1.04(1 + \lambda)}{\lambda + \mu^* - 0.62 \lambda \mu^*} \right) \tag{1.27}$$

Values of the Coulomb pseudopotential range between $\mu^* = 0.10 - 0.15$, while ω_{log} does not generally differ drastically from the Debye frequency ω_D. The above equation for T_c provides a very good method for comparing *ab inito* calculated parameters to the experimentally measured transition temperature.

Chapter 2

EPW: Efficient calculation of the electron-phonon interaction

2.1 Introduction

The electron-phonon interaction plays a crucial role in the electron and lattice dynamics of condensed matter systems. For example, phenomena such as the electrical resistivity [21] and conventional superconductivity [7] are a direct consequence of the interaction between electrons and lattice vibrations. The electron-phonon interaction also plays an important role in the thermoelectric effect [22]. Other fundamental physical phenomena such as the Kohn effect [23] and the Peierls [24] distortions are also direct consequences of the electron-phonon interaction. The electron-phonon interaction is also responsible for the broadening of the spectral lines in angle-resolved photoemission spectroscopy [19] and in vibrational spectroscopies [25], as well as for the temperature dependence of the band gaps in semiconductors [26].

The calculation of the electron-phonon coupling from first-principles is challenging because of the necessity of evaluating Brillouin zone integrals with high accuracy. Such calculation requires the evaluation of matrix elements between electronic states connected by phonon wavevectors [27]. Well-established software packages are available for computing electronic states and eigenvalues through density-functional theory [28, 29, 30], as well as phonon frequencies and eigenmodes through density-functional perturbation theory [3]. However large numbers of matrix elements may be necessary to achieve numerical convergence of the Brillouin zone intergrals over these matrix elements.

For example, in order to compute the electronic lifetimes associated with the electron-phonon interaction it is necessary to evaluate a Brillouin zone integral over all the possible phonon wavevectors (thousands to millions). Since lattice-dynamical calculations for each phonon wavevector are at least as expensive as self-consistent total energy minimizations, achieving numerical convergence in the Brillouin zone integrals over the phonon wavevectors by brute-force calculations may become a prohibitive computational task. `EPW` exploits the real-space localization of Wannier functions to generate large numbers of first-principles electron-phonon matrix elements through a generalized Fourier interpolation. `EPW` therefore enables affordable, accurate, and extremely efficient calculations of the electron-phonon coupling [31]. The use of maximally localized Wannier functions (MLWFs) [32, 33] to calculate Brillouin zone integrals with high accuracy has been the object of a number of other studies [34, 35, 36, 37, 38, 39, 40, 41, 42, 43, 44, 45, 46].

In this communication we outline the functionalities of `EPW` and the details of the technical release (Sec. II), we review the individual sections of the code (Sec. III), and we describe its parallel structure (Sec. VI). We then illustrate the capabilities of `EPW` through example calculations (Sec. V). We finally discuss some future directions for additional development (Sec. VI). Some technical details are given in the Appendix (Sec. VII).

2.2 Functionalities and technical release

`EPW` is a program written in `FORTRAN90` which calculates the electron-phonon coupling from first principles using maximally localized Wannier functions. `EPW` uses information provided by `Quantum-ESPRESSO` [30] and `wannier90` [47], and runs as a post-processing tool. Electrons are described using density functional theory (DFT) [28, 29] with planewaves and pseudopotentials, either separable norm-conserving [48, 49, 50, 51] or Vanderbilt ultrasoft [52]. Lattice dynamical properties are calculated within density functional perturbation theory (DFPT) [3]. The theoretical background and methodology are thoroughly described in Ref. [31]. Examples of quantities [53] which can be computed using `EPW` include:

- the total electron-phonon coupling strength λ,
- the phonon self-energy associated with the electron-phonon interaction within the Migdal approximation,
- the electron self-energy associated with the electron-phonon interaction within the Migdal approximation,
- the Eliashberg electron-phonon spectral function α^2F,
- the transport electron-phonon spectral function α^2F_{T}.

`EPW` is freely available under the GNU General Public License (GPL). The current version is developed and maintained using Subversion and is accessible to prospective developers and end-users at the website `epw.org.uk`. `EPW` employs the freely available `FFTW, BLAS, LAPACK` libraries in conjunction with several subroutines distributed within the `Quantum-ESPRESSO` package. Several subroutines in `EPW` are based upon modified `Quantum-ESPRESSO` subroutines as permitted under the GPL. The parallelization is achieved through the `MPI` library specification for message passing. The current version of `EPW`, v2.3, includes approximately 9000 independent lines of `FORTRAN90` code. In addition to the source code, several complete example calculations are provided with the `EPW` distribution.

The inputs to `EPW` are as follows:

- Phonon dynamical matrices for the wavevectors of a uniform Brillouin-zone grid centered at Γ (`prefix.dyn` files from `Quantum-ESPRESSO`). Only wavevectors within the irreducible wedge of the Brillouin zone are required.

- The derivatives of the self-consistent potential with respect to the phonon perturbations, for the same wavevectors as above (`prefix.dvscf` files from `Quantum-ESPRESSO`).
- The electron eigenfunctions and eigenvalues for the wavevectors of a uniform Brillouin-zone grid centered at Γ (`prefix.wfc` or `prefix.save/` files from `Quantum-ESPRESSO`).
- Norm-conserving pseudopotentials [49] or Vanderbilt ultrasoft pseudopotentials [52],
- A plain text input file specifying the runtime parameters.

The electronic wavefunctions are calculated on a uniform grid using `Quantum-ESPRESSO`. Dynamical matrices and the derivatives of the self-consistent potential are also computed within `Quantum-ESPRESSO` for phonons in the irreducible wedge of the Brillouin zone. When choosing initial electron and phonon grids, it is necessary that the Brillouin zone grid for phonons be comensurate with the Brillouin zone grid for electrons in order to map the wavefunctions $\psi_{m\mathbf{k}+\mathbf{q}}(\mathbf{r})$ onto $\psi_{m\mathbf{k}'+\mathbf{G}}(\mathbf{r})$, with $\mathbf{G}$ a reciprocal lattice vector. For example, if the calculation is performed using a Brillouin zone grid of size $6 \times 6 \times 6$ for the phonons, then the natural choices for the electronic Brillouin zone grid are either $6 \times 6 \times 6$ or $12 \times 12 \times 12$. This does not represent a computational bottleneck as phonon calculations are considerably more time-consuming than non-selfconsistent electronic calculations.

2.3 Computational methodology

2.3.1 Physical quantities

In this section we describe some of the physical quantities which can be calculated using `EPW`. The imaginary part of the phonon self-energy within the Migdal approximation [54, 53] is calculated as:

$$\Pi''_{\mathbf{q}\nu} = \mathrm{Im} \sum_{mn,\mathbf{k}} w_{\mathbf{k}} |g^{\nu}_{mn}(\mathbf{k},\mathbf{q})|^2 \frac{f(\epsilon_{n\mathbf{k}}) - f(\epsilon_{m\mathbf{k}+\mathbf{q}})}{\epsilon_{n\mathbf{k}} - \epsilon_{m\mathbf{k}+\mathbf{q}} - \omega_{\mathbf{q}\nu} + i\eta}. \tag{2.1}$$

In Eq. (2.1) the electron-phonon matrix elements are given by

$$g^{\nu}_{mn}(\mathbf{k},\mathbf{q}) = \langle \psi_{m\mathbf{k}+\mathbf{q}} | \partial_{\mathbf{q}\nu} V | \psi_{n\mathbf{k}} \rangle, \tag{2.2}$$

with $\psi_{n\mathbf{k}}$ the electronic wavefunction for band m, wavevector $\mathbf{k}$, and eigenvalue $\epsilon_{n\mathbf{k}}$, $\partial_{\mathbf{q}\nu} V$ the derivative of the self-consistent potential associated with a phonon of wavevector $\mathbf{q}$, branch index ν, and frequency $\omega_{\mathbf{q}\nu}$. The factors $f(\epsilon_{n\mathbf{k}}), f(\epsilon_{m\mathbf{k}+\mathbf{q}})$ in Eq. (2.1) are the Fermi occupations, and $w_{\mathbf{k}}$ are the weights of the $\mathbf{k}$-points normalized to 2 in order to account for the spin degeneracy in spin-unpolarized calculations. A very common approximation to Eq. (2.1) consists of neglecting the phonon frequencies $\omega_{\mathbf{q}\nu}$ and taking the limit of small broadening η. The final expression is positive definite and is often referred to as the "double-delta function" approximation [53]. This approximation is no longer necessary when using `EPW`. We note that the imaginary part of the phonon self-energy in Eq. (2.1) also corresponds to the phonon half-width at half-maximum $\gamma_{\mathbf{q}\nu}$.

The electron-phonon coupling strength associated with a specific phonon mode and wavevector $\lambda_{\mathbf{q}\nu}$ is given by

$$\lambda_{\mathbf{q}\nu} = \frac{1}{N_{\mathrm{F}}\omega_{\mathbf{q}\nu}} \sum_{mn,\mathbf{k}} w_{\mathbf{k}} |g_{mn}^{\nu}(\mathbf{k},\mathbf{q})|^2 \delta(\epsilon_{n\mathbf{k}})\delta(\epsilon_{m\mathbf{k}+\mathbf{q}}), \tag{2.3}$$

with δ being the Dirac delta function. In the double-delta function approximation the coupling strength $\lambda_{\mathbf{q}\nu}$ can be related to the imaginary part of the phonon self-energy $\Pi''_{\mathbf{q}\nu}$ as follows:

$$\lambda_{\mathbf{q}\nu} = \frac{1}{\pi N_{\mathrm{F}}} \frac{\Pi''_{\mathbf{q}\nu}}{\omega^2_{\mathbf{q}\nu}} \tag{2.4}$$

The total electron-phonon coupling λ is calculated as the Brillouin-zone average of the mode-resolved coupling strengths $\lambda_{\mathbf{q}\nu}$:

$$\lambda = \sum_{\mathbf{q}\nu} w_{\mathbf{q}} \lambda_{\mathbf{q}\nu}. \tag{2.5}$$

In Eq. (2.5) the $w_{\mathbf{q}}$ are the Brillouin zone weights associated with the phonon wavevectors $\mathbf{q}$, normalized to 1 in the Brillouin zone. The Eliashberg spectral function $\alpha^2 F$ can be calculated in terms of the mode-resolved coupling strengths $\lambda_{\mathbf{q}\nu}$ and the phonon frequencies using:

$$\alpha^2 F(\omega) = \frac{1}{2} \sum_{\mathbf{q}\nu} w_{\mathbf{q}} \omega_{\mathbf{q}\nu} \lambda_{\mathbf{q}\nu}\, \delta(\omega - \omega_{\mathbf{q}\nu}). \tag{2.6}$$

The transport spectral function $\alpha^2 F_{\mathrm{T}}$ is obtained from the Eliashberg spectral function $\alpha^2 F$ by replacing $\lambda_{\mathbf{q}\nu}$ with $\lambda_{\mathrm{T},\mathbf{q}\nu}$:

$$\alpha^2 F_{\mathrm{T}}(\omega) = \frac{1}{2} \sum_{\mathbf{q}\nu} w_{\mathbf{q}} \omega_{\mathbf{q}\nu} \lambda_{\mathrm{T},\mathbf{q}\nu} \delta(\omega - \omega_{\mathbf{q}\nu}), \tag{2.7}$$

$$\lambda_{\mathrm{T},\mathbf{q}\nu} = \frac{1}{N_{\mathrm{F}}\omega_{\mathbf{q}\nu}} \sum_{mn,\mathbf{k}} w_{\mathbf{k}} |g_{mn}^{\nu}(\mathbf{k},\mathbf{q})|^2 \delta(\epsilon_{n\mathbf{k}})\delta(\epsilon_{m\mathbf{k}+\mathbf{q}}) \left(1 - \frac{\mathbf{v}_{n\mathbf{k}} \cdot \mathbf{v}_{m\mathbf{k}+\mathbf{q}}}{|\mathbf{v}_{n\mathbf{k}}|^2}\right), \tag{2.8}$$

with $\mathbf{v}_{n\mathbf{k}} = \nabla_{\mathbf{k}} \epsilon_{n\mathbf{k}}$ the electron velocity.

The real and imaginary parts of the electron self-energy $\Sigma_{n\mathbf{k}} = \Sigma'_{n\mathbf{k}} + i\Sigma''_{n\mathbf{k}}$ can be calculated as

$$\Sigma_{n\mathbf{k}} = 2\sum_{\mathbf{q}\nu} w_{\mathbf{q}} |g_{mn}^{\nu}(\mathbf{k},\mathbf{q})|^2 \left[\frac{n(\omega_{\mathbf{q}\nu}) + f(\epsilon_{m\mathbf{k}+\mathbf{q}})}{\epsilon_{n\mathbf{k}} - \epsilon_{m\mathbf{k}+\mathbf{q}} + \omega_{\mathbf{q}\nu} - i\eta} + \frac{n(\omega_{\mathbf{q}\nu}) + 1 - f(\epsilon_{m\mathbf{k}+\mathbf{q}})}{\epsilon_{n\mathbf{k}} - \epsilon_{m\mathbf{k}+\mathbf{q}} - \omega_{\mathbf{q}\nu} + i\eta} \right], \tag{2.9}$$

with $n(\omega_{\mathbf{q}\nu})$ the Bose occupation factors.

Another useful quantity which can be obtained through `EPW` is the phonon-assisted indirect absorption of photon in semiconductors. In addition to the electron-phonon matrix elements, this quantity requires knowledge of the momentum matrix elements. These matrix elements are obtained through a Wannier rotation in the same way that the electronic Hamiltonian eigenvalues are calculated. The quantity which results from a call to the `indabs` subroutine is $\alpha_{el-ph}(\omega)$, the indirect absorption coefficient given by Equation 2.10 [55].

$$\alpha_{el-ph}(\omega) = 2\frac{C}{\omega}\sum_{\nu ijkq} |\lambda \cdot (S_1 + S_2)|^2 \times P\delta(\epsilon_{j,k+q} - \epsilon_{i,k} - \hbar\omega \pm \hbar\omega_{q\nu}) \tag{2.10}$$

Here $\hbar\omega$ and λ are the photon energies and polarizations $C = 4\pi^2 e^2/n_r cm^2$ and n_r is the refraction index. The generalized matrix elements S_1 and S_2 and the statistics under the P factor are

$$S_1(k,q) = \sum_m \frac{p_{im}(k) g^{\nu}_{mj}(k,q)}{\epsilon_{mk} - epsilon_{ik} - \hbar\omega} \tag{2.11}$$

$$S_2(k,q) = \sum_m \frac{g^{\nu}_{im}(k,q) p_{mj}(k)}{\epsilon_{m,k+q} - epsilon_{ik} \pm \hbar\omega_{q\nu}} \tag{2.12}$$

$$P = \left(n_{q\nu} + \frac{1}{2} \pm \frac{1}{2}\right)(f_{i,k} - f_{j,k+q}) \tag{2.13}$$

where $p_{ij}(k)$ are the dipole matrix elements.

2.3.2 Calculation of the matrix elements on the coarse Brillouin zone grid

The key task of `EPW` is to calculate from first-principles electron-phonon matrix elements for a large number of electron and phonon wavevectors with a modest computational effort. The initial step of this process is to determine the electron-phonon matrix elements on coarse grids of electron and phonon wavevectors using standard DFT and DFPT methods [56]. The result of this step is a set of matrix elements given by Eq. (2.2). The wavefunctions and the phonon perturbation potentials are read into `EPW`, then the matrix elements on the coarse grid are calculated within `EPW`.

The phonon dynamical matrices and the linear variations of the self-consistent potential are read from file only for wavevectors in the irreducible wedge of the Brillouin zone. The dynamical matrices and the potentials variations for all the remaining points of the uniform grid are generated using crystal symmetry operations. This strategy is advantageous since the computation of the phonon dynamical matrices and potential variations is generally the most time-consuming part of an electron-phonon calculation. For example, a system with cubic symmetry requiring a coarse mesh of $8 \times 8 \times 8$ phonon wavevectors needs only have phonons calculated at 29 irreducible points; hence the reduction in computational time is a factor of 512/29.

The electron-phonon matrix elements and the dynamical matrices thus calculated at each point of the coarse Brillouin-zone grid can be written to disk through an input file option (`prefix.epb` files). Subsequent executions of `EPW` can forgo the recalculation of the matrix elements and dynamical matrices by reading these data from disk.

2.3.3 Interface with `wannier90`

`wannier90` generates maximally localized Wannier functions by minimizing the spread of the Berry-phase position operator through a unitary transform [32]. Details on how to run `wannier90` can be found in the `wannier90` documentation [47].

In standalone mode `wannier90` reads three files generated from a first-principles calculation (`prefix.mmn, prefix.amn, prefix.eig`), a file which defines the starting guess for determining MLWFs and the crystal structure (`prefix.nnkp`), and a runtime input file (`prefix.win`). The execution of `wannier90` therefore requires the user to run multiple programs and handle the files to be passed between `wannier90` and `Quantum-ESPRESSO`. In order to simplify the calculation of the electron-phonon coupling `EPW` calls `wannier90` as a library. `EPW` therefore requires only the wavefunction files from `Quantum-ESPRESSO` and a runtime input file in order to determine MLWFs using `wannier90`. The quantites required for running `wannier90` are either calculated within `EPW` (for instance the overlap matrices A_{mn} and M_{mn} [47]), or else read in from file (for instance the Kohn-Sham eigenvalues). These data are then passed from `EPW` to `wannier90` through the `wannier_run` library routine. This feature of `EPW` ensures that the execution of `wannier90` is embedded within `EPW`. Hence the end user is only required to run one single executable which communicates directly with `wannier90`. `EPW` also includes an option to pass additional input parameters to `wannier90`. This allows the user to access all the available features of `wannier90`, such as for instance plotting bandstructures or MLWFs. When called from `EPW`, `wannier90` produces the gauge matrix $U^{\mathbf{k}}_{mn}$ [47], which yields the transformation between Bloch eigenstates and MWLFs, according to:

$$w_{n\mathbf{R}_e}(\mathbf{r}) = \frac{\Omega}{(2\pi)^3}\int_{\mathrm{BZ}} d\mathbf{k}\ \mathrm{e}^{-i\mathbf{k}\cdot\mathbf{R}_e}\sum_m U^{\mathbf{k}}_{mn}\,\psi_{m\mathbf{k}}(\mathbf{r}), \tag{2.14}$$

where $w_{n\mathbf{R}_e}$ is a MLWF associated with the direct lattice vector $\mathbf{R}_e$, Ω is the unit cell volume, and the integral is discretized over the Brillouin zone. The array $U^{\mathbf{k}}_{mn}$ has the dimensions of the number of Bloch bands times the number of MLWFs times the number of electronic wavevectors in the coarse Brillouin zone grid. This matrix is written to disk and can directly be read on subsequent program executions. The array $U^{\mathbf{k}}_{mn}$ is used in `EPW` in order to transform Bloch functions into MLWFs.

2.3.4 Transformation from the Bloch representation on the coarse Brillouin zone grid to the MLWF representation

After calculating the electron-phonon matrix elements in the Bloch representation for each wavevector on the coarse electron and phonon Brillouin zone grids, `EPW` transforms the electronic Hamiltonian, the phonon dynamical matrix, and the electron-phonon matrix elements into the Wannier representation. Derivations and detailed explanations of the following transformations can be found in Ref. [31]. For clarity the electron band and the phonon mode indices will be omitted in the following equations. The electronic Hamiltonian in the MLWF representation $H^{\mathrm{el}}_{\mathbf{R}_\mathrm{e},\mathbf{R}'_\mathrm{e}}$ is obtained as:

$$H^{\mathrm{el}}_{\mathbf{R}_\mathrm{e},\mathbf{R}'_\mathrm{e}} = \sum_{\mathbf{k}} w_{\mathbf{k}}\mathrm{e}^{-i\mathbf{k}\cdot(\mathbf{R}'_\mathrm{e}-\mathbf{R}_\mathrm{e})}U^{\dagger}_{\mathbf{k}}H^{\mathrm{el}}_{\mathbf{k}}U_{\mathbf{k}}. \tag{2.15}$$

In this case the weights $w_{\mathbf{k}}$ are normalized to 1. The Hamiltonian matrix elements in the Wannier representation $H^{\mathrm{el}}_{\mathbf{R}_{\mathrm{e}},\mathbf{R}'_{\mathrm{e}}}$ decay rapidly with the distance $|\mathbf{R}_{\mathrm{e}} - \mathbf{R}'_{\mathrm{e}}|$, as they scale with the overlap of MLWFs centered in the unit cells $\mathbf{R} = \mathbf{R}_{\mathrm{e}}$ and $\mathbf{R} = \mathbf{R}'_{\mathrm{e}}$, respectively. The dipole matrix elements in the MLWF representation $P^{\mathrm{el}}_{\mathbf{R}_{\mathrm{e}},\mathbf{R}'_{\mathrm{e}}}$ are obtained in the same manner as the Hamiltonian. This is done as only the electronic states which compose the Bloch-space matrix element are rotated to obtain the real-space representation.

$$P^{\mathrm{el}}_{\mathbf{R}_{\mathrm{e}},\mathbf{R}'_{\mathrm{e}}} = \sum_{\mathbf{k}} w_{\mathbf{k}} \mathrm{e}^{-i\mathbf{k}\cdot(\mathbf{R}'_{\mathrm{e}}-\mathbf{R}_{\mathrm{e}})} U^{\dagger}_{\mathbf{k}} P^{\mathrm{el}}_{\mathbf{k}} U_{\mathbf{k}}. \tag{2.16}$$

The dynamical matrix can be transformed to a localized real-space representation using

$$D^{\mathrm{ph}}_{\mathbf{R}_{\mathrm{p}},\mathbf{R}'_{\mathrm{p}}} = \sum_{\mathbf{q}} w_{\mathbf{q}} \mathrm{e}^{-i\mathbf{q}\cdot(\mathbf{R}'_{\mathrm{p}}-\mathbf{R}_{\mathrm{p}})} \mathbf{e}_{\mathbf{q}} D^{\mathrm{ph}}_{\mathbf{q}} \mathbf{e}^{\dagger}_{\mathbf{q}}, \tag{2.17}$$

where $\mathbf{e}_{\mathbf{q}}$ are the orthonormal eigenvectors of the dynamical matrix. The matrix $D^{ph}_{\mathbf{R}_{\mathrm{p}},\mathbf{R}'_{\mathrm{p}}}$ is the mass-scaled matrix of force constants. The electron-phonon matrix elements in the MLWF representation are obtained using:

$$g(\mathbf{R}_{\mathrm{e}},\mathbf{R}_{\mathrm{p}}) = \frac{1}{N_{\mathrm{p}}} \sum_{\mathbf{k},\mathbf{q}} w_{\mathbf{k}} w_{\mathbf{q}} \mathrm{e}^{-i(\mathbf{k}\cdot\mathbf{R}_{\mathrm{e}}+\mathbf{q}\cdot\mathbf{R}_{\mathrm{p}})} U^{\dagger}_{\mathbf{k}+\mathbf{q}} g(\mathbf{k},\mathbf{q}) U_{\mathbf{k}} \mathbf{u}^{-1}_{\mathbf{q}} \tag{2.18}$$

where the $\mathbf{u}^{\nu}_{\mathbf{q}\kappa}$ are the phonon eigenvectors scaled by the atomic masses [31]. In order to check the spatial decay of $H^{\mathrm{el}}_{\mathbf{R}_{\mathrm{e}},0}$, $D^{\mathrm{ph}}_{\mathbf{R}_{\mathrm{p}},0}$, and $g(\mathbf{R}_{\mathrm{e}},\mathbf{R}_{\mathrm{p}})$ the magnitude of these quantites as a function of $\mathbf{R}_{\mathrm{e}}$ and $\mathbf{R}_{\mathrm{p}}$ is written to formatted files in the working directory. A run-time option allows for all data in the Wannier representation to be written into one single file. For subsequent calculations these data can be read in and program execution can restart without the need to go through the prior computational steps.

2.3.5 Tranformation from the MLWF representation to the Bloch representation on the fine Brillouin zone grid

The accuracy of `EPW` calculations depends on the spatial localization of the MLWFs and the phonon perturbations. Typically MLWFs are localized within a few Å[57, 58]. The localization of the phonon perturbation is dependent upon the dielectric screening properties of the system, and must be verified in each case before proceeding with the interpolation [31].

In order to calculate the electronic eigenstates, the phonon frequencies, and the electron-phonon matrix elements on a fine Brillouin zone grid, the Hamiltonian, the dynamical matrix, and the electron-phonon matrix elements are truncated outside of a real-space supercell containing $N_{\mathbf{k}}$ and $N_{\mathbf{q}}$ unit cells in the case of electrons and phonons, respectively. Here $N_{\mathbf{k}}$ and $N_{\mathbf{q}}$ are the number of grid points in the coarse Brillouin zone meshes. Following this truncation it is possible to perform an interpolation back into the Bloch representation onto arbitrary electron and phonon wavevectors. The Hamiltonian, the dynamical matrix, and the electron-phonon matrix elements are Fourier-transformed back to the Bloch representation by inverting Eqs. (2.15), (2.17), and (2.18) [31].

The procedure described here enables the calculation of electron-phonon matrix elements on extremely fine Brillouin zone grids. The fine grids of electron and phonon wavevectors are specified by the user in input. The procedure adopted here is similar to the Fourier interpolation of time series commonly adopted in signal processing [59]. The same strategy as the one employed in `EPW` has been adopted in order to study Fermi surfaces [34] and the anomalous Hall effect [36].

At this stage the Hamiltonian, the dynamical matrix, and the electron-phonon matrix elements on fine grids of electron and phonon wavevectors are used to compute the physical quantities described in Sec. 2.3.1.

2.3.6 Specifying a unique gauge for the electronic wavefunctions

Since nondegenerate electronic wavefunctions are uniquely defined up to a phase, and a set of degenerate wavefunctions can be mixed via a unitary matrix, electron-phonon matrix elements are machine dependent. In some cases it may be convenient to use electron-phonon matrix elements outside of `EPW`, for instance in the study of phonon sidebands in excitonic spectra [60], or in the phonon-assisted Auger recombination [61]. In order to meaningfully use the electron-phonon matrix elements generated by `EPW` outside of the code it is necessary to define uniquely the phase of each wavefunction as well as the way in which degenerate wavefunctions are mixed.

In order to set the gauge of each wavefunction in `EPW` we proceed as follows. First, we determine the subset of degenerate wavefunctions at each wavevector on the coarse mesh. Then we artificially lift the degeneracies by diagonalizing the subset of degenerate states with respect to a small external perturbation. In principle the perturbation could take on any form, however for convenience `EPW` employs a nonlinear combination of the data found in the `prefix.dvscf` files. Finally, the Fourier components of each wavefunction are scaled by a complex factor $\exp(i\theta)$ in such a way that the largest component of each wavefunction is real-valued. In this way, the machine dependence of the matrix elements is eliminated. This procedure is explained in detail in Ref. [31].

2.3.7 Summary of the tasks executed by `EPW`

The computational steps described in the previous sections can be summarized schematically as follows:

1. Electron eigenstates and eigenvalues are read from disk,

2. `wannier90` input data including the overlap matrices A_{mn} and M_{mn} are computed,

3. `wannier90` is called as a library, and the resulting MLWF localization matrix is stored on disk.

4. The electron-phonon matrix elements are computed on a coarse grids of electron and phonon wavevectors in the Bloch representation,

5. The Hamiltonian, dynamical matrix, and electron-phonon matrix elements are transformed from the Bloch representation to the MLWF representation,

6. The Hamiltonian, dynamical matrix, and electron-phonon matrix elements are Fourier-transformed back to the Bloch representation on arbitrarily dense grids of electron and phonon wavevectors,

7. The electronic eigenvalues, phonon frequencies, and electron-phonon matrix elements are processed in order to calculate physical quantites such as, for instance, the electron self-energy or the electron-phonon coupling strength.

2.4 Parallelization

`EPW` is designed and optimized to be executed on multiple processors. Within the `Quantum-ESPRESSO` package, parallel tasks are split into processor "pools", where each pool is allocated a set of electronic wavevectors **k**. If there is more than one processor within each pool, the reciprocal space **G**-vectors for describing the wavefunctions are split amongst the processors of that pool. `EPW` can be executed in parallel by splitting the calculation over electron or phonon wavevectors. `EPW` is not parallelized over the reciprocal-space **G**-vectors. The parallelization strategy in `EPW` is tailored to each step of the computation. As execution of `EPW` begins, the coarse **k**-point mesh is generated and distributed amongst the available pools, as in `Quantum-ESPRESSO`.

Most of the inputs to the `wannier90` such as the lattice and reciprocal vectors are passed through `Quantum-ESPRESSO` and `EPW`. Important exceptions are the overlap matrices A_{mn} and M_{mn}. Within `EPW` the computation of the overlap matrix elements is distributed across the coarse grid **k**-point pools. As the elements of the matrices A_{mn} and M_{mn} are computed independently, the execution time of this step scales inversely with the the number of pools.

`wannier90` is executed serially on each processor through a library call. The time required to determine MLWFs is negligible as compared to the computation of the electron-phonon matrix elements on the coarse Brillouin zone grids.

The electron-phonon matrix elements on the coarse Brillouin zone grid are computed sequentially for each phonon wavevector, while the electron wavevectors are distributed across pools.

The computation of the electron-phonon matrix elements on the fine Brillouin zone grids is parallelized over electronic or phonon wavevectors depending on the calculation type. For example, when calculating the phonon self-energy an integration is required over electronic wavevectors. In this case the most convenient strategy is to parallelize over the electronic wavevectors. The converse is true for the calculation of the electron self-energy. In those cases where the final quantity requires integrations over both electron and phonon wavevectors, such as the total electron-phonon coupling strength, the efficiency of `EPW` is independent of the choice of the parallelization scheme.

Figure 2.1 shows the efficiency of our parallelization strategy for various sections of `EPW` for the test case of hole-doped SiC. This example is included for reference in the `EPW` distribution.

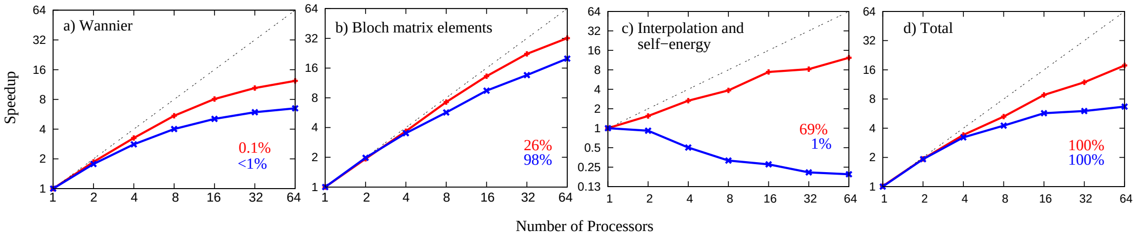

Figure 2.1: Parallelization of `EPW`: speedup vs number of processors observed in parallelizing a) the generation of MLWFs, b) the calculation of the electron-phonon matrix elements on the coarse Brillouin zone grids, c) the interpolation of the electron-phonon matrix elements to the fine Brillouin zone grids as well as the computation of the phonon self-energy. Panel d) displays the speedup observed to perform the entire computation including the initialization step and the intermediate I/O. The speedup is defined as the ratio between the time it takes to run a calculation on a single processor and the time it takes to run the same calculation on a given number of processors. The diagonal dotted lines correspond to the ideal speedup, which is equal to the number of processors employed. The calculations have been performed for hole-doped SiC in the rigid-band approximation. The unit cell contains 2 atoms. The blue line corresponds to a calculation with coarse Brillouin zone grids containing $6 \times 6 \times 6$ **k**- and **q**-points, a kinetic energy cutoff of 30 Ry, and fine Brillouin zone grids containing 1000 points each. The red line corresponds to a calculation with coarse Brillouin zone grids containing $8 \times 8 \times 8$ **k**- and **q**-points, a kinetic energy cutoff of 60 Ry, and fine **k**- and **q**-points grids containing 10^6 and 104 points (the irreducible points of a uniform and unshifted $14 \times 14 \times 14$ grid), respectively. The parallelization becomes more efficient as the number of electron and phonon wavevectors in the fine Brillouin zone grids is increased.

2.4.1 Calculations "on the fly"

The interpolation part of `EPW` can be executed in two different modes. In the first mode `EPW` calculates all the electron-phonon matrix elements for every **k**- and **q**-point of the fine Brillouin zone grids, and stores this information to disk. The subroutines for calculating the electron or phonon self-energy are then called and the matrix elements along with the electronic eigenvalues and the phonon frequencies are read from disk in order to evaluate Eqs. (2.1), (2.9).

In the second mode of operation, the electron or the phonon self-energy are calculated "on the fly" as the matrix elements are generated, and all the quantities are overwritten. In this case the matrix elements are not stored on disk.

This feature allows us to address systems for which the storage required for the electron-phonon matrix elements would be exceedingly large. For example, if the fine electron and phonon Brillouin zone grids consisted each of 10^5 wavevectors, and we had 8 MLWFs and 6 phonon modes, then the entire set of double precision matrix elements would require more than 1 TB of storage. On the other hand the calculation on the fly would reduce the storage requirement down to a manageable size of 1 TB.

2.5 Examples

In the following we illustrate the capabilities of `EPW` by describing three prototypical systems: (i) Lead, a simple metal which is also a strong-coupling superconductor. (ii) Graphene, a two-dimensional zero-gap semiconductor with linear quasiparticle dispersions close to the Fermi level. (iii) Silicon carbide, a wide-gap semiconductor which becomes a low-temperature superconductor upon boron doping.

2.5.1 Lead

Solid Pb is the prototypical strong-coupling superconductor. While the superconducting transition temperature of Pb is less than 10 K, the electron-phonon coupling strength has been measured and calculated to be very large, in the range of $\lambda = 1.3 \pm 0.1$ [62, 63, 64, 65, 66].

In this section we present an example calculation of the electron-phonon coupling in bulk Pb and we compare our results to experimental data. The calculations were performed within the local-density approximation to density functional theory using `Quantum-ESPRESSO`, `wannier90`, and `EPW`. A norm-conserving, scalar-relativistic pseudopotential including four valence electrons was used to take into account the core-valence interaction. The electronic states were computed within a plane-wave basis with a kinetic energy cutoff of 80 Ry. The charge density was computed self-consisently on a $16 \times 16 \times 16$ Γ-centered Brillouin zone grid. The electronic wavefunctions used within `EPW` were calculated on an $8 \times 8 \times 8$ uniform Brillouin zone grid. The phonon dynamical matrices and the linear variations of the self-consistent potential were calculated within DFPT using the `Quantum-ESPRESSO` package, using the same convergence parameters as above. We considered a uniform $8 \times 8 \times 8$ Brillouin zone grid for the phonon calculations, corresponding to 29 irreducible phonon wavevectors.

Four Wannier states were used to reconstruct the electronic structure near the Fermi level. These states were found to be sp^3-like functions localized symmetrically along each of the Pb-Pb bonds, with a spatial spread of 2.17 Å. The spatial decay of the electron Hamiltonian, the phonon dynamical matrix, and the electron-phonon matrix elements in the MLWF representation are shown in Fig. 2.2.

In order to calculate the phonon linewidths and the total electron-phonon coupling, the electron Hamiltonian, the phonon dynamical matrix, and the electron-phonon matrix elements were transformed from the MLWF representation to the Bloch representation by the generalized Fourier interpolation described in Sec. 2.3.5. By using 10^6 $\mathbf{k}$-points, 8000 $\mathbf{q}$-points, and a smearing parameter of 30 meV, we obtained a total electron-phonon coupling strength $\lambda = 1.41$. The Eliashberg spectral function $\alpha^2F(\omega)$ is shown in Fig. 2.3, together with the experimental curve obtained by inverting tunneling data [62]. Our method clearly yields a very good agreement with experiment.

For comparison with experiment we also calculated the superconducting transition temperature $T_{\rm c}$ starting from the total electron-phonon coupling. We adopted the modified McMillan equation [67] and a Coulomb repulsion parameter μ^* between 0.10 and 0.15, obtaining T_c equal to 4K to 6K respectively. This result compares favorably to the experimental value 7.2 K.

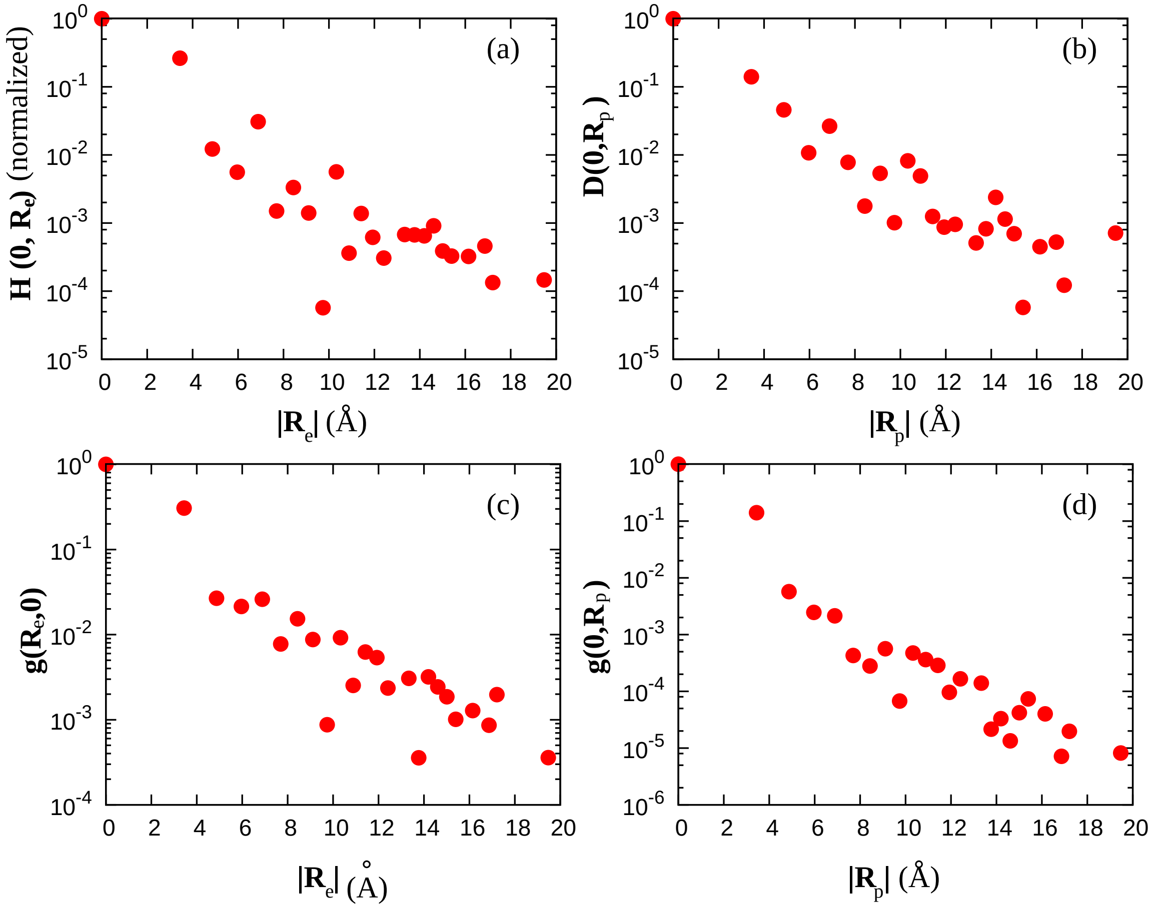

Figure 2.2: Spatial decay of the largest components of the Hamiltonian $H^{\mathrm{el}}_{\mathbf{R}_{\mathrm{e}},0}$ (a), the dynamical matrix $D^{\mathrm{ph}}_{\mathbf{R}_{\mathrm{p}},0}$ (b), and the electron-phonon matrix elements $g(0, \mathbf{R}_{\mathrm{p}})$ (c) and $g(\mathbf{R}_{\mathrm{e}}, 0)$ (d) for fcc Pb. The data are plotted as a function of distance and are taken along several directions.

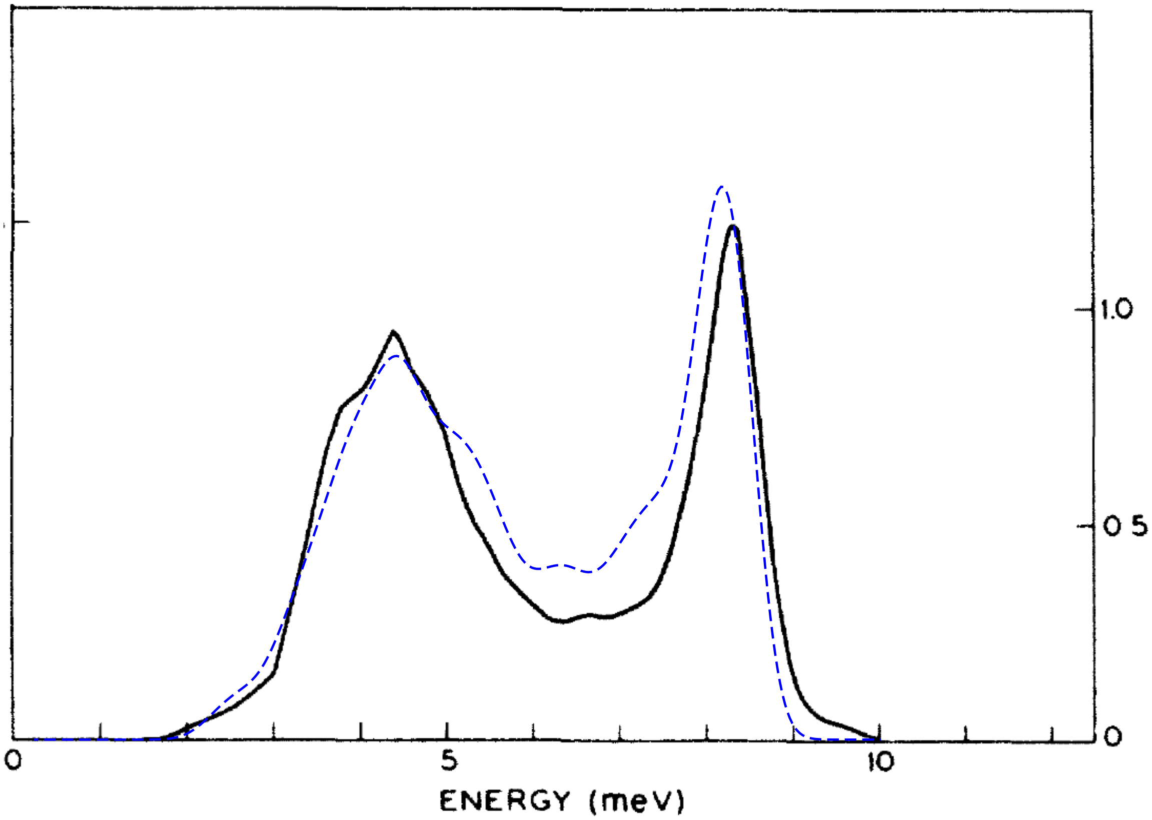

Figure 2.3: Eliashberg spectral function of fcc Pb. The solid line is from Ref. [62], the dashed line has been obtained using `EPW`.

2.5.2 Graphene

Graphene is a two-dimensional sheet of carbon atoms which has attracted enourmous attention from the scientific community due to its peculiar electronic properties [68], and in particular the Dirac-like nature of electrons near the Fermi level [69, 70]. Considerable attention has been paid to the measurement of many-body renormalization effects, such as the effect of the electron-phonon interaction on the electronic bandstructure, using for instance angle-resolved photoemission experiments [71].

We here present the results of an electron-phonon calculation on a sheet of freestanding graphene [39]. The local density approximation to density functional theory was employed in conjunction with a norm-conserving carbon pseudopotential. A plane wave basis with a kinetic energy cutoff of 60 Ry was used. The graphene sheets were separated by a vacuum of 8 Å in a supercell geometry in order to eliminate spurious interactions between periodic replicas. The relaxed C-C bond length was found to be 1.405 Å.

Three in-plane bonding Wannier functions, two p_z-like Wannier functions (one per each carbon atom), and two s-like Wannier functions directly above and below the center of the hexagon (away from the graphene plane by 1.57 Å) in the two-atom unit cell were used to describe the electronic structure. The spatial spread of these MLWFs are 0.565 Å, 0.782 Å, and 1.726 Å, respectively. The spatial decay of the electron Hamiltonian, the phonon dynamical matrix, and the electron-phonon matrix elements in the MLWF representation for a $6 \times 6 \times 1$ grid are shown in Fig. 2.4.

The electron self-energy was computed and the integral of of Eq. (2.9) was performed with 10^6 phonon $\mathbf{q}$-vectors, obtained through the interpolation method of this communication. The mass renormalization parameter, $\lambda_{n\mathbf{k}}$ has been obtained as an energy derivative of the electron self-energy as in $\lambda_{n\mathbf{k}} = \frac{\partial}{\partial \epsilon}\mathrm{Re}\ \Sigma_{n\mathbf{k}}(\epsilon_{n\mathbf{k}})|_{\epsilon=\epsilon_F}$. The results of the calculations of the real and imaginary parts of the electron self-energy as well as the electron-phonon coupling parameter as a function of Fermi energy are given in Fig. 2.5.

2.5.3 Silicon carbide

The possibility of achieving superconducting behavior in semiconductors has recently attracted considerable interest, and several experimental [72, 73] and theoretical [74, 43, 75, 38, 76, 77, 78, 79] studies have been performed on this class of materials. Boron-doped SiC is a promising candidate because of its potential uses in power electronics owing to its large breakdown voltage.

For this test case we performed electron-phonon calculations on a rigid-band model of 4% hole-doped cubic SiC. For our calculations we employed the local density approximation to density functional theory, norm-conserving pseudopotentials, and a plane wave basis with a kinetic energy cutoff of 60 Ry. The relaxed lattice parameter was found to be 4.34 Å, in good agreement with the experimental value of 4.36 Å. `EPW` was executed using coarse meshes of $8\times 8 \times 8$ uniform grids of electron and phonon wavevectors. Four Wannier functions per formula unit were considered to describe the valence electronic struture. MLWFs were found to be sp_3-like functions with an average spread of 1.15 Å. The spatial decay of the electron Hamiltonian, the phonon dynamical matrix, and the electron-phonon matrix elements in the MLWF representation are shown in Fig. 2.6. We calculated the total

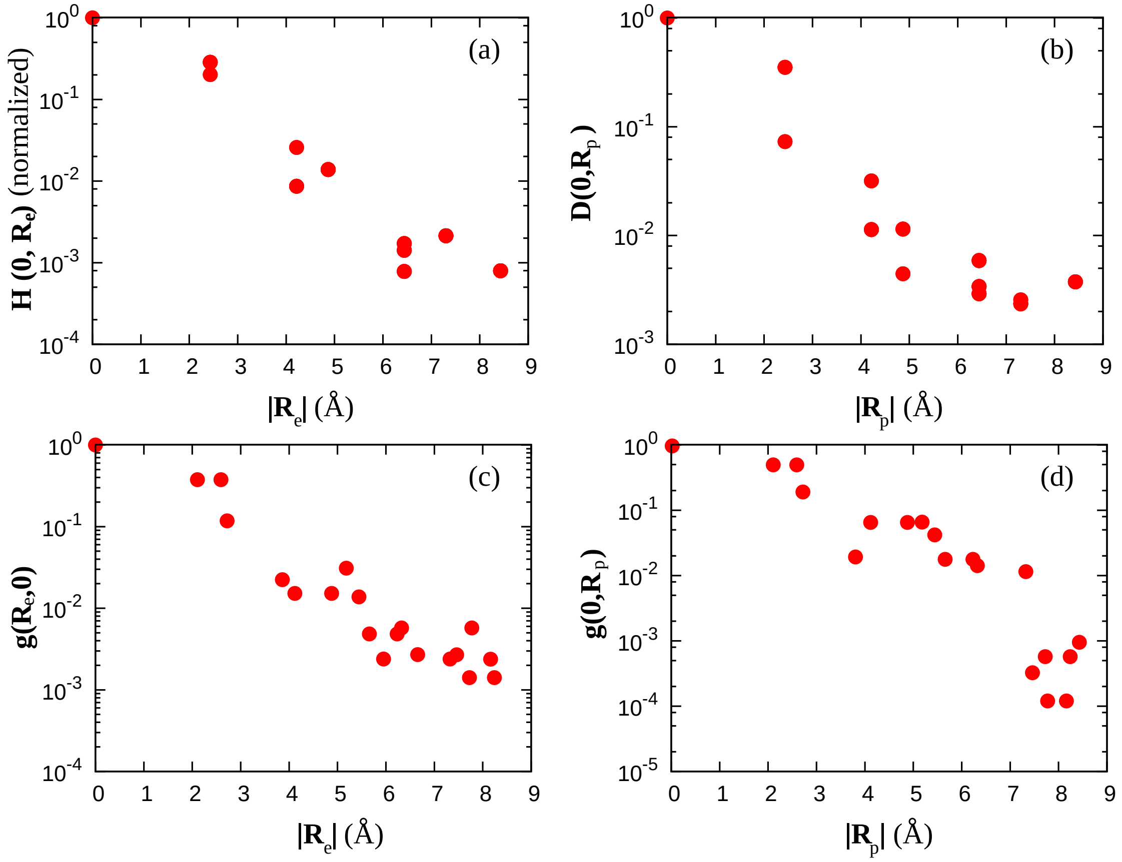

Figure 2.4: Spatial decay of the largest components of the Hamiltonian $H^{\text{el}}_{\mathbf{R}_\text{e},0}$ (a), the dynamical matrix $D^{\text{ph}}_{\mathbf{R}_\text{p},0}$ (b), and the electron-phonon matrix elements $g(0,\mathbf{R}_\text{p})$ (c) and $g(\mathbf{R}_\text{e},0)$ (d) for graphene. The data are plotted as a function of distance and are taken along several directions.

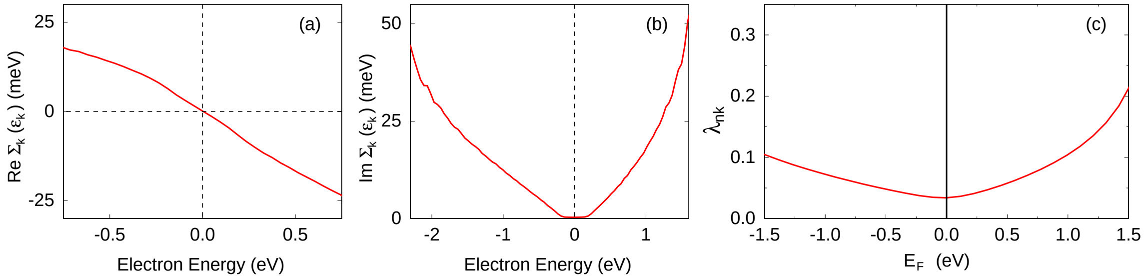

Figure 2.5: The real (a) and imaginary (b) parts of the electron self-energy $\Sigma_\mathbf{k}$ near the Dirac point as well as the electron-phonon coupling $\lambda_{n\mathbf{k}}$ as a function of doping (c) for graphene. In panels (a) and (b), the Fermi energy has been set to zero.

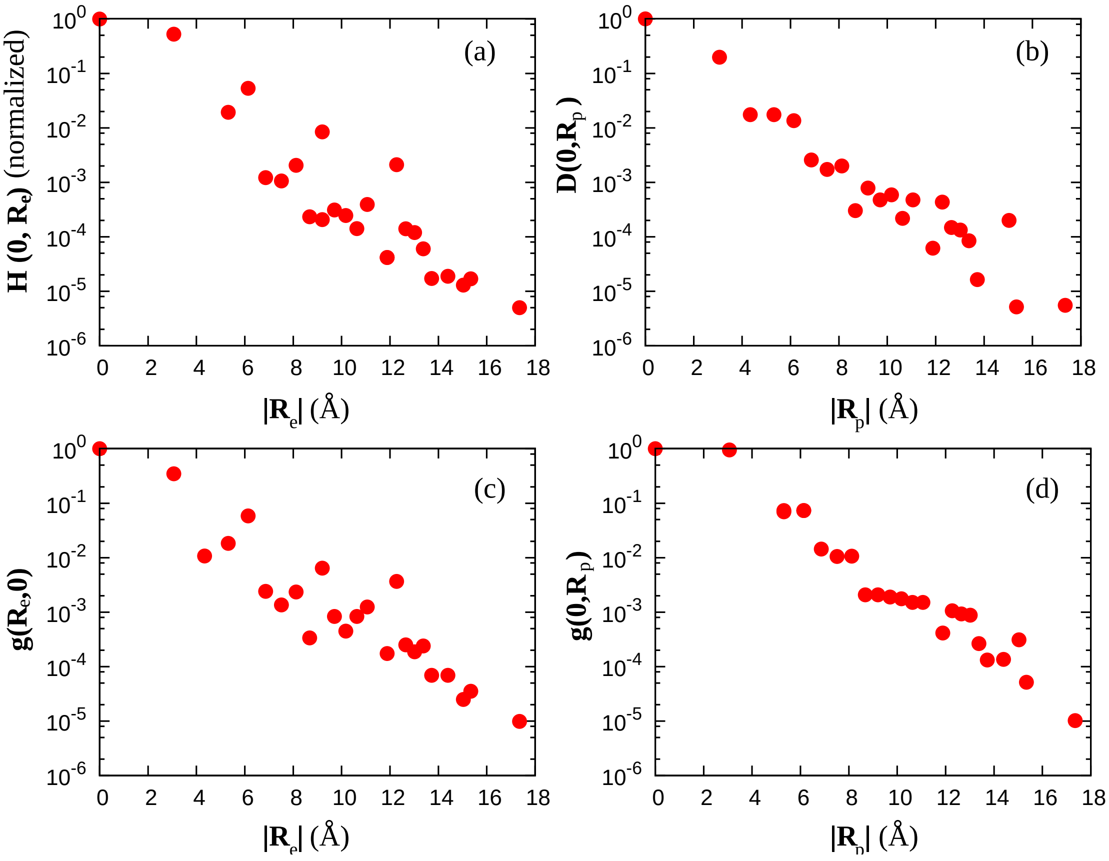

Figure 2.6: Spatial decay of the largest components of the Hamiltonian $H^{\mathrm{el}}_{\mathbf{R}_{\mathrm{e}},0}$ (a), the dynamical matrix $D^{\mathrm{ph}}_{\mathbf{R}_{\mathrm{p}},0}$ (b), and the electron-phonon matrix elements $g(0,\mathbf{R}_{\mathrm{p}})$ (c) and $g(\mathbf{R}_{\mathrm{e}},0)$ (d) for cubic hole-doped SiC. The data are plotted as a function of distance and are taken along several directions.

electron-phonon coupling strength $\lambda = 0.34$ using 250,000 **k**-points and 8000 **q**-points. The superconducting transition temperature was calculated using a Coulomb repulsion parameter $\mu^\star = 0.1$ and was found to be $T_\mathrm{c} = 1$ K. Our result is in good agreement with recent experimental data yielding $T_\mathrm{c} = 1.4$ K[72].

2.6 Conclusion

In this communication we introduced `EPW`, a computer code for calculating the electron-phonon coupling from first-principles using density functional perturbation theory and maximally localized Wannier functions. `EPW` enables extremely accurate and highly efficient calculations of the mode-resolved and total electron-phonon coupling strength, as well as phonon and electron linewidths. The code is distributed through the website `http://epw.org.uk` and is available under the terms of the GNU General Public License. Plans are in place to extend `EPW` in order to implement the anisotropic Eliashberg theory [80], the density functional theory for superconductors [81, 82], and phonon-assisted optical responses [83].

Chapter 3

Superconductivity in transition metal carbides

The discovery of superconductivity at 39 K in magnesium diboride [84] has generated a renewed interest in phonon-mediated superconductors containing light elements. Within this class of materials, carbon and nitrogen compounds have attracted considerable attention following the synthesis of alkali-doped fullerenes, layered hafnium nitride, metal-intercalated graphite, and boron-doped diamond, which have been reported to superconduct at 33 K [85], 25 K [86], 11 K [87] and 4 K [73], respectively. Among the binary carbon compounds, the carbides of the group IVb, Vb, and VIb transition metals (including WC, TiC, TaC, and HfC) exhibit exceptional mechanical properties, with Young moduli as large as 530 GPa and melting temperatures above 3000 K [88]. The mechanical hardness of transition metal carbides has been suggested to originate from bonding combinations of metal d and carbon p orbitals which strongly resist shear strain or shape change [89, 90]. If a similar mechanism were active in the superconducting pairing, combined with the large frequencies of the optical phonons ($\sim$80 meV), this would result in high superconducting transition temperatures [91]. However, experiments performed on carbides and nitrides of the groups IVb, Vb, and VIb transition metals indicate transition temperatures not exceeding 17 K [88]. It is important to understand why such a mechanism seems ineffective in the superconductivity of the carbides, and whether it can be enhanced by chemical doping in order to optimize the transition temperature.

The carbides of the groups IVb and Vb transition metals exhibit similar structural, electronic, and vibrational properties [88]. These compounds all crystallize in the rock-salt structure with similar lattice parameters. The vibrational spectra display acoustic peaks between 10-30 meV and optical peaks at 60-90 meV. Despite these similarities, group Vb transition metal carbides exhibit superconductivity in the range 7-11 K [92], while the IVb compounds have not been observed to superconduct above 0.1 K [93]. These different superconducting properties have variably been ascribed to Kohn anomalies in the vibrational spectra [94] or nesting effects of the associated Fermi surfaces [95, 96]. While those studies provided significant insight into the superconductivity of transition-metal carbides, a comprehensive study of the interplay between phonon softening, Fermi surface nesting, and carrier concentration in these materials, along with its effect on the superconducting properties, is not available.

The investigations of superconductivity in transisiton-metal carbides are performed by focusing on two representative compounds, one for each group: HfC (IVb) and TaC (Vb). Using `EPW`, we show that superconductivity in TaC relates to a nesting of the corresponding Fermi surface with large connecting wavevectors. On the other hand, in HfC the Fermi surface does not exhibit a significant nesting and the associated transition temperature is negligibly small. The microscopic mechanism of the pairing is shown to consist of the coupling of the metal d states to acoustic zone-edge vibrations. In view of optimizing the transition temperature, we study the variation of the electron-phonon coupling strength with changes in the chemical potential, as well as the onset of structural phase transitions driven by doping through phonon softening.

Calculations were performed within the local density approximation [28] to density functional theory. The valence electronic wavefunctions were expanded in a plane-wave basis with a kinetic-energy cutoff of 90 Ry, and the core-valence interaction was taken into account through norm-conserving pseudopotentials [50, 48]. The lattice dynamical properties were computed in the harmonic approximation using density functional perturbation theory [3]. Superconductivity was studied within the isotropic approximation to the Migdal-Eliashberg theory [53]. The evaluation of the electron-phonon coupling strength $\lambda_{\mathbf{q}}$ and the Eliashberg function $\alpha^2F(\omega)$ required a very dense sampling of the electron-phonon scattering processes throughout the Brillouin zone [31]. We achieved such a dense sampling by means of our first-principles interpolation scheme [38, 31] based on maximally localized Wannier functions [32].

In this work we considered 8 electronic Wannier functions spanning an energy range of ± 4 eV from the Fermi level. These correspond to 5 metal d states and 3 carbon p states. We computed the electron-phonon matrix elements starting from an initial Brillouin zone mesh with $6 \times 6 \times 6$ points, corresponding to a real-space interaction range of 27 Å between image Wannier functions in neighboring supercells [31]. The fine grid for the Brillouin zone integration consisted of $20 \times 20 \times 20$ unique points obtained by randomly translating a uniform mesh.

Figure 3.1 shows the calculated phonon dispersions for TaC and HfC along relevant high-symmetry directions in the Brillouin zone. Our calculations are in good agreement with the dispersions derived from neutron scattering experiments [97]. Pronounced softenings are observed for the acoustic branches of TaC [Fig. 3.1(c)] at wavevectors corresponding to the L point, to points at 0.7 $\overline{\Gamma\mathrm{X}}$, and 0.9 $\overline{\Gamma\mathrm{K}}$ in the Brillouin zone. Taken together, these points define a cubic Kohn-anomaly surface in the Brillouin zone [92], with the corners touching the eight L points and the faces bulging out along the Δ directions. Analogous anomalies can be observed in the vibrational spectra of the other group Vb transition metal carbides NbC and VC [97, 98]. Such a Kohn-anomaly surface is not observed in HfC, consistent with the other group IVb compounds ZrC and TiC [97, 99]. Nonetheless, close to the zone center the optical phonons of HfC appear significantly softer than what is expected on the basis of a mass scaling argument between HfC and TaC [Fig. 3.1].

The softening of the acoustic branches in group Vb carbides has been associated with the topology of the corresponding Fermi surface [95]. The Fermi surface of TaC consists of six arms extending from Γ along the Δ directions [Fig. 3.1(a)], and exhibits important nesting features associated with several wavevectors connecting the parallel faces of the arms. Together, these nesting wavevectors define precisely the Kohn-anomaly surface discussed above. In the case of HfC, the Fermi surface consists of a small spheroid centered at the Γ point and six pockets elongated along the Δ directions. The softening of the zone-center optical phonons of HfC reflects the increased electronic susceptibility for wavevectors corresponding to transitions within the spheroid and within each pocket.

In order to identify the phonons which are relevant to the superconducting pairing, we calculated the electron-phonon coupling strength $\lambda(\mathbf{q})$ [see Eq. (7.23) of Ref. [8]] using our Wannier interpolation scheme. For clarity we consider here the average coupling strength corresponding to the acoustic [$\lambda_{\text{ac}}(\mathbf{q})$] and to the optical [$\lambda_{\text{op}}(\mathbf{q})$] branches (Fig. 3.2). In the case of TaC, the primary contribution to the acoustic coupling strength arises from wavevectors belonging to the cubic Kohn anomaly surface discussed above. This finding is consistent with the observation that the electron-phonon coupling strength $\lambda(\mathbf{q})$ and the renormalization of the phonon dispersions are both related to the phonon self-energy. The optical modes of TaC appear to offer no significant contribution to the coupling strength. In the case of HfC, both the acoustic and optical branches display significant structure near the zone center, consistent with the softening discussed in relation to Fig. 3.1(d). In order to quantify the contributions arising from the acoustic and optical modes to the electron-phonon coupling strength in TaC and HfC we computed the Eliashberg spectral function $\alpha^2F(\omega)$ [53], and the corresponding isotropic coupling strength λ [Fig. 3.3]. Consistent with the analysis carried out in relation to Fig. 3.2, the optical phonons do not play any significant role in the superconducting pairing of TaC ($\lambda_{\text{opt}}^{\text{TaC}} = 0.12$) and HfC ($\lambda_{\text{opt}}^{\text{HfC}} = 0.15$). On the other hand, the acoustic phonons provide an important contribution to the pairing in the case of TaC ($\lambda_{\text{ac}}^{\text{TaC}} = 0.62$), while they remain ineffective in the case of HfC ($\lambda_{\text{ac}}^{\text{HfC}} = 0.09$). Inspection of the Eliashberg function and the phonon density of states (Fig. 3.3) shows that, in the case of TaC, the spectral weight of $\alpha^2F(\omega)$ is largely enhanced in the acoustic modes, in line with the preceeding discussion. The calculated coupling strengths can be used to obtain an estimate of the superconducting transition temperatures of HfC and TaC. For this purpose we used the McMillan equation with a Coulomb pseudopotential $\mu^\star = 0.13$ [8], and obtained $T_c = 8.3$ K for TaC and $T_c <\sim 0.01$ K for HfC, consistent with the experimental values 10.3 K and <0.015 K, respectively [88, 93].

The differences in the coupling of Fermi surface electrons to the acoustic and optical phonons in Ta and Hf carbides can be rationalized by inspecting the Wannier-projected electronic density of states [Fig. 3.4(a)]. The Fermi level of HfC lies near a minimum of the density of states, with partial $2p$ and $5d$ densities of 0.38 states/(eV cell) and 0.39 states/(eV cell), respectively. The Fermi level of TaC lies 1.35 eV above the corresponding one of HfC, with partial $2p$ and $5d$ densities of 0.24 states/(eV cell) and 0.78 states/(eV cell), respectively. Surprisingly, while the acoustic coupling in TaC is a factor $\lambda_{\text{ac}}^{\text{TaC}}/\lambda_{\text{ac}}^{\text{HfC}} \simeq 6.9$ larger than in HfC, the corresponding ratio between the partial $5d$ density of states is only $0.78/0.39 \simeq 2$. This indicates that the difference in the electron-phonon coupling strengths λ of HfC and TaC cannot be ascribed to a simple density-of-states effect. This observation is supported by the analysis of the the nesting function [Fig. 1 (e) and (f)][100] indicating pronounced features arising from the flat parallel sheets of the Fermi surface of TaC, superimposed to the characteristic $1/q$ background.

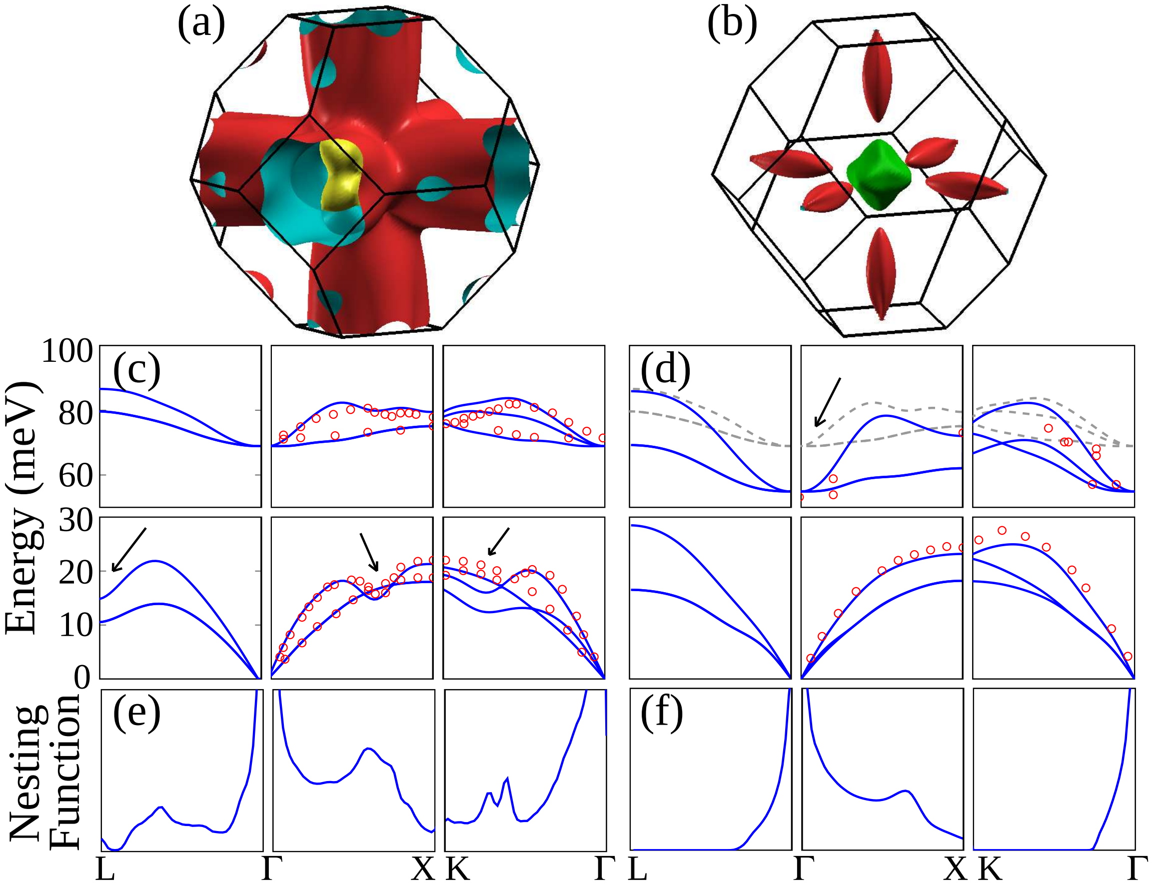

Figure 3.1: (Color online) Top: Fermi surfaces of (a) TaC and (b) HfC, Middle: phonon dispersions of (e) TaC and (f) HfC (solid lines), together with the experimental data of Ref. [97] (circles). The dashed lines in (d) correspond to the dispersions of TaC after rescaling the Ta mass to the Hf value. The arrows indicate the wavevectors exhibiting Kohn anomalies. Bottom: Nesting functions of (e) TaC and (f) HfC (arbitrary units).

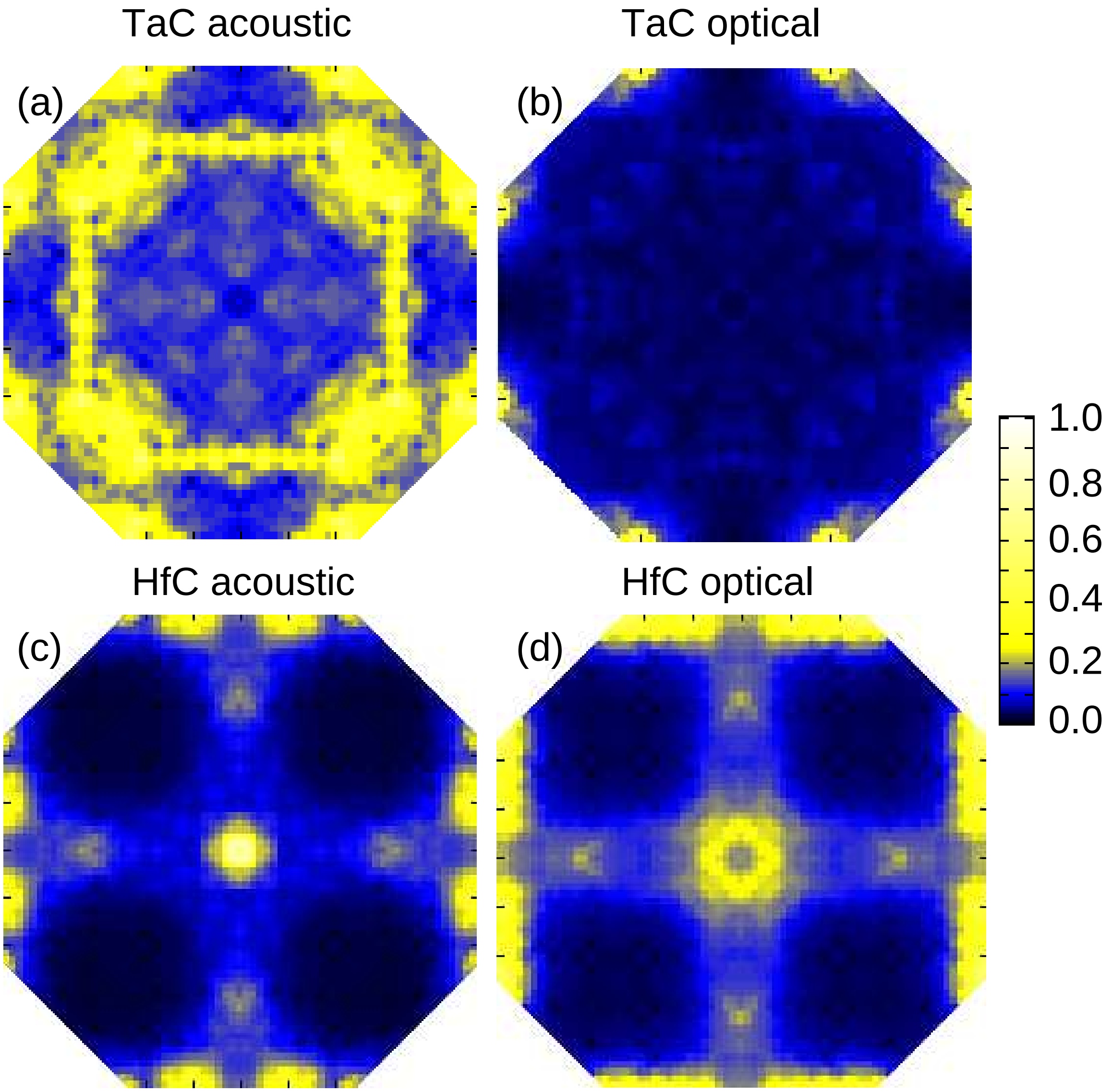

Figure 3.2: (Color online) Intensity plot of the electron-phonon coupling strength $\lambda(\mathbf{q})$ in the $\mathbf{q} = (q_x, q_y, 0)$ plane of the Brillouin zone. Top: average electron-phonon coupling strength in TaC for acoustic (a) and optical (b) modes. Bottom: average coupling strength in HfC for acoustic (c) and optical (d) modes.

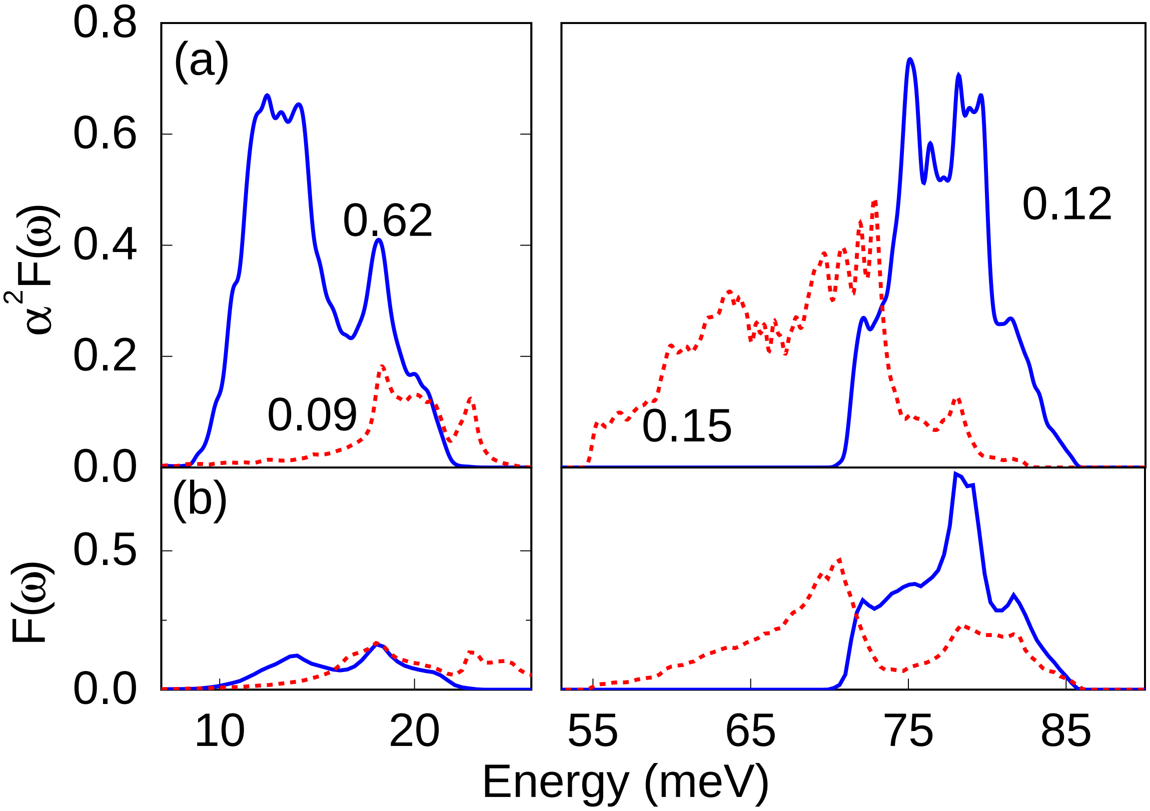

Figure 3.3: (Color online) (a) Eliashberg function $\alpha^2F(\omega)$ for TaC (solid) and HfC (dashed). We show the partial contributions to the electron-phonon coupling strength λ next to each curve. (b) The corresponding vibrational density of states $F(\omega)$ in units of modes per meV per unit cell.

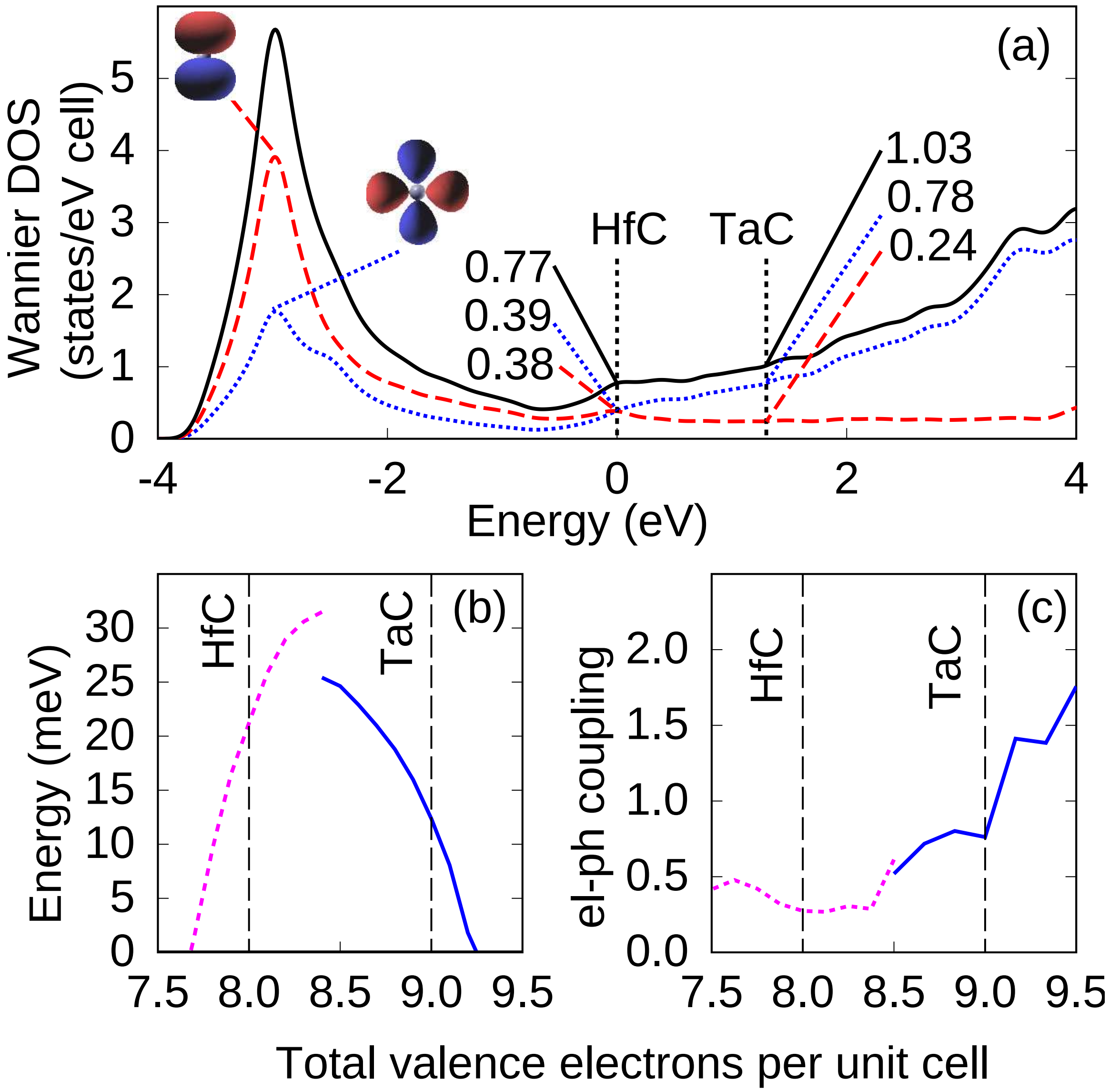

Figure 3.4: (Color online) (a) Wannier-projected density of states for TaC and HfC: C-$2p$ (dashed) and metal-$5d$ (dotted) partial density of states, and total density of states (solid). The vertical lines denote the Fermi levels of HfC and TaC. (b) Phonon softening vs. doping in HfC (dashed) and TaC (solid): shown is the doping-dependent frequency of the softest mode for each material. (c) Electron-phonon coupling λ as a function of electron concentration for HfC (dashed) and TaC (solid).

These results allow us to outline the following picture of the electron-phonon interaction and the superconducting pairing in the transition metal carbides HfC and TaC: (i) the optical modes do not couple significantly to the Fermi surface electrons. This behavior results from the small mass ratio between the carbon and the metal atoms ($m_{\mathrm{C}}/m_{\mathrm{Hf,Ta}} \simeq 1/15$, which implies that optical vibrations involve primarily the C atoms), as well as from the small partial density of $2p$ states at the Fermi level. (ii) The acoustic modes mainly couple to the metal $5d$ electrons. This follows from the large $5d$ density of states at the Fermi level, and the fact that acoustic modes involve significant displacements of the metal atoms. (iii) The Fermi surface of TaC offers significant phase space for electron-phonon scattering with large wavevectors, $q \sim 0.7$ (we adopt reciprocal lattice units throughout), while (iv) in the case of HfC the nesting vectors are considerably smaller in magnitude, $q <\sim 0.2$, and the associated phase space is negligible. Therefore, while a similar atomistic mechanism operates in both HfC and TaC, the different Fermi surface topology leads to substantially different electron-phonon interaction strengths. These observations indicate that the superconductivity in TaC arises from the coupling of metal d states to acoustic phonons with large wavevectors, and is strongly enhanced by a pronounced Fermi surface nesting. As a consequence, the mechanical hardness of this compound, for which carbon p states play a crucial role [89], appears to be essentially unrelated to the superconductivity.

The understanding developed so far allows us to discuss directions for optimizing the superconducting transition temperature of super-hard carbides. Due to the close connection between the Fermi surface topology and the superconductivity in these compounds, we consider the possibility of optimizing the Fermi surface nesting via substitutional doping. The similarity between the band structures of HfC and TaC suggest that a simple rigid-band model should be suitable for discussing trends. Since a change in the electron concentration will induce a renormalization of the phonon dispersions, we calculated the renormalized vibrational frequencies to identify the stability range of the lattice. Figure 3.4(b) shows that the addition of 0.32 el/cell to TaC results into a lattice instability driven by a soft longitudinal acoustic (LA) phonon with wavevector $\mathbf{q} = (0.75, 0, 0)$. On the other hand, a lattice instability associated with a $\mathbf{q} = (0.16, 0.50, 0.64)$ soft LA mode develops in HfC following the removal of 0.41 el/cell. The instability of electron-doped TaC predicted here is consistent with the fact that stoichiometric group VIb WC is not observed in the cubic structure [88]. Figure 3.4(a) shows that in order to enhance the contribution of the p-states to the electron-phonon coupling, the Fermi level should lie 3 eV below the one of undoped HfC. However, the hole-doping required to produce such a Fermi level shift is well beyond the threshold for the onset of the lattice instability [Fig. 3.4(b)]. In Fig. 3.4(c) we show the electron-phonon coupling strength λ recalculated for both HfC and TaC after varying the electron concentration. We calculated the renormalization of the vibrational frequencies using the real part of the phonon selfenergy in the Migdal approximation [38]. Within the stability range of the respective lattices, Fig. 3.4 shows that the coupling strength of HfC is not very sensitive to the doping, while for TaC it can reach values as high as $\lambda = 1.4$ at the onset of the instability. Using this result with the McMillan equation we find that electron-doping of TaC may increase the superconducting transition temperature up to 23K.

We have shown that the atomistic origin of the superconducting pairing in HfC and TaC resides in the coupling of the transition metal *d* electrons to acoustic phonons. The large difference in the interaction strengths between group IVb HfC and Vb TaC results from the pronounced nesting of the Fermi surface in TaC. Since the other carbides of IVb and Vb transisition metals are isoelectronic to HfC and TaC and exhibit similar lattice dynamical properties, the mechanisms identified in the present work are expected to apply to the entire class of transition metal carbides. More generally, the present study shows that the understanding and design of phonon-mediated superconductors involving light elements and transition metals requires a fine analysis of the delicate interplay between phonon softening, carrier concentration, and Fermi surface topology.

Chapter 4

Superconductivity in boron-doped SiC

Silicon carbide is a promising material for a variety of emerging applications. Its large bandgap, high breakdown field, and high melting point make it ideal for uses in high-power devices, radiation tolerant electronics [101], and optoelectronics [102]. Recent observations of superconductivity in B-doped samples of 3C-SiC [103] introduce the possibility of additional technological applications for this material.

The superconducting properties of semiconductors were predicted several decades ago [75], and the discovery of superconductivity in boron-doped diamond [73] and silicon [104] sparked significant interest in this research area. The critical temperature of doped diamond has been raised above 11 K since the original discovery [105]. However, diamond-based devices are still impractical for applocations [106]. On the other hand, although silicon electronics benefits from a well-established industrial infrastructure, B-doped silicon undergoes a phase transition to the superconducting state at the very low temperature of 0.3 K, and the gas immersion laser method used to achieve the required levels of doping is a challenging technique [104]. Within this framework, silicon carbide stands as a promising compromise between the former two materials: (i) the infrastructure for producing SiC is already well established and (ii) boron-doping can be achieved without major difficulties.

In this chapter we investigate from first-principles the origin of superconductivity in boron-doped silicon carbide. First, we study the electron-phonon coupling strength in the cubic polytype 3C of silicon carbide by simulating the hole-doping through a rigid-band model. Then, we consider the electron-phonon interaction in a supercell model of the 3C-SiC to validate our results. Finally, we determine the relative strength of the electron-phonon coupling in different polytypes of silicon carbide. Our investigation indicates that the total coupling strength ranges from $\lambda = 0.21$ to $\lambda = 0.34$ among all polytypes considered. Using the McMillan equation with Coulomb parameter $\mu^* = 0.1$ [67], we obtain superconducting transition temperatures between 0.01 K and 1.1 K, in good accord with experimental data.

SiC polytypes consist of tetrahedrally bonded silicon and carbon atoms. The structural difference among the polytypes results from the stacking of the silicon-carbon tetrahedra along the *c*-axis. For example, the stacking in 2H-SiC corresponds to a periodicity of two layers of Si and C (AB), while the stacking in 6H-SiC corresponds to a periodicity of six layers (ABCACB). In this work we first discuss the cubic polytype 3C-SiC because the superconducting samples in the experiment of Ref. [103] were reported to be primarily of the 3C type. We then extend our investigation to the 4H-SiC and the 6H-SiC polytypes which are important for device applications [107, 108].

In the original experiment of Ref. [103] 3C-SiC samples were synthesized with a 4% concentration of boron. Structural analysis indicated that B dopants substitutionally replaced the C atoms. In our calculations we considered two distinct doping levels. First, we studied 3C-SiC with a realistic boron concentration of 3.7%. In this case we explore both a rigid band model (for the electronic structure, the lattice dynamics, and the electron-phonon interaction, model I-RB in the following) and a $3 \times 3 \times 3$ supercell model (for the electronic structure, model I-SC). Then, we studied 3C-SiC with a B concentration of 12.5%, substantially larger than in the original experiment [103]. In this latter case we compared again a rigid band model (model II-RB) with a $2 \times 2 \times 2$ supercell model (for which we studied the electronic structure, the lattice dynamics, and the electron-phonon coupling, model II-SC). The calculations for the other polytypes were all performed within the rigid-band approximation. We described the electronic structure using the local density approximation [29, 51] to density functional theory, within a planewave pseudopotential scheme [28, 50, 48]. We calculated the lattice dynamical properties using density-functional perturbation theory [3], and the electron-phonon coupling parameter using an interpolation scheme [31] based on maximally-localized Wannier functions [32, 33]. We used a plane-wave kinetic energy cutoff of 60 Ry, and Brillouin-zone coarse grids with 29 irreducible points for the electron-phonon calculation. The electronic energies, phonon frequencies, and electron-phonon matrix elements were interpolated according to Ref. [31]to grids containing 8000 (1000) unique phonon wavevectors and 125000 (8000) unique electron wavevectors for the rigid-band (supercell) models.

Figure 4.1 shows a comparison between the band structures of 3.7% B-doped 3C-SiC calculated within the rigid band model, I-RB, and within the supercell model, I-SC. In both cases, the doping has the effect of lowering the Fermi level below the top of the valence band. As a result, a small multi-sheet Fermi surface emerges around the center of the Brillouin zone. Importantly, the dopants do not introduce localized states in the band gap. The close similarity between the electronic bands of model I-RB and model I-SC around the Fermi level provides a justification for the use of the rigid-band approximation to describe the electronic structure of B-doped SiC. This finding is analogous to what had already been observed in the case of B-doped diamond [79, 38]. Our results are consistent with previous experimental work on SiC showing that the Mott metal-to-insulator transition occurs at a hole-doping concentration of 10^{21} cm^{-3} [109]. In fact, the dopant concentration considered here, corresponding to a hole concentration of 2×10^{21} cm^{-3}, clearly lies within the metallic regime, consistent with Fig. 4.1.

Figure 4.2 shows the phonon dispersions calculated for pristine and for hole-doped 3C-SiC. In the case of pristine 3C-SiC, the calculated phonon dispersions are in good agreement with the experimental data of Ref. [110]. In particular, we find a splitting of 23 meV between the longitudinal optical (LO) and the transverse optical (TO) phonons at the Γ point, in accord with the measured value of 21 meV. In order to discuss the lattice dynamics of B-doped SiC, we first present our results for model I-RB and then extend our

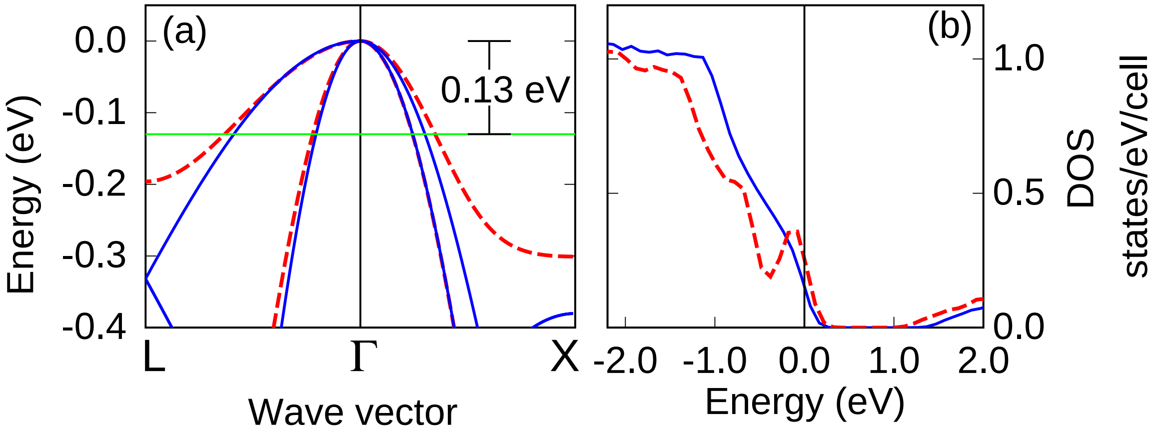

Figure 4.1: (Color online) (a) Band structure of 3.7% B-doped 3C-SiC: model I-RB (solid blue lines) and model I-SC (dashed red lines). The zero of energy is set to the top of the valence bands, and the Fermi level is indicated by the horizontal line. (b) Electronic density of 3.7% B-doped 3C-SiC: model I-RB (solid blue line), and model I-SC (dashed red line). The density of states at the Fermi level is similar in the two models (0.18 states/eV/cell in model I-RB and 0.23 states/eV/cell in model I-SC). In the supercell model we do not find impurity states within the band gap.

discussion using models II-RB and II-SC. In model I-RB, upon doping the LO-TO splitting is closed by the metallic screening and the optical phonons become degenerate at the zone center. From pristine to hole-doped SiC the TO mode at Γ is softened by 5.5 meV and the LO mode by 26.5 meV, similarly to the cases of boron-doped diamond [111] and silicon [104]. The dispersions throughout the rest of the Brillouin zone are only weakly affected by the doping. This is also similar to the case of boron-doped diamond where the optical phonons are softened only if their wavevector is smaller than $\sim 2k_{\mathrm{F}}$ (k_{F} is the average radius of the Fermi surface in reciprocal space) [77, 38]. In Refs. [79, 38] it was pointed out that B-doped diamond exhibits partially localized vibrational modes associated with the dopant. These modes give rise to a nondispersive feature below the optical branches [38] and cannot be described by a rigid-band model. In order to check for the existence of those modes in the case of SiC, we un-folded the phonon dispersions of the supercell model II-SC into the Brillouin zone of pristine SiC following Ref. [38]. Figure 4.2 indicates that the acoustic modes of the II-RB and II-SC models align closely. The branch splitting at zone-edges arises from the impurity potential in the heavily doped supercell. As in the case of boron-doped diamond, the optical modes exhibit a non-dispersive feature below the optical branches, associated with localized motion around the boron atoms. However, in contrast to the case of B-doped diamond, the impurity branch has negligible contribution to the total electron-phonon coupling [cf. the Eliashberg spectral function in Fig. 4.2(d)]. This finding indicates that a rigid-band model is appropriate to describe the electron-phonon interaction in B-doped SiC.

Figure 4.3 shows the Eliashberg spectral function $\alpha^2F(\omega)$ for model I-RB, calcu-

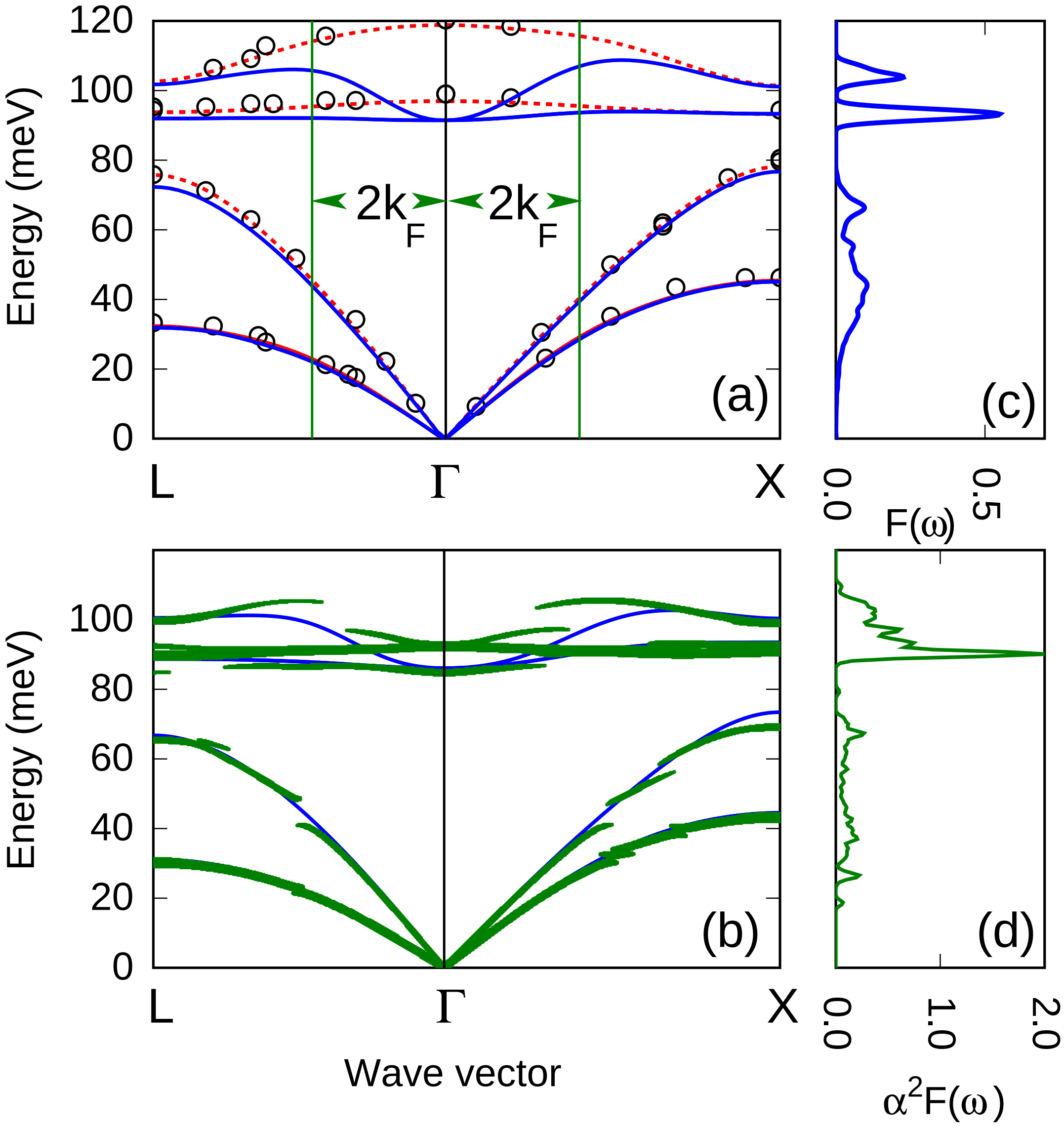

Figure 4.2: (Color online) (a) Phonon dispersions of pristine (dashed red lines) and B-doped (solid blue lines) 3C-SiC along the Λ and the Δ directions of the Brillouin Zone. The vertical (green) lines indicate the average Fermi surface diameter. Open circles are experimental data [110]. (b) Phonon dispersions for heavily B-doped 3C-SiC: model II-RB (solid blue lines) and model II-SC (green points, after folding into the Brillouin zone of pristine SiC, following Ref. [38]). (c) Phonon density of states for model I-RB. (d) The Eliashberg spectral function for 12.5% B-doped 3C-SiC (model II-SC). The nondispersive branch around 80 meV in (b) does not contribute to the Eliashberg spectral function.

lated using Eq. [7] of Ref. [31]. The Eliashberg function exhibits two sharp peaks at the energies of 92 meV and 106 meV, associated with the Van Hove singularities in the phonon dispersion relations (cf. Fig. 4.2). In addition to the optical peaks, a broad although less pronounced feature appears in the acoustic energy range. Interestingly, the coupling of electrons to the acoustic phonons is negligible above 40 meV, despite the non-vanishing vibrational density of states [Fig. 4.2(c)]. This can be understood by considering that the wavevector of acoustic phonons with energy in excess of 40 meV is larger than $\sim 2k_{\rm F}$ [cf. Fig. 4.2(a)], hence they cannot promote electronic transitions within the Fermi surface. At variance with this finding, in the heavily-doped case (model II-SC) there is some noticeable contribution of high-energy acoustic phonons to the Eliashberg function, corresponding to a wider Fermi surface [Fig. 4.2(d)].

The first reciprocal energy moment of the Eliashberg spectral function provides the electron-phonon coupling parameter $\lambda = 2\int \omega^{-1}\alpha^2 F(\omega)$. For model I-RB of 3.7% B-doped 3C-SiC we find a coupling parameter $\lambda = 0.34$. The coupling of the electrons to the acoustic phonons accounts for 70% of the total coupling strength. This result is qualitatively different from the cases of B-doped diamond and silicon, where the coupling to the acoustic modes accounts for less than 25% of the total electron-phonon coupling strength, as found by integrating the spectral functions of Refs. [38, 74]. Furthermore, we find that the Eliashberg function of B-doped 3C-SiC can be reproduced quite accurately by taking the electron-phonon matrix element g constant and equal to 95 meV [dashed line in Fig. 4.3]. This indicates that superconductivity in SiC is dominated by the geometry of the Fermi surface and by the vibrational density of states, as opposed to the coupling of electrons to specific vibrational modes as it is the case in diamond [79, 38]. A band-by-band decomposition of the coupling parameter reveals indeed that intraband scattering processes within the largest Fermi surface of 3C-SiC [112] are favored by the peculiar nesting features of this surface, and provide the dominant contribution to the pairing. This mechanism has not been observed for B-doped diamond [76].

The superconducting transition temperature corresponding to the calculated electron-phonon coupling parameter is obtained using the modified McMillan equation [67]. The average logarithmic phonon frequency [Eq. (14.2) of Ref. [53]] is $\omega_{\rm log} = 63$ meV, considerably smaller than the one calculated for B-doped diamond in Ref. [38] (125 meV). The relatively small logarithmic frequency results from the large contribution of the acoustic phonons in SiC, which enhances the weight of the Eliashberg function in the low-frequency range. Depending on the choice of the Coulomb parameter μ^*, the calculated superconducting transition temperature varies between 0.09 K ($\mu^* = 0.15$) and 1.1 K ($\mu^* = 0.1$). The latter value compares favorably with the measured transition temperature of 1.4 K. These results indicate that the experimentally observed superconductivity in SiC can be explained with an electron-phonon coupling mechanism.

In order to validate our results based on the rigid-band model I-RB, we performed additional calculations for the heavily doped rigid-band (II-RB) and supercell (II-SC) models of B-doped SiC. In these latter models we consider a very large boron concentration of 12.5% (not yet achieved in experiment) in order to compare the rigid-band approach and the supercell approach in a limiting situation The electron-phonon coupling parameter was found to be $\lambda_{\rm II-RB} = 0.44$ for model II-RB and $\lambda_{\rm II-SC} = 0.46$ for model II-SC. Inspection

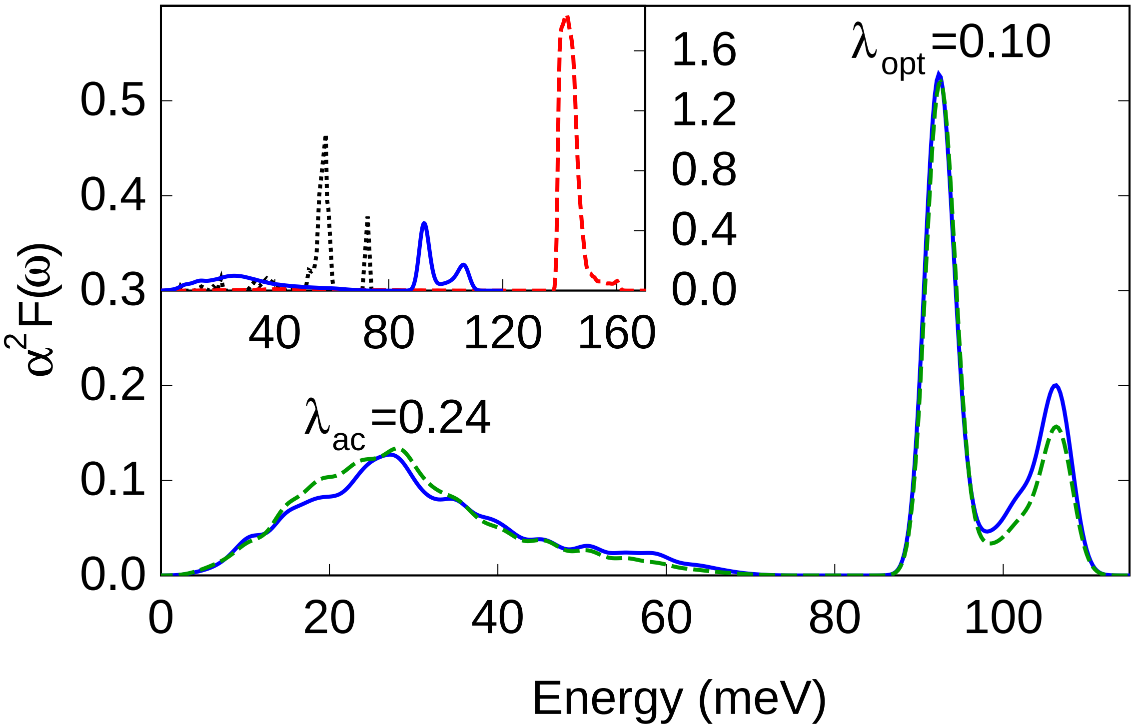

Figure 4.3: (Color online) Eliashberg function $\alpha^2F(\omega)$ for model I-RB of 3.7% B-doped 3C-SiC (solid blue line). We also show the Eliashberg function obtained using a constant electron-phonon matrix element g =95 meV for comparison (dashed green line). (inset) Comparison between the Eliashberg functions of B-doped SiC (solid blue line, model I-RB), diamond (dashed red line, from Ref. [38]) and silicon (dotted black line, from Ref. [74]). The contribution of the acoustic phonons to the electron-phonon coupling parameter is significant in SiC, whereas it is small or negligible in diamond and silicon.

	3C	2H	4H	6H
$\lambda_{\rm ac}$	0.24	0.15	0.12	0.14
$\lambda_{\rm opt}$	0.10	0.09	0.09	0.07
$\lambda_{\rm tot}$	0.34	0.24	0.21	0.21
$T_{\rm c}$(K)	1	0.01	0.001	0.001

Table 4.1: Electron-phonon interaction strength in various polytypes of 3.7% doped SiC. We show the total coupling strength ($\lambda_{\rm tot}$), as well as the contributions arising from the acoustic ($\lambda_{\rm ac}$) and the optical ($\lambda_{\rm opt}$) phonons. The superconducting transition temperature ($T_{\rm c}$, in K) is estimated using the McMillan formula with a Coulomb parameter $\mu^* = 0.1$. The calculations on the hexagonal poly-types have been performed using a rigid band model. The accuracy in the calculated coupling parameters $\lambda_{\rm tot}$ is the same across different polytypes, while the $T_{\rm c}$ values depend exponentially on $\lambda_{\rm tot}$ and are shown purely for comparison purposes.

of the Eliashberg function for models II-RB and II-SC reveals no significant differences in the sources of coupling for these two models. The close agreement between the rigid-band and the supercell calculation provides an a posteriori justification for our choice of modeling 3.7% B-doped 3C-SiC within a rigid-band approximation. Interestingly, the superconducting transition temperatures of the heavily-doped models II-RB (5.1 K for $\mu^* = 0.1$) and II-SC (6.3 K for $\mu^* = 0.1$) are found to be above the boiling-point of liquid helium. This result bears potential implications for practical uses of superconducting SiC.

After discussing the mechanism of superconductivity in 3C-SiC, we now extend our investigation to the 4H- and 6H-SiC polytypes which are of interest for applications, and to the 2H-SiC polytype for completeness. For each of these polytypes the valence band maximum occurs at the zone-center, and the B doping gives rise to a multi-sheet Fermi surface around Γ of similar topology. Our calculations indicate that the electron-phonon coupling in the polytypes 2H-, 3C-, 4H-, and 6H-SiC occur in the range $\lambda = 0.21 - 0.34$ for comparable levels of doping (Table 4.1). The electron-phonon coupling strength associated with the optical modes is very similar for all of the polytypes ($\lambda = 0.07 - 0.10$). This is consistent with the fact that optical phonons around the zone-center correspond to bond-stretching vibrations which are sensitive to the short-range structure, which is the same in all polytypes. In contrast, the coupling to low energy acoustic phonons exhibits a larger variation ($\lambda = 0.12 - 0.23$) and is enhanced in 3C-SiC. We assign this variation to the differences in the shape of the Fermi surfaces among the polytypes (some leading to a more pronounced nesting).

Recently, a metal-insulator transition has been observed in Al-doped SiC [113], raising the question as whether electron doping of SiC could be a more convenient strategy to increase its superconducting transition temperature. In order to address this question we have calculated the electron-phonon coupling parameter of Al-doped SiC within the rigid-band approximation. The coupling parameter is found to be smaller than in B-doped SiC for comparative levels of doping ($\lambda = 0.15$ for 5% Al doping and $\lambda = 0.29$ for 15% Al doping), indicating that hole-doping is more advantageous in view of optimizing superconduтivity in SiC.

In conclusion, we investigated the origin of superconductivity in boron-doped silicon carbide from first-principles by considering a large set of structural models. We find that superconductivity arises from conventional phonon-mediated pairing. The transition temperature ranges from 1.1 K (for a B concentration of 3.7%) to 6.3 K (12.5%). In contrast to the related B-doped Si and diamond systems, acoustic phonons and Fermi surface nesting play a prominent role in the superconductivity of SiC. Our study suggests that heavily-doped cubic SiC may be a potential candidate for technological uses of superconducting semiconductors.

Chapter 5

The role of the dopant in the superconducting Fe-pnictides

Sparked by the discovery of superconductivity at 26 K in LaFeAsO$_{1-x}$F$_x$ [114], iron-based superconductors have become the subject of intense study both experimentally and theoretically. The iron-pnictide superconductors exhibit surprisingly high superconducting transition temperatures, surpassing any other materials but the cuprates.

Initial calculations suggest that the superconductivity of the iron-pnictides does not originate from a conventional electron-phonon coupling mechanism [115]. Nonetheless, a significant phonon softening has recently been observed using inelastic X-ray scattering [116], hinting at the possibility of strong electron-phonon interaction for some specific modes. The mechanism whereby the doping with fluorine alters the lattice dynamics of the iron pnictides is unknown, and calls for a thorough theoretical analysis.

Prior theoretical investigations of the lattice dynamics and electron-phonon coupling in these materials have been based on virtual crystal (VC) models of the fluorine-doping [115, 117]. The use of VC models is advantageous since taking into account the F doping explicitly using a supercell is computationally demanding. Unlike the cuprates where doping of the parent material induces an insulator-to-metal transition [118], in this system the parent compound LaFeAsO is already metallic (albeit a poor metal) [119]. Therefore, no dramatic changes are expected upon doping within the VC approximation. However, the F-doped compound LaFeAsO$_{1-x}$F$_x$ exhibits a superconducting transition for $x \approx 0.03$ [114]. This raises the question as to whether the VC description of the lattice dynamics and the electron-phonon coupling in doped LaFeAsO captures all of the relevant physics at play.

In this chapter, we explore the effects of doping of LaFeAsO through fluorine on the electronic structure, lattice dynamics and electron-phonon coupling. We take explicitly into account the fluorine doping through a large supercell [120]. We explain the origin of the recently measured phonon softening [116] and confirm previous virtual crystal results on the strength of electron-phonon coupling. Our supercell model shows that the location of the additional charge density in the doped superconductor differs dramatically from what could be expected based on simplified VC models. Indeed, the excess charge does not localize in the Fe-As layer similarly to the doping of the Cu-O plane in the cuprate superconductors. Instead the doped charge is distributed througout the unit cell, and a slight *deficit* of electrons is observed on the Fe plane.

For this study, $\mathrm{LaFeAsO}_{1-x}\mathrm{F}_x$ has been described using a supercell model for which $x = 0.125$, close to the optimal doping concentration for superconductivity [114]. We considered a system corresponding to $2 \times 2 \times 1$ unit cells of the parent compound and replaced one O atom by a F atom. The ground state electronic structure was calculated using density functional theory within the local density approximation (LDA) [29, 51], employing plane-wave basis sets[121] and ultra soft pseudopotentials [52]. A kinetic energy cutoff of 40 Ry was used for the wavefunctions and a kinetic energy cutoff of 240 Ry was used for the augmented charge density. The lattice dynamical properties were calculated using density-functional perturbation theory [3]. The parent compound is formed by a tetragonal lattice of $P4/mm$ symmetry with relaxed lattice constants $a = 4.02$ Å, $c = 8.73$ Å. The two relaxed Wyckoff parameters were $z = 0.64$, 0.14.

In the case of the doped supercell, a full relaxation of the lattice parameters and the atomic coordinates was carried out. The unit-cell volume of the doped system differed by less than 4% from the undoped compound, the lattice parameters being $a = 3.99$ Å and $c = 8.52$ Å. The most significant structural change corresponded to the nearest neighbor distances between the F atom and its neighboring O atoms. Indeed, the F-O nearest neighbor distances decreased by 2.0% upon doping from 2.665 Å to 2.614 Å.

Figure 1 shows the change $\Delta n(z)$ in the ground state charge density distribution of LaFeAsO resulting from fluorine doping. The charge density in the unit cell is integrated over the xy-plane, as the material is nearly two dimensional. The integral of $\Delta n(z)$ over one LaFeAsO unit cell (which includes two formula units) yields 0.125×2 additional valence electrons. Upon doping the Fermi energy shifts upwards by less than 0.1 eV. The associated electronic states are mostly of Fe-3d and As-4p character, in agreement with Ref. [117]. The most significant changes in the charge density distribution upon doping are observed in the interstitial regions between the La layer and its neighboring As and O:F layers. These changes arise primarily from a relaxation of the La atoms, whereby the La semi-core states move towards the As layer. Additional electronic charge is also present on the O:F layer. The additional charge arises from atomic-like electronic states which are localized around the F atoms and have energies 7.5 eV below the Fermi level. The most interesting aspect of the charge density distribution in the doped system is the electron *depletion* directly on the plane containing the iron atoms. This unexpected result indicates that models which describe the F-doping by assuming a concentration of free electrons on the 2-dimensional Fe-plane do not capture an important aspect of the physics of iron-based superconductors. In order to observe this effect it is crucial to take explicitly into account the F dopants in the calculations. Indeed, a calculation which describes the doping through a rigid-band model shows that the additional electrons are distributed uniformly across the c-axis and no electron depletion regions are observed (cf. Fig. 1).

Figure 2 displays the difference between the calculated phonon densities of states of F-doped LaFeAsO and the undoped compound. This difference is compared to the measured difference between the density of states of the similar compounds NdFeAsO and its doped counterpart $\mathrm{NdFeAsO}_{0.85}\mathrm{F}_{0.15}$ as obtained by inelastic x-ray scattering (IXS) [116]. The phonon spectra of LaFeAsO and NdFeAsO are expected to be in close agreement as the

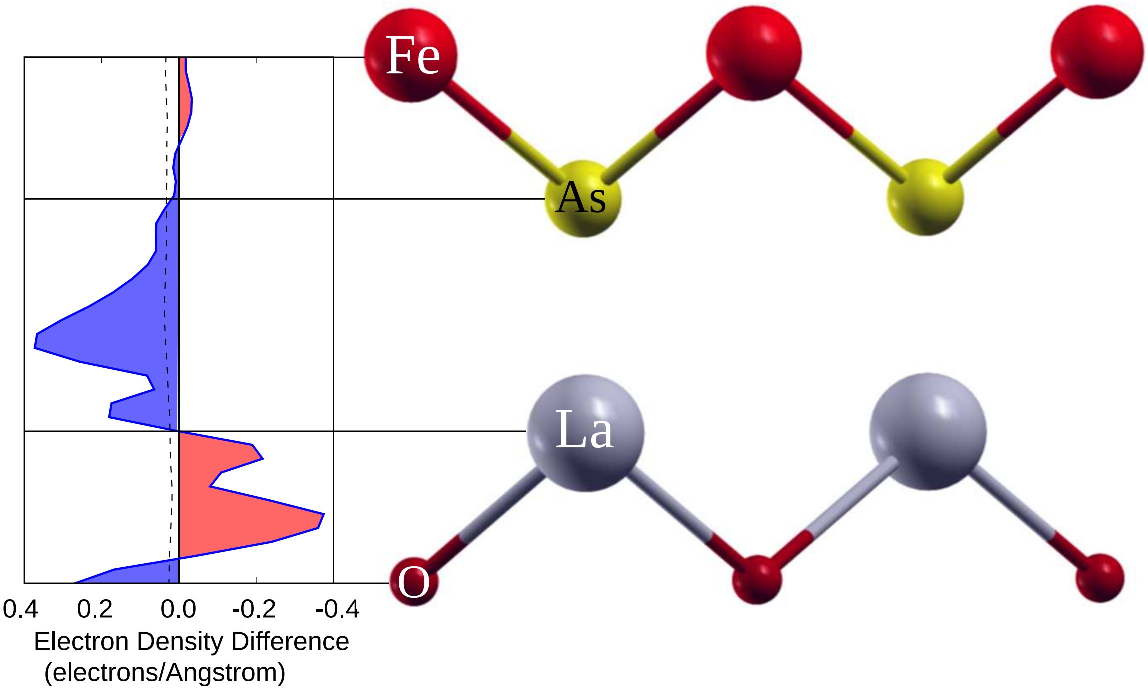

Figure 5.1: (Color Online) The planar integrated difference in the charge density between undoped and F-doped LaFeAsO (x=0.125). Positive values (blue) correspond to excess electrons, negative values (red) denote holes. The charge redistribution mostly takes place away from the Fe atoms in the interstitial region and near the F dopants. A net depletion of electrons on the iron layer is observed. The light dashed line indicates the distribution of the doped electronic charge within a rigid-band model.

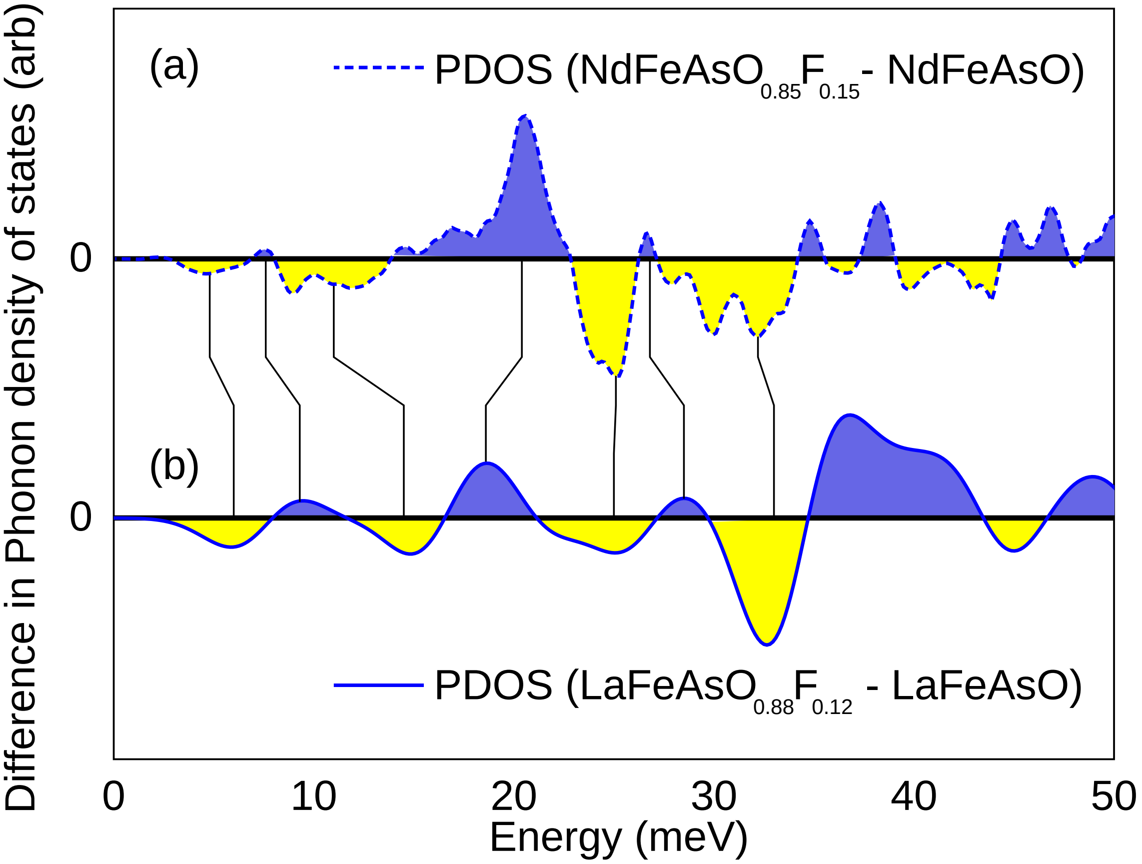

Figure 5.2: (Color online) (a) Experimental difference between the phonon density of states of undoped and F-doped NdFeAsO [116] (dashed line). (b) Calculated difference between the phonon density of states of LaFeAsO and LaFeAsO$_{0.88}$F$_{0.12}$ (solid line). Differences in the high-energy portion of the spectrum are suppressed in the experiment because of the smaller IXS scattering cross sections of O and F.

two parent compounds share the same structure, their lattice constants differ by less than 2% [122], and the masses of the respective rare-earth element differ by only 4%. In the case of NdFeAsO, a softening of the phonons with energies near 21 meV is observed in the IXS experiment of Ref. [116]. Our calculations reveal a very similar softening in the case of LaFeAsO. Analysis of the vibrational modes indicates that this feature is associated with vibrations involving predominantlty La and As motion along the c-axis. This softening can be assigned to the modified bonding arrangement in the La/O:F layer. Indeed, the in the doped system La atoms are displaced by as much as 0.08 Å along the c-axis as compared to the pristine material. Analogously, most of the observed changes in the phonon density of states can be explained in terms of lattice deformation upon doping.

In order to investigate the difference between VC models and our supercell model we additionally calculated the phonon dispersions for LaFeAsO within a rigid-band approximation. Interestingly, the phonon dispersions of the rigid-band model do not show any appreciable difference with respect to the undoped compound. This indicates that the slight perturbation to the Fermi surface under a rigid-band doping has a negligible effect on the lattice dynamics of the system. The present result highlights the importance of taking explicitly into account the F dopants for a correct description of the lattice dynamics in the superconducting phase.

We further investigated the strength of the electron-phonon interaction in F-doped LaFeAsO. The electron-phonon matrix elements were calculated from first principles using the standard prescriptions [123, 124]. No significant electron-phonon matrix elements arising from F-specific modes or any relevant phonon at finite wavevector were observed. The rigid-band model and the the supercell model were found to exhibit similar electron-phonon matrix elements and Fermi surfaces. The fact that the phonon softening is observed only in the supercell model while the electron-phonon interaction strength appears similar in the two models confirms that the observed phonon softening does not arise from electron-phonon coupling effects. Instead, this feature must be assigned to the structural deformations which accompany the substitutional replacement of O atoms by F atoms.

Figure 3 compares the calculated phonon dispersion curve along the $\Gamma - X$ high symmetry line of undoped LaFeAsO and F-doped LaFeAsO. The phonon dispersions of the supercell model in the Brillouin zone of the undoped material are obtained by means of the Brillouin-zone unfolding procedure used in Ref. [38]. For each wavevector considered in the Brillouin zone of the undoped compound, we determined the corresponding folded vector in the Brillouin zone of the supercell, and then we removed spurious modes by projecting the vibrational eigenmodes of the supercell model onto those of the undoped compound. The projection intensity at a specific **q**-vector and frequency is given by:

$$I_{\mathbf{q}}(\omega) = \sum_{\nu,\nu'} \delta(\omega_{\mathbf{q}\nu} - \omega) \left| \sum_{\tau\sim\tau'} \mathbf{u}_{\mathbf{q}}^{\nu'\tau'} \cdot \mathbf{e}_{\mathbf{q}}^{\nu\tau} e^{i(\mathbf{q}\cdot(\tau'-\tau))} \right|^2 \tag{5.1}$$

In Eq. (5.1) $\omega_{\mathbf{q},\nu}$ is the frequency of a phonon with wavevector **q** and branch index ν of the doped cell. The Bloch-periodic component of the vibrational eigenmodes in the doped system are $|e_{\mathbf{q}\nu,\tau}\rangle$, and $|u_{\mathbf{q}\nu',\tau'}\rangle$ are the eigenmodes of the undoped system. τ and τ' are the atomic labels in the two systems, respectively.

The phonon dispersions of pristine and doped LaFeAsO differ most significantly for vibrational modes at high energy which involve the motion of the oxygen and fluorine atoms. This is attributed to the structural relaxation of the O-layer in the presence of F as well as to the the mass difference between the oxygen and fluorine atoms.

The remaining phonon modes, which involve mostly the Fe-As layer and the La atoms, retain similar dispersions, although they are pertubed by the F-substitution. Denegeracies are lifted by the broken symmetry induced by the dopants. For example, the degenerate zone edge phonons at ~ 29 meV are split by 2 meV in the doped system. Comparison of the zone center modes between the undoped and doped systems shows an overall *increase* in the eigenfrequencies for most modes.

In Ref. [116], Raman active phonons with energy around 25 meV have been measured. Upon doping a shift is observed in the frequencies of the NdFeAsO system. Interestingly, however, the sign of the change is not constant among the various phonon

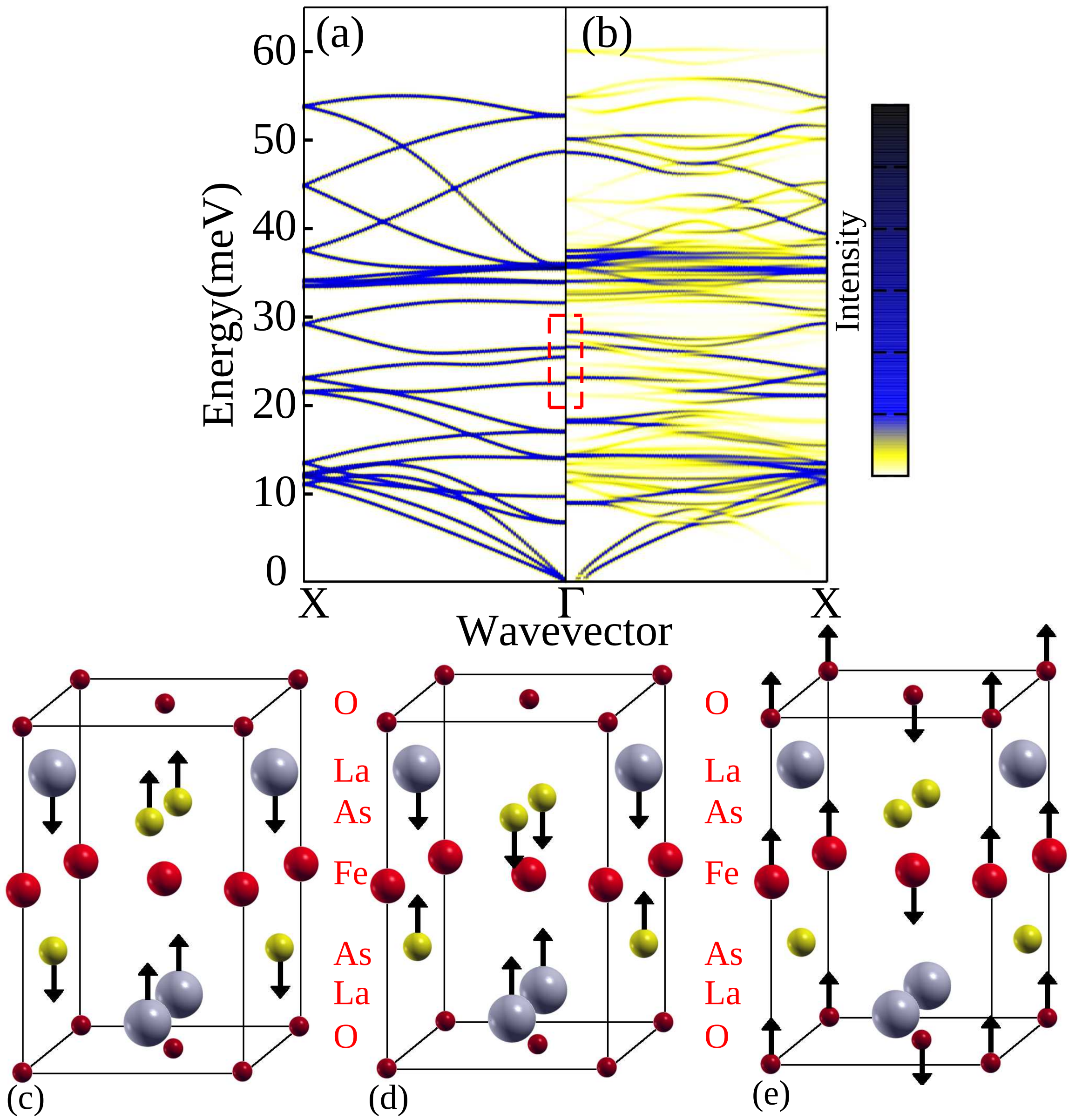

Figure 5.3: (Color online) Calculated phonon dispersions along the Δ direction of (a) pristine LaFeAsO and (b) F-doped LaFeAsO within the supercell model. The phonon dispersions of the supercell model have been obtained using the unfolding procedure corresponding to Eq. (5.1). (c), (d): Eigendisplacements of the A_{1g} (zone-center) phonons. (e): Eigendisplacements of the (zone-center) B_{1g} phonon. The red box highlights the eigenmodes (a)-(c) on the phonon dispersion.

$\mathbf{k}$	$\mathbf{q}$	$\omega_{\mathbf{q},\nu}$ (meV)	$\lvert g^{\nu}_{\mathbf{k},\mathbf{q}}\rvert$ (meV)
Γ	Γ	26.2	24.8
Γ	Γ	26.8	13.3
Γ	M	11.4	1.1
$0.4\overline{\Gamma M}$	Γ	40.3	2.8
$0.14\overline{\Gamma X}$	Γ	22.8	16.2

Table 5.1: Representative electron-phonon matrix elements of F-doped LaFeAsO, $|g^{\nu}_{\mathbf{k},\mathbf{q}}|$, involving the scattering of electrons near the Fermi surface which occupy the initial state with wavevector $\mathbf{k}$, by a phonon of wavevector $\mathbf{q}$ and branch index ν.

modes. This result indicates that the change in the phonon density of states does not originate from a uniform mass adjustment associated with the O:F replacement (a 19% change of the lightest mass in the crystal), and should rather be assigned the structural deformation as well as the peculiar rearrangement of the electronic charge.

We calculated a 1.0 meV *hardening* of the 25.2 meV A_{1g} phonon in LaFeAsO as well as a 1.6 meV hardening of the 26.3 meV B_{1g} phonon [(c) and (e) of Fig. [5.3]]. This finding compares favorably with the experimental increase of 0.6 meV of the two eigenfrequencies near 25 meV in NdFeAsO [116] observed through Raman spectroscopy. In the Raman scattering experiment the 22.1 meV A_{1g} [(d) of Fig. [5.3]] phonon is softened by 0.3 meV upon doping, while the detected peak is broadened by 25%. Our calculations show that the 22.2 meV A_{1g} phonon of LaFeAsO is actually split into two modes upon doping. Each mode contains contributions from the A_{1g} irreducible representation, although neither mode is of pure A_{1g} symmetry. The two resulting modes have energies of 21.0 meV and 22.8 meV. Taking into account the experimental broadening of 1.6 meV of the Raman signal, the two peaks would merge into a single signal which is 0.3 meV softer than in the pristine material, in accord with experiment.

Table 1 displays the results of some relevant electron-phonon matrix elements calculated for the doped system for phonons at the Γ, M and $X-$points in the Brillouin zone of doped LaFeAsO. These matrix elements are much smaller than what is observed in some electron-phonon superconductors with relatively high transition temperatures [38]. No phonon modes, associated with fluorine or otherwise, were found to generate significantly larger electron-phonon matrix elements. The total coupling strength in the doped system was found to be $\lambda = 0.18$, which is slightly smaller than what has been found in prior studies on the undoped material [115] where $\lambda = 0.21$. The slight decrease in the total electron-phonon coupling strength in the doped superconductor can primarily be ascribed to the lower electronic density of states at the Fermi level seen in $\mathrm{LaFeAsO}_{1-x}\mathrm{F}_x$.

We explained the difference in the lattice dynamics of doped LaFeAsO as compared to its undoped compound in terms of the structural relaxation of the atomic bonds around the dopants. Our calculations indicate that the description of the doping in this material in terms of electron-doping in the two-dimensional Fe-plane does not adequately reflect the physics of this system.

Chapter 6

Superconductivity in ultra-thin Pb layers

The possible existence of true two-dimensional superconductivity has been the subject of study for many decades [125, 126, 127, 128, 129]. Recent measurements have brought renewed interest to this field, as superconductivity has been confirmed in thin-film samples of lead down to a single monolayer [130, 131]. In ultra-thin Pb samples, the electronic wavefunctions are confined along the out-of-plane axis to a length scale of only a few nanometers. For Pb, which is free-electron-like in the bulk, significant modifications of the electronic states are expected to arise from quantum-size effects. In fact, many of these effects have been observed [132, 133, 134, 135, 136].

Past experimental work has suggested that the superconducting state in Pb films should not persist once the film thickness drops below a few monolayers [128], while the Mermin-Wagner theorem indicates that fluctuations should destroy a two-dimensional superconducting state at finite temperatures for any finite-ranged attractive interaction [137]. However, recent experiments demonstrating the presence of superconductivity in films of all thickness [130, 131] are an exciting contradiction to previous suggestions. Since Pb is the prototypical strong coupling electron-phonon superconductor with a myriad of wide-ranging studies in the literature, and now that it has been found to retain superconductivity in ultra-thin films, it creates an ideal system for studying quasi-two-dimensional superconductivity.

In this chapter we report the results of first-principles calculations on the electron-phonon coupling in bulk Pb as well as in films of thickness 2-6 monolayers. Electronic and phonon densities of states are given along with the Eliashberg spectral functions. We find that electron-phonon effects account for the experimental observations, and we propose a simple model which can account for the general trend of the superconducting transition temperature dependence upon film thickness. This study also suggests extensions for future calculations.

Our first-principles calculations are based on pseudopotential density-functional theory within the local density approximation (LDA) [29, 51] for free-standing Pb films. Our calculations utilize a plane-wave basis [121] with a kinetic energy cutoff of 80 Ry. This basis was employed in conjunction with a norm-conserving scalar-relativistic pseudopotential which included four valence electrons. A grid of $24 \times 24 \times 1$ electronic $\mathbf{k}$-vectors was used to describe the ground state electronic structure. We constructed models of Pb films along the (111) direction to mimic experimental observations. The unit cell was chosen with a simple 1×1 reconstruction in each monolayer. The experimental lattice parameter of bulk fcc Pb is 4.95 Å, while the relaxed LDA lattice constant was found to be 4.87 Å; this slight underestimate is consistent with the expected tendency of LDA to overbind. The fcc in-plane bond length, $a/\sqrt{2}$, was imposed by symmetry in the layered system to be 3.44 Å. The layer separation was relaxed so that each atom was subject to a force of less than 0.01 eV/Å. The calculations have been performed within a supercell arrangement [138], and the films have been separated by a vacuum layer of 15 Å which is sufficient to eliminate spurious interfilm interactions.

Lattice dynamics were determined using density functional perturbation theory [3] and the electron-phonon coupling was calculated using a Wannier-Fourier interpolation method [32, 33, 31]. A Brillouin zone mesh of 8×8×1 electronic wavevectors was used to find maximally localized Wannier functions for each thin-film system. Four *sp3*-like Wannier functions per Pb atom were used to describe accurately the electronic structure of each layered system. Phonons were calculated on a grid of 4×4×1 wavevectors. The electron-phonon matrix elements $g^{mn}_{\mathbf{kq}\nu}$, were determined at each point on this coarse grid. From the method described in Ref. [31], the electronic eigenvalues, phonon eigenfrequencies and electron-phonon matrix elements were determined on very fine-sampled Brillouin zone grids consisting of 250,000 unique electronic wavevectors and 2000 phonon wavevectors.

The superconducting transition temperature (T_c) and the total electron-phonon coupling strength λ were determined through isotropic Migdal-Eliashberg theory [53].

To begin we calculate the lattice dynamics, electron-phonon coupling strength λ, and Migdal-Eliashberg spectral function $\alpha^2 F$ for bulk fcc Pb to verify the method with the calculated pseudopotential as well as to give a basis for comparison of thin-film calculations. The total electron-phonon coupling strength was found to be $\lambda = 1.41$, where 10^6 electronic points and 5000 phonon wavevectors were used in the integration of Eq. [4.51] of Ref [8]. This value is consistent with many previously published results [62, 64, 65, 63]. Using the modified McMillan equation (Eq. 6.1) which is appropriate for strong-coupling superconductors [67], and a Coulomb repulsion parameter of $\mu^* = 0.14$, we find agreement between the measured and calculated superconducting transition temperature at 7.2 K.

$$T_c = \frac{f_1 f_2 \omega_{log}}{1.2} \exp\left(\frac{-1.04(1+\lambda)}{\lambda - \mu^* - 0.62\lambda\mu^*}\right) \tag{6.1}$$

Table 6.1 displays the densities of states (DOS) at the Fermi level for bulk and 2-6ML films based on our density functional theory calculations. We find that the Fermi level for the 3ML film lies in a peak in the DOS, arising from a quantum well state. This results in an unstable structure under lattice perturbations, yielding many soft phonon modes which drive the free-standing 3ML slab to a lower energy state not described by the 1×1 reconstruction. We believe this may contribute to the experimental difficulty in observing large islands of pristine 3ML Pb [130]. Similarly, within our calculations, the 4ML system is unstable to phonon eigenvectors which involve the asymmetric sliding of neighboring atomic sheets. It is worth noting that large pristine areas of 4ML Pb were not found in the experiments of Ref. [130]. Areas of 4ML were, however seen in close proximity

Structure	DOS (states/eV/spin/Pb)	DOS fraction of bulk	λ
bulk	0.482	1.00	1.41
2ML	0.322	0.67	1.05
3ML	0.707	1.47	—
4ML	0.467	0.97	—
5ML	0.447	0.93	1.37
6ML	0.488	1.01	1.38

Table 6.1: Calculated LDA electronic densities of states at the Fermi level $N(E_F)$ and electron-phonon couplings λ, for layered Pb at different film thicknesses in this work. The Fermi level of the 3ML film is at a peak in the DOS which tends to destabilize the free-standing film. Beyond this peak, the total DOS at the Fermi level per Pb atom does not varying largely in our calculation. Oscillations in $N(E_F)$ associated with quantum well states have been reported in studies which analyse much thicker films [140, 134]. The total electron-phonon coupling of the films approaches the bulk value as the film thickness is increased.

to 5ML islands. More recent work indicates that island size effects are of great importance to the superconducting properties of thin Pb films [135, 136, 132, 139]. In the case of our calculations for 4ML samples, it is possible that either a more complete treatment of bonding to the experimental substrate may stabilize the system or a method to take into account finite-sized films may yield physical results.

The LDA relaxed separation of each monolayer in the assorted films was analyzed. It was found, in agreement with prior studies [141], that the surface bonds of each system were contracted along the direction normal to the film. Excess surface electrons, from broken bonds arising from the terminiation of the Pb(111) layers, are concentrated in the interstitial regions of the slab. Increased bonding from these electrons was found to be the cause of the contraction along the out of plane direction. This results in an increased spring constant η, which leads to a stiffening of surface phonon modes.

The calculated phonon densities of states for bulk and 2ML Pb are shown in Figure 6.1. In the case of the 2ML film, the degeneracy of the transverse modes has been lifted by the presence of the surface which results in two distinct transverse peaks. Of particular interest is the stiffening of the longitudinal phonon peak by about 40%, or ∼3 meV. This stiffening is the result of a stronger Pb-Pb bond arising from the increased electron density in the surface bonds.

We have calculated the Eliashberg spectral function and total electron-phonon coupling for the stable freestanding Pb slabs of thickness 2, 5 and 6 monolayers. The spectral function in the 2ML system as well as in the bulk is displayed in Figure 6.2. The total electron-phonon coupling for each thickness is also given in Table 6.1. By inspecting the spectral function, which gives a total $\lambda = 1.05$ in the 2ML system, we see a reduction in the superconducting transition temperature T_c arising from reduced coupling to the longitudinal frequency phonons. A comparison of the coupling function $\alpha^2(\omega) = \alpha^2 F(\omega)/F(\omega)$, shows a

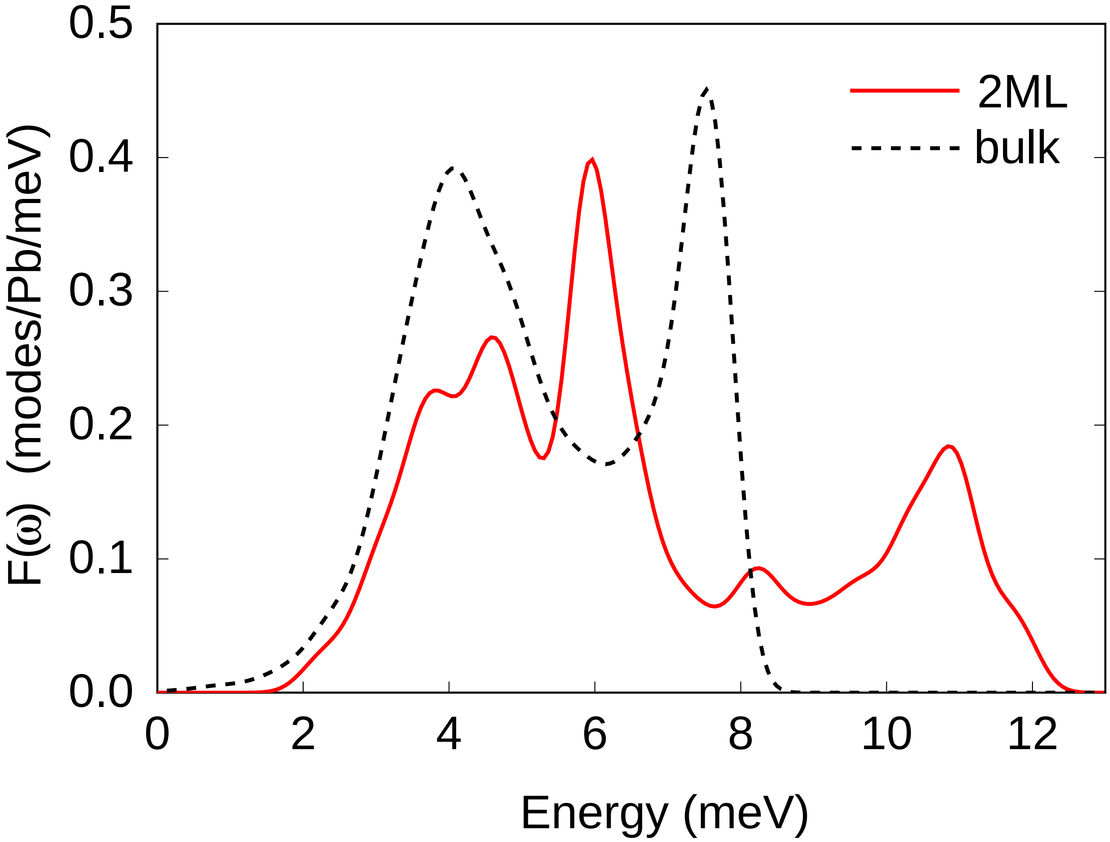

Figure 6.1: Phonon density of states for bulk Pb-fcc (dashed line) and 2ML Pb film (solid line). The transverse modes of the 2ML film are split and the out-of-plane TA peak is stiffened by 2 meV. The highest frequency LA peak is stiffened by 3 meV in the 2ML calculation as compared to the Pb-fcc data. For comparision, the curves are normalized such that $\int F(\omega) d\omega = 3$.

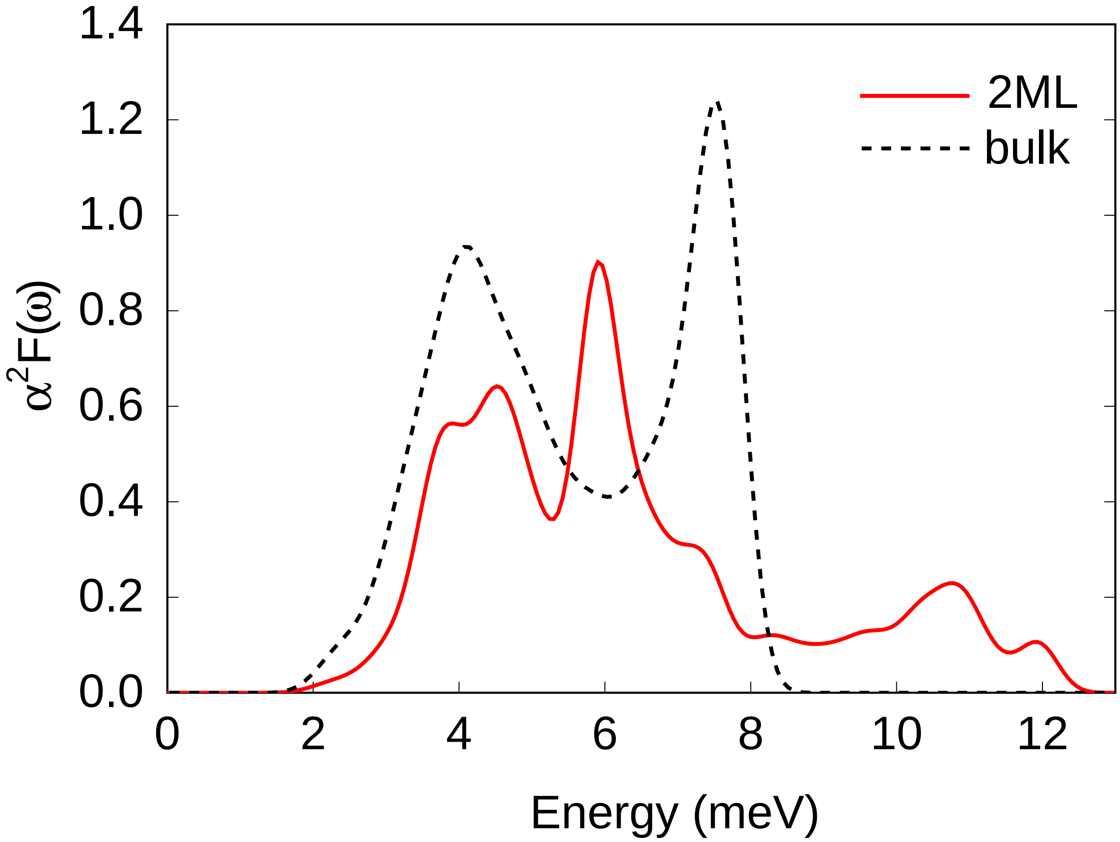

Figure 6.2: Eliashberg spectral function $\alpha^2 F$ for bulk Pb-fcc (dashed line) and 2ML Pb film (solid line). Here the total electron-phonon coupling $\lambda = 2\int \alpha^2 F(\omega)\omega^{-1}d\omega$ is decreased from the bulk value of 1.41 to the 2ML calculated value of 1.05. As can be seen from the above comparison of the spectral functions, the lower coupling in the 2ML system results from a depression of spectral weight which has also been shifted to higher frequencies.

smaller relative coupling to the longitudinal phonons in the thin layered sample. The main conclusion which can be drawn from these data is that the surface phonon modes, which are at an increased frequency, contribute less to the total coupling than the corresponding bulk phonons modes.

We next propose a simple model to account for the observed superconducting transition temperatures over a wide range of Pb film thicknesses. As seen in Ref. [142], the T_c is observed to follow a $1/d$ law, where d is the film thickness. In a bulk system, the layer separation is $a/\sqrt{3} \sim 2.86$ Å. If the system is taken to be composed of isolated regions of bulk superconductivity and surface superconductivity, we can assign a specific electron-phonon coupling to each region. As we have calculated a nearly pure surface-like system with the free-standing 2ML slab, we take the surface coupling strength $\lambda_{\mathrm{surf}} = 1.05$. The bulk coupling is then $\lambda_{\mathrm{bulk}} = 1.41$. In the experimental system, the measured Pb(111) films have been deposited on Si [143]. The effect of the substrate upon the electron-phonon

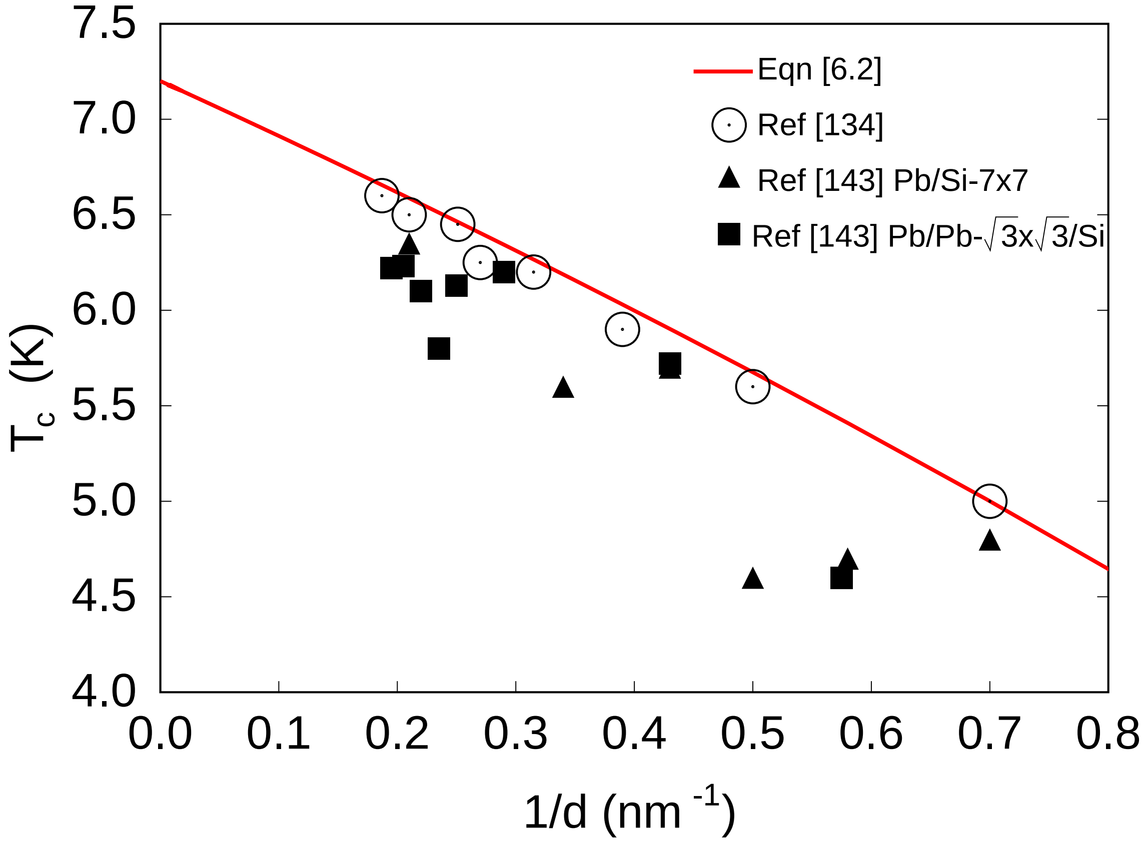

Figure 6.3: Superconducting transition temperature as a function of layer thickness for the experimental points of Ref. [133, 142] and the theoretical model (Eq. 6.2). The transition temperature was calculated through the modified McMillan equation (Eq. (34) of Ref. [67]). Frequency moments have been fixed for differing λ's and the Coulomb repulsion parameter is taken to be $\mu^* = 0.14$, to obtain the experimental bulk $T_c = 7.2$ K.

coupling has not been examined in detail in this work, however we can posit with some justification that the substrate-Pb coupling constant λ_{sub} is fixed for increasingly thick films. The total electron-phonon coupling strength as a function of film width $\lambda(d)$ can be approximated by

$$\lambda(d) = \frac{L}{d}\left[\left(\frac{d}{L} - 2\right)\lambda_{\text{bulk}} + \lambda_{\text{surf}} + \lambda_{\text{sub}}\right]. \tag{6.2}$$

Here L is the layer thickness which in the bulk is 2.86Å along the (111) direction. We fix λ_{sub} so that we obtain the recently measured T_c of the monolayer, 1.83 K [131], assuming the monolayer electron-phonon coupling is the average of the surface coupling and the substrate coupling. We use Eq. 6.2 to calculate the electron-phonon coupling and Eq. 6.1 to estimate the superconducting transition temperature as a function of layer thickness. The resulting trend of T_c with film thickness agrees very well with the experimental data, as shown in Figure 6.3. Although this model does not take into account many of the finer details of very thin metallic films, however it does provide a straightforward interpretation of the gross experimental features.

The above arguments do not account for the details of quantum-size effects which arise from the confined electronic quantum well states. It may be possible for example, through the stabilization of a film which produces a peak in the electronic DOS, to overcome the apparent suppression of T_c by the surface phonons. If for example, the 3ML film could be structurally stabilized while retaining its increased electronic DOS, a scaling of $\lambda = 1.6$ may be expected. This would lead to a superconducting transition temperature of $\sim$10 K which is well above the bulk value of 7.2 K. Further studies of the effects of the Pb-Si interface on the electron-phonon interaction is needed [143]. These studies may give us insight about the possibile stability of films which exist near quantum well states and on how the complex interplay between surface physics, lattice dynamics and quantum confinement affect superconductivity in these ultra-thin systems.

We find that the observed superconductivity in thin film samples of Pb is explained through the use of isotropic Migdal-Eliashberg theory. We find, in agreement with experiment, that the total electron-phonon coupling decreases with decreasing film thickness. The variance of the superconducting transition temperature with film thickness can be explained with a simple model relating the surface and bulk electron-phonon coupling. Additional studies which carefully examine the interaction of the metal-substrate interface could yield clues to routes of increased superconducting transition temperature in increasingly thin systems.

Chapter 7

Monolayer superconductivity of Pb on Si(111)

As a superconducting material is made thinner and thinner, eventually the system becomes two dimensional and is expected to lose its superconducting properties. The predicted loss of superconductivity in two-dimensional films is based upon on the assumption of a Kosterlitz-Thouless (KT) [144] phase transition which strictly prohibits the long range ordering necessary to sustain the superconducting phase. As a result of this interesting physical phenomenon, the study and discussion of potential 2D superconductivity has been a focus of intense research activity for many years [125, 126, 127, 128, 145]. While technological advances have permitted the fabrication of increasingly thin metallic films, it is only recently that a single monolayer of superconducting material has been measured at low temperatures.

Lead, the prototypical strong coupling electron-phonon superconductor, has a superconducting transition temperature of 7.2 K in the bulk and a ratio of superconducting gap to transition temperature of $2\Delta/k_BT_c = 4.3$, well above the BCS prediction of 3.52. Through recent scanning tunneling spectroscopy (STS) experiments, Pb has been shown to superconduct in samples comprised of only a single layer of atoms. This result, described as two-dimensional superconductivity, contrasts the predictions of the Mermin-Wagner theorem [146] which prohibits spontaneous symmetry breaking in systems of dimensions $d \leq 2$.

The recent experiments measuring the superconducting gap in thin films have observed superconductivity in monolayer samples of both Pb and In on Si [131]. Because a stable free-standing monolayer Pb or In film is unstable, the monolayers were deposited on a semiconducting substrate. Therefore, a thorough grasp of the metal-substrate interaction is highly important in understanding these experiments as well as for development and prediction of potential new thin superconductors. Given the robust superconductivity which has been previously reported in increasingly thin crystalline Pb films, it may soon be possible to fabricate many novel and technologically beneficial devices once a working knowledge of the underlying physics is attained.

In this letter we describe calculations on the ground state properties of a single layer of Pb grown on a Si(111) substrate in the configuration depicted by Fig. 7.1. The electronic structure, lattice dynamics and superconductivity are calculated for this structure, the thinnest Pb superconductor. Commentary on the implications of two-dimensional superconductivity is presented, and discussions of the structure as well as suggestions for routes to increased superconducting transition temperatures for thin films are given.

Within Ginzberg-Landau theory, the superconducting state is described by a spatially resolved complex order parameter, $\Psi(r)$. This order parameter possesses long-range correlations which can be quantified through the correlation function $\langle\Psi(r)\Psi(0)\rangle$ as $r \rightarrow \infty$. While this function has a finite value in the superconducting state, it vanishes as the temperature of the system is raised above T_c. However, the same analysis of the real space correlation function of a superconductor in two dimensions yields different results. In this case, it does not approach a constant value for large r as it does in a bulk superconductor. For systems below the KT transition temperature, T_{KT}, the correlation function decays slowly over large distances as in Eq. (7.1).

$$\langle e^{i(\phi(r)-\phi(0))}\rangle \sim \frac{1}{r^{2T/T_{KT}}} \tag{7.1}$$

The correlation function tends to zero as $r \rightarrow \infty$. The function shown in Eq. (1) only includes the complex phase-dependence of the order parameters as the magnitudes do not possess interesting spatial features. The absence of a positive correlation over long distances in two dimensions indicates the lack of true long range order. Because of this lack of long-range correlation, local fluctuations destroy the superconducting state, and therefore a two-dimensional metallic system cannot exhibit superconductivity. How, then, is the above argument to be rectified with recent experimental observations?

To analyze the full superconductor-substrate system, we performed state of the art pseudopotential-first-principles density functional theory calculations. Within the local density approximation (LDA) to density functional theory (DFT), we employed norm-conserving pseudopotentials to account for the core-valence interaction and included scalar-relativistic corrections to the Pb pseudopotential [29, 51]. While the spin-orbit coupling has been seen to have an impact on the total electron-phonon coupling [147], these results to not heavily impact the conclusions of this work. A plane-wave basis with a kinetic energy cutoff of 45 Ry was used to construct the Kohn-Sham eigenfunctions on a momentum-space grid of 12x12x1 wavevectors [28]. The quantum well states (QWS), which have been the subject of previous work are naturally included in our formalism [129]. Lattice dynamics were constructed through density functional perturbation theory (DFPT) [3]. The atoms of the substrate were held fixed, while the linear-response dynamical matrix was constructed for the 4 lead atoms per unit cell. This calculational constraint was necessary as proper treatment of the bulk and surface Si vibrational modes would require prohibitively thick slabs of silicon, generating extremely cumbersome unit cells in order to treat the surface Si modes.

The total electron-phonon coupling strength λ was determined through isotropic Migdal-Eliashberg theory, while the superconducting transition temperature was estimated using the Allen-Dynes equation [Eq.(7.2)] [67]. The Allen-Dynes equation is used to obtain a satisfactory estimate of the superconducting transition temperature in this system for ease of comparison with experiment [20]. Here, the Coulomb pseudopotential has been taken to be $\mu^* = 0.14$, a number which is in agreement with many previous studies [148, 149] on bulk Pb. This estimate, which depends on the validity of the aforementioned formalism in a quasi-two-dimensional system, is primarily provided as a reference to experiment while the primary result of this study is the total electron-phonon coupling λ.

$$T_c = \frac{\omega_{log}}{1.2}\exp\left(\frac{-1.04(1+\lambda)}{\lambda - \mu^* - 0.62\lambda\mu^*}\right) \tag{7.2}$$

A state of the art Wannier-Fourier interpolation technique has been utilized in the computation of electron-phonon related quantities [32, 33, 31]. The resulting dense sampling of the electronic eigenvalues, phonon frequencies, and electron-phonon matrix elements was obtained through use of the `Quantum ESPRESSO` [30], `wannier90` [47] and `EPW` [150] codes.

Coarse grids of 16 electronic and phonon wavevectors were interpolated to fine meshes containing 3600 phonon wavevectors and 10000 electronic states. Each electron-phonon matrix element $g^{ij\nu}_{\mathbf{k},\mathbf{q}}$ between an electronic state at $\mathbf{k}$, scattered by phonon $\mathbf{q}$ to state $\mathbf{k}+\mathbf{q}$ has indices i, j, and ν which run over 12 phonon modes and 55 Wannier functions. The matrix elements, averaged over wavevectors on the Fermi surface, combine to give the total electron coupling strength, λ using Eq. (7.3) [8].

$$\lambda = \frac{1}{N_k N_q}\sum_{\mathbf{kq}ij\nu}\frac{2}{\omega_{\nu\mathbf{q}}N(0)}\left|g^{ij\nu}_{\mathbf{k},\mathbf{q}}\right|^2\delta(\epsilon_{i\mathbf{k}})\delta(\epsilon_{j\mathbf{k}+\mathbf{q}}) \tag{7.3}$$

Here $\omega_{\nu\mathbf{q}}$ are the phonon eigenfrequencies, $\epsilon_{i\mathbf{k}}$ are the electronic eigenvalues, and N(0) is the electronic density of states at the Fermi level. The number of electronic and phonon wavevectors is given by N_k and N_q, respectively.

The crystal has been constructed in our calculations as follows. A unit cell containing 25 atoms forms a slab wherein a single layer of Pb atoms is placed above 3 bilayers of bulk Si. As a consequence of the finite out-of-plane-axis thickness of the silicon layer, the dangling bonds opposite the Pb overlayer have been passivated by attaching hydrogen atoms to the remaining unbonded *sp*3 Si states. The Pb-Si-H slabs have been constructed in a supercell arrangement, each slab separated by a vacuum layer of 22 Å which is sufficient to eliminate spurious interfilm interactions [138].

Using our scalar-relativistic LDA pseudopotential, the bulk relaxed LDA lattice constant of fcc Pb was found to be 4.87 Å, which compares favorably to the experimental lattice constant of 4.95 Å. Using the relaxed lattice constant we find that the (111) in-plane bond length is 3.44 Å for Pb in the 1×1 crystal arrangement as described in Ref. [66]. To correctly reconstruct the interface between bulk Si and monolayer Pb, we use a unit cell containing 3 Si atoms per layer capped by 4 Pb atoms forming a so-called striped incommensurate phase (SIC-Pb) of monolayer Pb [151]. This incommensurate phase, an arrangement only possible within a unit cell containing at least 4 Pb atoms, breaks the symmetry of the Pb-Pb bonds in such a way as to create two interatomic Pb lengths. Here we find that the shorter of the two, denoted by a bond in Fig. 7.1, is 3.00 Å. The longer of the two distances is 3.66 Å, 6% longer than the bulk value of 3.44 Å.

Below the Pb layer, the bulk substrate is modeled by three bilayers of Si in order to accurately describe the electronic structure at the interface. Specifically we are interested in hybridization effects which bear on the interatomic electronic densities and therefore the effective spring constants of the Pb-Pb and Pb-Si bonds. The in-plane unit cell has been constructed such that the bulk lattice constant of Si in this configuration takes on the relaxed

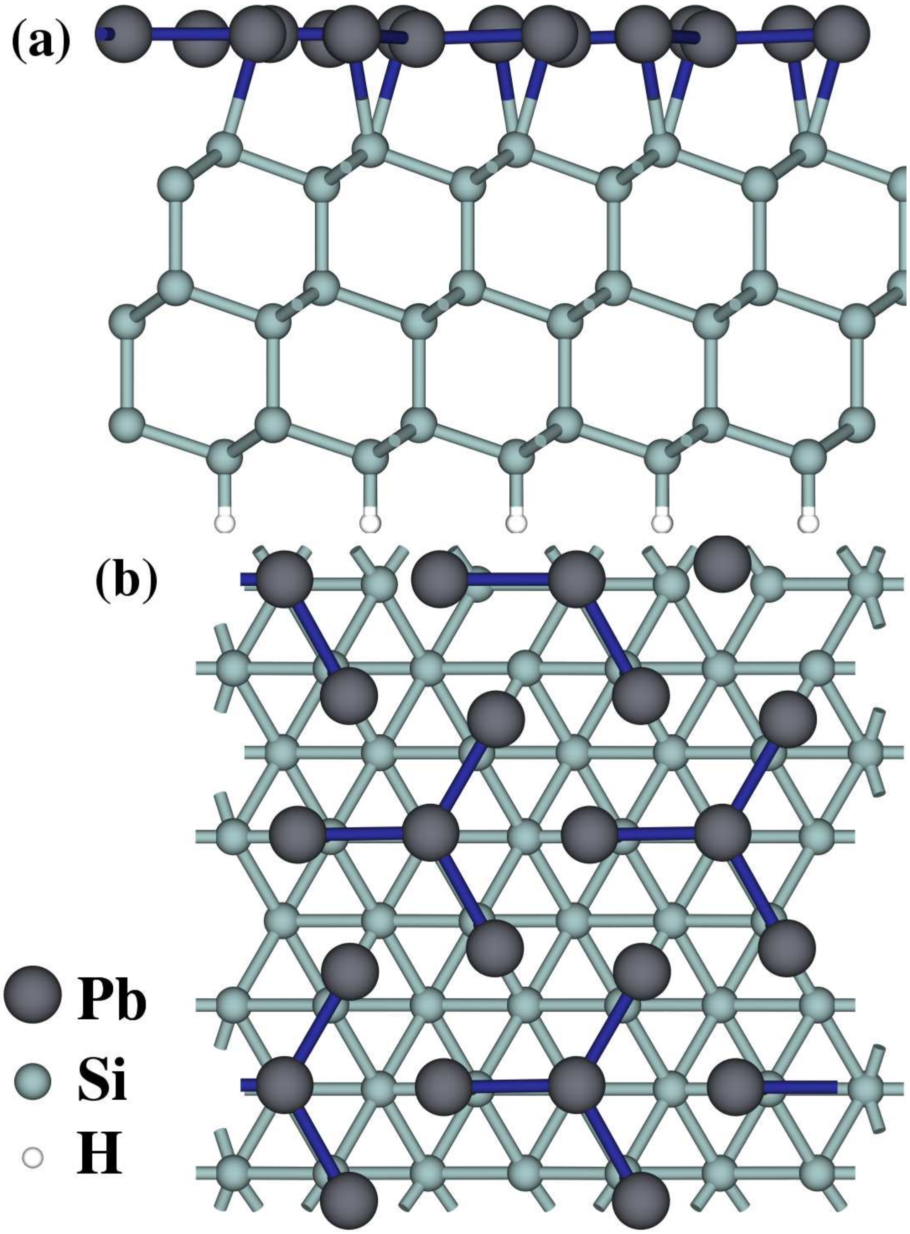

Figure 7.1: (Color online) Side view (a) and top view (b) projections of a few unit cells of the crystal structure employed in the calculations of this letter. Pb has been deposited on three bilayers of Si. The reconstruction of the Pb monolayer arising from the Si surface results in differentiated Pb-Pb bond lengths. The shorter Pb-Pb bonds are depicted most clearly by the dark lines in (b). This is the striped incommensurate phase (SIC-Pb) of monolayer Pb on Si(111) which has been shown to be superconducting in Ref. [131].

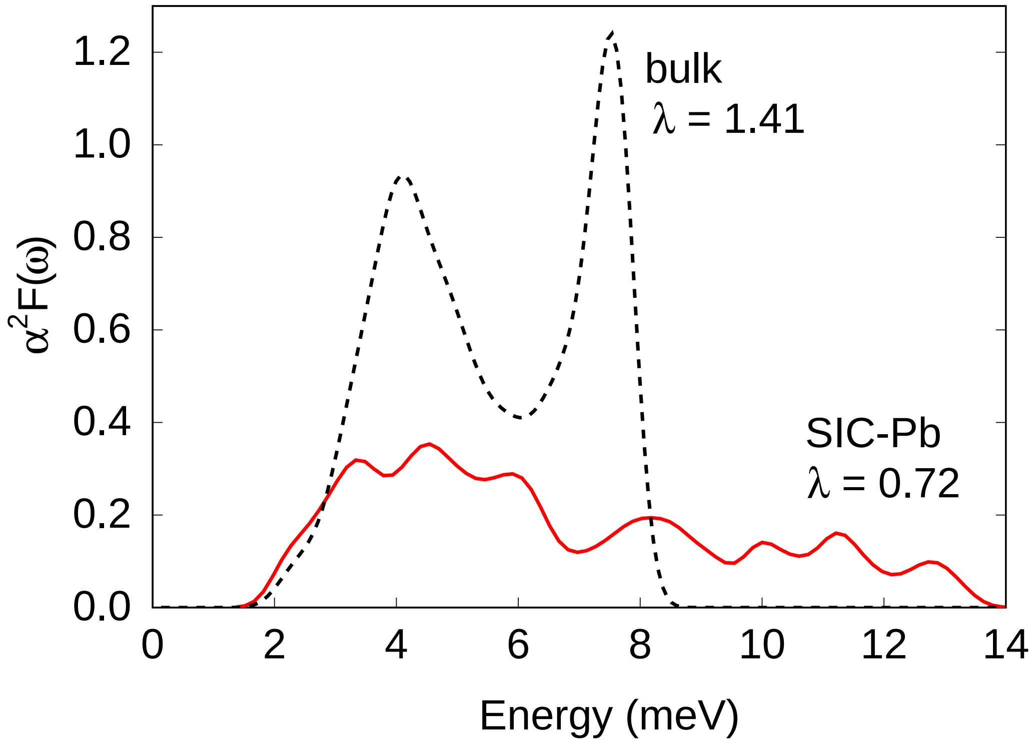

Figure 7.2: (Color online) Eliashberg spectral function α^2F for bulk Pb-fcc (dashed line) and monolayer SIC-Pb film on Si(111) (solid line). The total electron-phonon coupling $\lambda = 2\int \alpha^2F(\omega)\omega^{-1}d\omega$ is decreased from the bulk value of 1.41 to the monolayer calculated value of 0.72. The decrease arises primarily from stiffened phonon modes and a suppression of low-energy spectral weight coming from weaker electron-phonon matrix elements. The estimated T_c of 1.5 K arising from the monolayer spectral function is in very good agreement with the experimental value of 1.83 K.

value of 5.39 Å, as compared to the experimental value of 5.43 Å. The system has been fully relaxed such that the forces present are less than 0.02 $eV/Å$. Our configuration does not allow for reconstruction of the Si surface, however we do find that the Pb monolayer is put under a compressive strain by the bonding to the Si surface. This leads to some out-of-plane structure. Of each four atom unit cell, three Pb atoms are covalently bonded to the Si surface while the final atom is only bonded metallically to its Pb neighbors. The unbounded Pb atom sits 0.11 Å above the plane created by the bonded Pb atoms which form a 2.73 Å covalent bond to the top layer of Si atoms. This lattice-mismatch, which breaks many of the symmetries present in a simple 1×1 Pb monolayer construction leads to a great deal of structure in the phonon density of states.

The 2D features of the Pb surface, namely the differentiated bond lengths, are an artifact of the lattice mismatch between the Si and Pb. This mismatch imposes a strain on the Pb sheet. That strain causes a compression of the nearest neighbor Pb-Pb bonds and is present because of the energetically favorable bonding to the top layer Si atoms [152], resulting in strongly stiffened phonon frequencies. Related to this phenomenon, it has long been shown that Pb exhibits a monotonic decrease in superconducting transition temperature as a function of pressure [153, 154], directly correlated to increased phonon frequencies. In addition to a suppressed T_c, the ratio of the superconducting gap to the transition temperature, $2\Delta/k_BT_c$ in Pb under pressure has been found to be closer to the BCS value of 3.52 [155]. This effect has been attributed to a weakened electron-phonon coupling [156], an assertion which is supported by this letter.

We have calculated the total electron-phonon coupling in monolayer Pb on Si through Eq.(7.3) and find $\lambda = 0.72$. The Eliashberg spectral function for bulk Pb [66] and the monolayer calculation of this work are presented in Fig. 7.2. Using the logarithmically averaged phonon frequency $\omega_{log} = 4.9$ meV and $\mu^* = 0.14$, we estimate a superconducting transition temperature $T_c = 1.5$ K. This estimate depends weakly on the use of the bulk value of the Coulomb repulsion in the quasi-two-dimensional state. Variation of μ^* between reasonable values of 0.1 and 0.2 leads to a stable T_c of 1.5 ± 0.6 K. This estimate is in extremely good agreement with the experimental value of 1.83 K [131]. The decrease in total electron phonon coupling in SIC-Pb as compared to the calculated bulk value of $\lambda = 1.41$ [66] can be attributed to the stiffening of the phonon frequencies $\omega_{\nu\mathbf{q}}$ arising from bonding to the Si surface as well as a decrease in the magnitude of the electron-phonon matrix elements $g^{ij\nu}_{\mathbf{k},\mathbf{q}}$. The matrix elements are affected primarily because the $6p$ Pb wavefunctions at the Fermi level have hybridized with the silicon surface. This hybridization brings silicon states which are described very well using $sp3$-like Wannier functions into the matrix element integrals. As has been measured as well as calculated, the total electron-phonon coupling strength in hole-doped Si is significantly lower than in Pb [104]. Inspection of the Eliashberg spectral function of bulk hole-doped Si in Ref. [104] indicates that the electron-phonon matrix elements coupling phonons of frequencies below 50 meV are vanishingly small. It is therefore not surprising that introducing similar wavefunctions into the electron-phonon matrix elements of states near E_f would suppress the term $|g^{ij\nu}_{\mathbf{k},\mathbf{q}}|^2$ of Eq. (7.3). Interestingly, we find an increase in the electronic density of states at the Fermi level in SIC-Pb. Our calculated value of 0.583 states per eV per Pb atom is a 21% increase over bulk value of 0.482 states per eV per Pb atom [66]. This increase balances out some of the decrease in λ coming from increased phonon frequencies and weaker matrix elements.

Previously, semi-empirical formulas to describe the electron-phonon coupling in thin Pb films as a function of thickness have been presented [66]. Detailed in Eq. (7.4), the five parameters which enter into the total coupling estimation are λ_{bulk}, λ_{surf}, λ_{sub}, d and L. The bulk and surface interaction terms have been calculated from first-principles to be 1.41 and 1.05 respectively. The factor λ_{sub}, which accounts for the Pb interaction with a substrate had been fitted to match estimated superconducting transition temperatures with experimentally measured values. Of final two parameters, L is the thickness of a single layer. This is taken as the lattice constant of Pb divided by the geometrical factor $\sqrt{3}$, while d is the thickness of the sample in question. Using a simple model where the monolayer of Pb on Si behaves as if it is the average of a surface layer and a substrate layer, we find using previous first-principles results that $\lambda_{sub} = 0.39$. This value compares well to the fitted value of 0.30 used in Ref. [66], indicating self-consistency of these two approaches.

$$\lambda(d) = \frac{L}{d}\left[\left(\frac{d}{L} - 2\right)\lambda_{\text{bulk}} + \lambda_{\text{surf}} + \lambda_{\text{sub}}\right] \tag{7.4}$$

Evidenced by the strong effect on the Eliashberg spectral function [Fig.7.2], it is clear that the Pb-substrate interaction is of central importance to the behavior of this system. Therefore, the experimentally observed superconductivity in monolayer Pb is heavily dependent upon the Si(111) surface. This interaction provides a simple resolution to the competition between reduced dimensions and superconductivity; the Pb-Si system is not truly two-dimensional and therefore the observation of superconductivity in monolayer Pb does not violate the Mermin-Wagner theorem. This conclusion is supported by the ARPES observation of two distinguished two-dimensional single-electron subbands [131]. Unlike a freestanding monolayer of Pb, these bands, present in our calculated electronic bandstructure (not shown), indicate that the electrons in this system are not strictly two-dimensional. This system can therefore be more accurately described as quasi-two-dimensional.

Strong theoretical support for BCS electron-phonon superconductivity in monolayer films of Pb as measured by scanning tunneling spectroscopy experiments has been presented. While this system is at the atomic limit of film deposition, superconductivity is benefited by the interaction with the silicon substrate. The interaction of metal with substrate prevents this system from undergoing a KT phase transition, allowing for the long range phase coherence necessary to sustain a superconducting state. It is clear that the observed superconductivity in Pb cannot be separated from the effects of the substrate and therefore the complex Pb-Si system must be treated as a whole. Additionally, the superconducting transition temperature of ultra-thin Pb may be enhanced by reducing the in-plane strain on the metallic Pb-Pb bonds, which would soften the phonons involved in superconductivity. Additional work to model the Si surface vibrations may be interesting to further clarify the role of the substrate in this and other novel thin superconductors.

Chapter 8

Phonon-assisted absorption in silicon from first-principles

The phonon-assisted absorption of light in materials is an important optical process both from a fundamental and from a technological point of view. Intraband light absorption by free carriers in metals and doped semiconductors requires the additional momentum provided by the lattice vibrations, while phonon-assisted processes determine the onset of absorption in indirect-band-gap semiconductors (Fig. 8.1). Moreover, the value of the direct band gap in silicon (3.4 eV[157]) is large and precludes optical absorption in the visible. However, silicon is a commercially successful photovoltaic material because of the indirect optical transitions that enable photon capture in the spectral region between the indirect (1.1 eV[158]) and direct band gaps.

Despite their importance, at present only a very limited number of first-principles studies of phonon-assisted optical absorption spectra exist. *Ab initio* calculations of direct optical absorption spectra including excitonic effects have already been performed for Si and other bulk semiconductors [159, 160, 161] and the underlying methodology is presently well established [162, 163]. Phonon-assisted absorption studies are more involved, however, and the associated computational cost is much higher than the direct case. The calculation of the indirect absorption coefficient involves a double sum over $\boldsymbol{k}$-points in the first Brillouin zone (BZ) to account for all initial and final electron states. In addition, these sums must be performed with a very fine sampling of the zone to get an adequate spectral resolution. The computational cost associated with these BZ sums is in fact prohibitive with the usual methods. Phonon-assisted absorption calculations have been done for the special case of free-carrier absorption[55], where the carriers are initially limited to a region near the Γ point of the first BZ, but a full calculation using brute-force methods for the general case remains beyond the reach of modern computers.

The difficulty of zone-integral convergence can be addressed with the maximally-localized Wannier function interpolation method[32, 33, 47]. Using this technique, the quasiparticle energies[164] and optical transition matrix elements[34, 36] can be interpolated to arbitrary points in the BZ at a minimal computational cost. Moreover, this interpolation method has been generalized[31, 39] to obtain the electron-phonon coupling matrix elements between arbitrary pairs of points in the first BZ.

In this Letter, we developed a first-principles computational method, based on a Wannier-Fourier interpolation formalism, to determine the phonon-assisted optical absorption spectrum of silicon from first principles. The calculated data near the absorption onset are in very good agreement with experimental results for a range of temperatures. Moreover, we were able to reproduce the absorption spectrum of silicon in the energy range between the indirect and direct band gaps (1.1 – 3.4 eV), a spectral region that cannot be accessed by standard model calculations. This region covers the entire visible spectrum and is important for optoelectronic applications.

To calculate the phonon-assisted absorption coefficient in silicon, we start by using the Fermi's golden rule expression and obtain[165, 55]:

$$\begin{aligned}\alpha(\omega) =& 2\frac{4\pi^2 e^2}{\omega c n_r(\omega)}\frac{1}{V_{\text{cell}}}\frac{1}{N_{\boldsymbol{k}}N_{\boldsymbol{q}}}\sum_{\nu ij\boldsymbol{k}\boldsymbol{q}}|\boldsymbol{\lambda}\cdot(\boldsymbol{S}_1+\boldsymbol{S}_2)|^2\\ &\times P\delta(\epsilon_{j,\boldsymbol{k}+\boldsymbol{q}}-\epsilon_{i\boldsymbol{k}}-\hbar\omega\pm\hbar\omega_{\nu\boldsymbol{q}}),\end{aligned} \tag{8.1}$$

where $\hbar\omega$ and $\boldsymbol{\lambda}$ are the energy and polarization of the photon and $n_r(\omega)$ is the refractive index of the material at frequency ω. The generalized optical matrix elements, $\boldsymbol{S}_1$ and $\boldsymbol{S}_2$, are given by

$$\boldsymbol{S}_1(\boldsymbol{k},\boldsymbol{q}) = \sum_m \frac{\boldsymbol{v}_{im}(\boldsymbol{k})g^{\text{SE}}_{mj,\nu}(\boldsymbol{k},\boldsymbol{q})}{\epsilon_{m\boldsymbol{k}}-\epsilon_{i\boldsymbol{k}}-\hbar\omega+i\Gamma_{m,\boldsymbol{k}}}, \tag{8.2}$$

$$\boldsymbol{S}_2(\boldsymbol{k},\boldsymbol{q}) = \sum_m \frac{g^{\text{SE}}_{im,\nu}(\boldsymbol{k},\boldsymbol{q})\boldsymbol{v}_{mj}(\boldsymbol{k}+\boldsymbol{q})}{\epsilon_{m,\boldsymbol{k}+\boldsymbol{q}}-\epsilon_{i\boldsymbol{k}}\pm\hbar\omega_{\nu\boldsymbol{q}}+i\Gamma_{m,\boldsymbol{k}+\boldsymbol{q}}}, \tag{8.3}$$

and correspond to the two possible paths of the indirect absorption process (Fig. 8.1). They are determined in terms of the velocity ($\boldsymbol{v}$) and electron-phonon coupling (g) matrix elements, as well as the real ($\epsilon_{n\boldsymbol{k}}$) and imaginary ($\Gamma_{n\boldsymbol{k}}$) parts of the quasiparticle self-energies. The factor P accounts for the carrier and phonon statistics,

$$P = \left(n_{\nu\boldsymbol{q}}+\frac{1}{2}\pm\frac{1}{2}\right)(f_{i\boldsymbol{k}}-f_{j,\boldsymbol{k}+\boldsymbol{q}}).$$

The upper (lower) sign corresponds to phonon emission (absorption).

First-principles calculations were performed within the local density approximation (LDA)[29, 51] to density functional theory using a plane-wave pseudopotential approach[28] with a kinetic energy cutoff of 35 Ry. The ground state charge density was determined on a BZ grid of 14×14×14 $\boldsymbol{k}$-points. Quasiparticle energies within the GW approximation for the self-energy operator[166, 167, 168] were determined on a 6×6×6 grid and interpolated throughout the BZ through the use of the maximally-localized Wannier function formalism[32, 33, 47]. We included 34 electronic bands in the coarse-grid calculation and extracted 26 Wannier functions, which reproduce the LDA bandstructure 10 eV below and 30 eV above the Fermi level. The interpolated quasiparticle band structure of silicon is shown in Figure 8.1. The indirect (1.3 eV) and direct (3.3 eV) quasiparticle band gaps are in good agreement with previous calculations[167] and experiment. The same formalism has been used to interpolate the velocity matrix elements[162, 34, 36], including the renormalization required [169] after the GW corrections. The real (ε_1) and imaginary (ε_2) parts of the dielectric function and the refractive index due to direct transitions were also determined at the quasiparticle level for a range of photon frequencies (Fig. 8.2), required in Eq. 8.1 to determine the absorption coefficient. Lattice dynamics are calculated using density functional perturbation theory[3]. The electron-phonon coupling matrix elements are calculated on the same coarse grid of electronic points, while the dynamical matrices and phonon-potential perturbations are calculated on a 6×6×6 grid of momentum-space vectors[31, 39] using the EPW code[150]. The imaginary part of the electron self energies ($\Gamma_{n\boldsymbol{k}}$) arising from the electron-phonon interaction[31, 39, 150] are calculated for a large number of quasiparticle states (Fig. 8.3).

Phonon-assisted optical absorption in indirect-band-gap semiconductors occurs for photons with energies greater than the indirect band gap minus (plus) the energy of the phonon absorbed (emitted) to assist the transition. The onset of indirect absorption is calculated over a wide range of temperatures in bulk silicon through Eq. 8.1 and the results are shown in Fig. 8.4. The theoretical data have been shifted horizontally by 0.15 − 0.23 eV to match the experimental absorption onset. Each curve displays a characteristic knee, arising from the different energy onsets of the phonon-absorption and phonon-emission terms, which becomes smoother with increasing temperature. The calculated data are in good agreement with experimental results[170] for all temperatures measured. For these calculations, we used fine grids of 40×40×40 for the $\boldsymbol{k}$ and $\boldsymbol{q}$ sums in Eq. 8.1, respectively. These fine grids yield converged optical spectra with an energy resolution of 14 meV, which is quite small and necessary to resolve the fine features near the absorption onset. Although the experimental data near the edge can be fit with simple parameterized forms[170], to our knowledge they have not been calculated entirely from first principles previously.

In addition to the absorption onset, we are interested in the phonon-assisted absorption spectrum in the energy range between the indirect and direct band gaps, covering the visible range. This spectral region involves transitions between valence and conduction band states away from the band extrema and, as a consequence, cannot be modeled with simple parameterized forms. On the contrary, because of the large number of electronic states and phonon modes involved, first-principles calculations are the only computational tool that can access this spectral region. The interpolation of the *ab initio* quantities within the Wannier-Fourier formalism makes the calculation feasible on modern computers. The calculated spectra with an energy resolution of 30 meV (Fig. 8.5) converge with zone-sums of 24×24×24 electronic and 24×24×24 phonon points. The imaginary part of the electron self-energy for the intermediate electronic states was set to a constant value (100 meV). However, the calculated data are not very sensitive to the particular value of the quasiparticle lifetime for photon energies in this spectral region.

In order to improve the agreement between theory and experiment, the theoretical absorption spectra of Figs. 8.4 and 8.5 have been shifted to the left along the energy axis by 0.15-0.23 eV. The reason for these shifts has to do with the accuracy of the calculated quasiparticle energies, as well as with finite temperature effects. First, the quasiparticle energies as calculated with the GW approximation are typically accurate to within 0.1 eV from experiment. In our particular case, we also found that the calculated band gap is within this error bar larger than the experimentally measured one. We note that no other

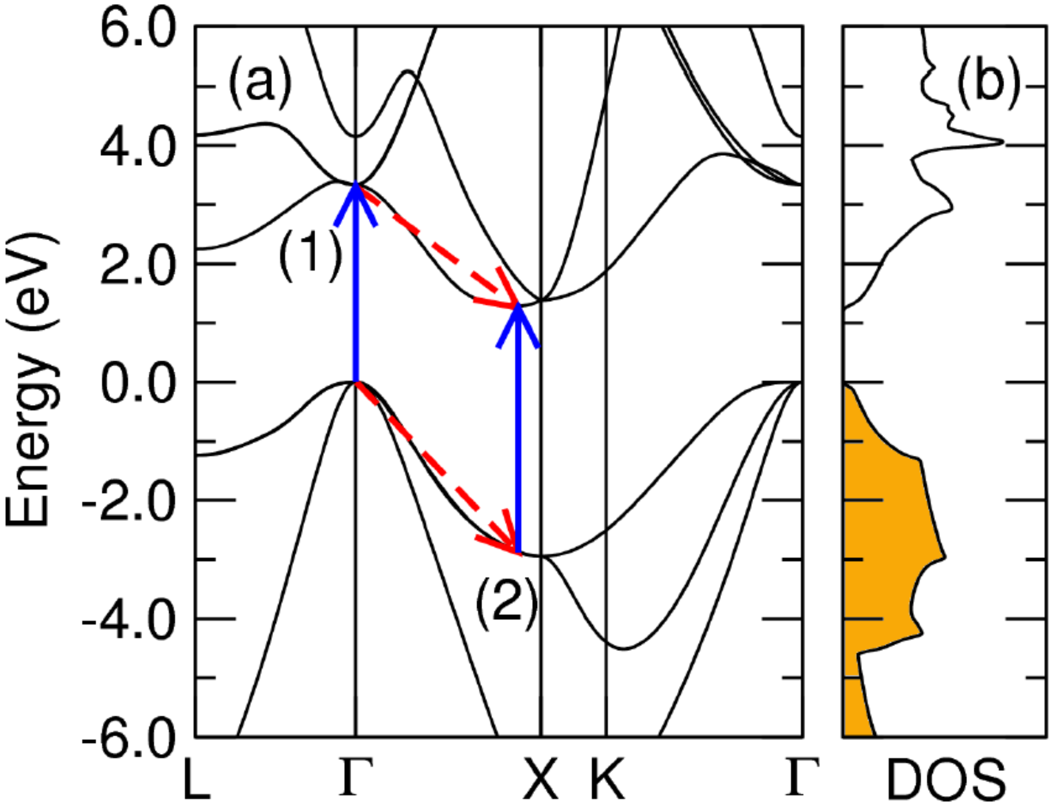

Figure 8.1: (a) Quasiparticle band structure of silicon calculated within the GW approximation and interpolated with the Wannier formalism. The arrows indicate the lowest-energy phonon-assisted optical absorption processes across the indirect band gap. Solid lines denote optical transitions, while dashed lines correspond to electron-phonon scattering events. The two terms, $\boldsymbol{S}_1$ and $\boldsymbol{S}_2$, of Eq. 8.1 are represented by paths (1) and (2) respectively. (b) Density of electronic states versus the quasiparticle energy. The occupied bands have been highlighted.

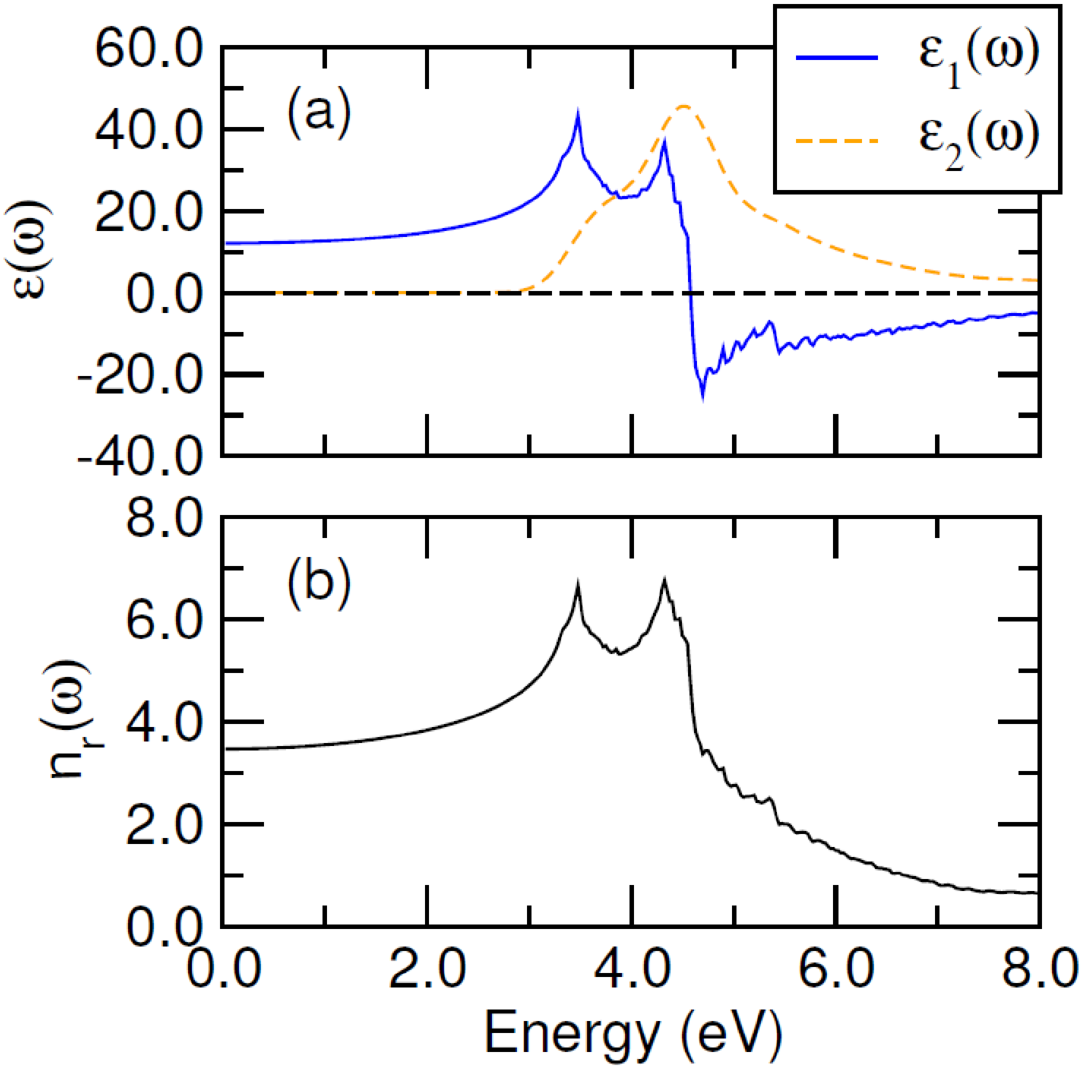

Figure 8.2: (a) Real and imaginary part of the dielectric fucntion of silicon. (b) Index of refraction.

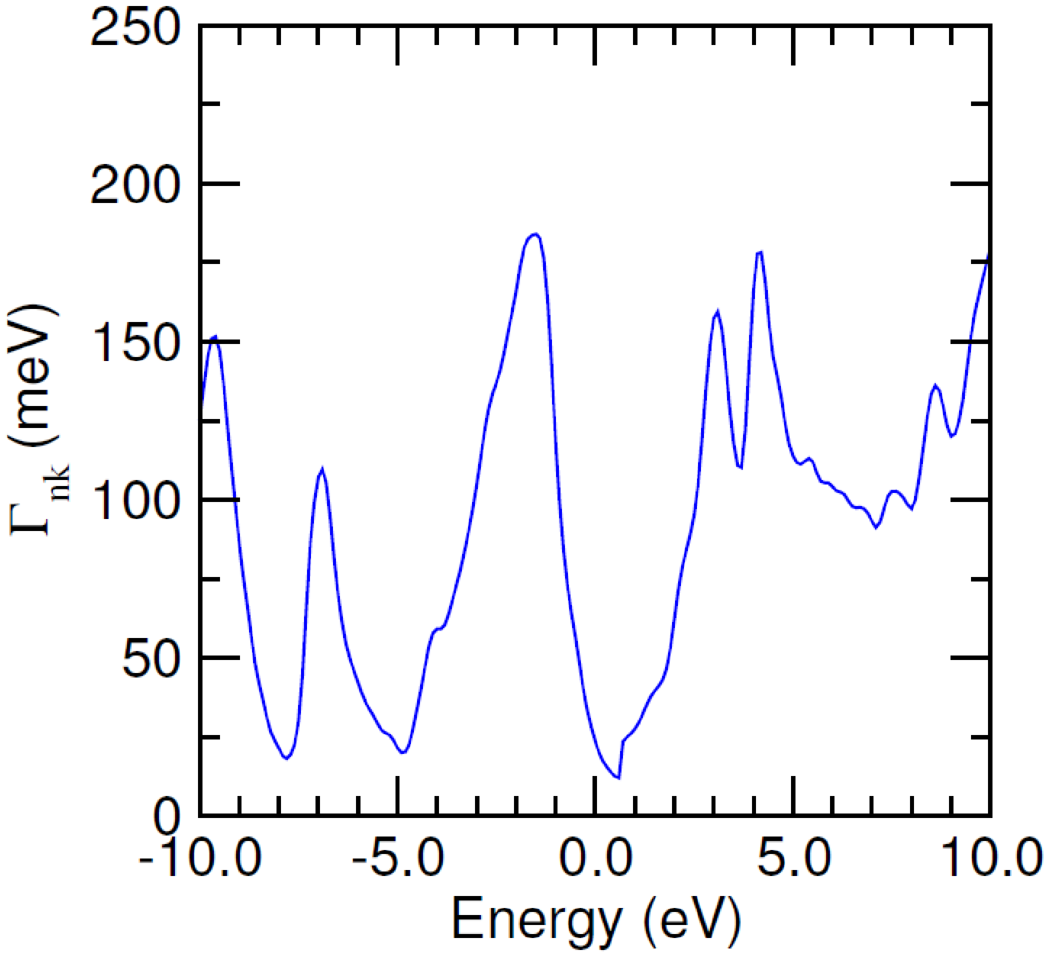

Figure 8.3: Imaginary part of the quasiparticle energies due to the electron-phonon interaction as a function of the real quasiparticle energy referenced to the top of the valence band.

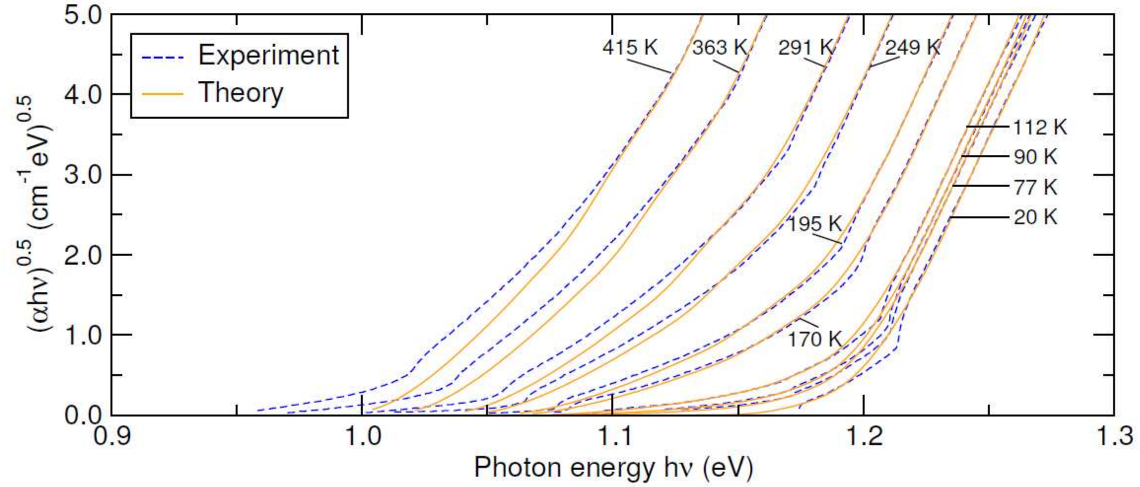

Figure 8.4: Onset of the phonon-assisted optical absorption in silicon, as a function of photon energy and temperature. The theoretical results (solid lines) are in good agreement with experiment (dashed lines). Experimental data are from Ref.

first-principles method is presently available to guarantee a more accurate result. Moreover, finite-temperature effects on the eigenvalues, which we have not considered explicitly, account for the remaining difference. The only temperature dependence we considered is for the Bose occupations of the phonon modes which primarily affects the phonon-absorption contribution to $\alpha(\omega)$. However, the temperature dependence of the quasiparticle energies of silicon, arising from lattice expansion and the electron-phonon band-gap renormalization [172, 173], leads to a gap decrease of approximately 0.1 eV in the range 0 – 400 K [174]. The two effects combined explain the need for and the value of the rigid horizontal shift of the theoretical data to lower energies.

Although excitonic effects, arising from the electron-hole interaction, are potentially important for optical processes and in general affect the direct absorption spectra even for photon energies far from the absorption edge[162], we found that they are not as important for the case of indirect absorption. Sharp features that appear at low temperatures near the onset of indirect absorption have been attributed to excitonic effects[170, 175]. Our calculations, however, are based on quasiparticle theory and do not account for the electron-hole interaction that gives rise to these excitonic features. Nevertheless, our calculated absorption spectra are in very good quantitative agreement with experimental data, pointing to a weaker role of the electron-hole Coulomb interaction for the case of indirect optical transitions. This is probably because of the fact that the band-extrema wavefunctions in indirect-gap materials are located at different points of the BZ and hence the wavefunction overlap, which determines the magnitude of the Coulomb interaction between them, is small. Therefore, the phonon-assisted spectra can to a large extend be explained at the quasiparticle level of theory, without the need to account for excitonic effects.

In conclusion, we used a Wannier-Fourier interpolation technique to calculate the phonon-assisted optical absorption spectra of silicon at the quasiparticle level. The calcu-

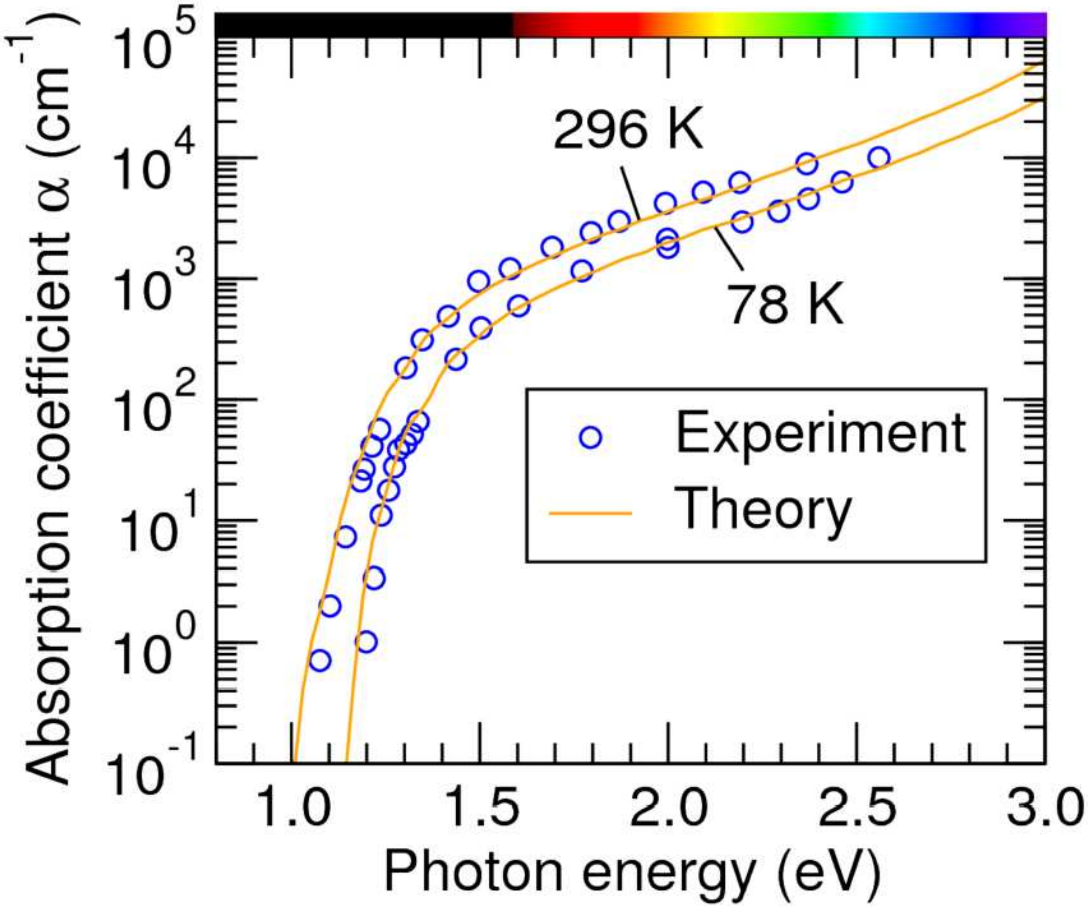

Figure 8.5: Calculated (solid lines) and experimental (circles) absorption coefficient of silicon in the energy range between the indirect and direct gaps, for two temperatures. Experimental data are from Ref. [171].

lated spectra are in very good agreement with experimental measurements, both near the absorption onset and in the spectral region between the indirect and direct band gaps for any lattice temperature. The computational formalism is quite general and can be used to study both the fundamental physics of indirect absorption, as well as the phonon-assisted optical properties of technologically important materials for optoelectronic applications.

Bibliography

[1] C. Fiolhais, F. Nogueira, and M. Marques. *A Primer in Density Functional Theory.* Springer-Verlag, Berlin, 2003.

[2] R. M. Martin. *Electronic Structure: Basic Theory and Practical Methods.* Cambridge University Press, 2004.

[3] S. Baroni, S. d. Gironcoli, A. Dal Corso, and P. Giannozzi. Phonons and related crystal properties from density-functional perturbation theory. *Reviews of Modern Physics*, 73:515–562, 2001.

[4] S. Baroni, P. Giannozzi, and A. Testa. Green's function approach to linear response in solids. *Phys. Rev. Lett.*, 58(18):1861–1864, 1987.

[5] E. Zein. *Sov. Phys. Solid State*, 26:1825, 1984.

[6] M. Tinkham. *Introcution to Superconductivity.* Dover, New York, 1996.

[7] J.R. Schrieffer. *Theory of Superconductivity.* Benjamin, New York, 1962.

[8] G. Grimvall. *The Electron-Phonon Interaction in Metals.* North Holland, New York, 1981.

[9] J. P. Carbotte. Properties of boson-exchange superconductors. *Rev. Mod. Phys.*, 62(4):1027–1157, Oct 1990.

[10] P. Hohenberg and W. Kohn. Inhomogeneous Electron Gas. *Phys. Rev.*, 136(3B):B864–B871, Nov 1964.

[11] W. Kohn and L. J. Sham. Self-Consistent Equations Including Exchange and Correlation Effects. *Phys. Rev.*, 140(4A):A1133–A1138, Nov 1965.

[12] M. Born and R. Oppenheimer. *Ann. D. Phys.*, 84:457, 1927.

[13] R. P. Feynman. Forces in Molecules. *Phys. Rev.*, 56(4):340–343, Aug 1939.

[14] H. K. Onnes. On the Sudden Rate at Which the Resistance in Mercury Disappears. *Comm. Phys. Lab. Univ. Leiden.*, 119, 1911.

[15] H. Frohlich. Theory of the superconducting state. *Physical Review*, 79:477, 1950.

[16] D. Pines. *The Many-Body Problem.* Benjamin, New York, 1962.

[17] J. Bardeen, L. N. Cooper, and J. R. Schrieffer. Theory of Superconductivity. *Phys. Rev.*, 108(5):1175–1204, Dec 1957.

[18] J. Bardeen, L. N. Cooper, and J. R. Schrieffer. Microscopic Theory of Superconductivity. *Phys. Rev.*, 106(1):162–164, Apr 1957.

[19] A. Damascelli, Z. Hussain, and Z.-X. Shen. Angle-resolved photoemission studies of the cuprate superconductors. *Reviews of Modern Physics*, 75(2):473–541, Apr 2003.

[20] W. L. McMillan. Transition Temperature of Strong-Coupled Superconductors. *Physical Review*, 167(2):331–344, Mar 1968.

[21] N. F. Mott. *Proceedings of the Physical Society of London*, 46, 1934.

[22] K. C. D. MacDonald. *Thermoelectricity: An Introduction to the Principles.* Wiley, New York, 1962.

[23] W. Kohn. Image of the Fermi Surface in the Vibration Spectrum of a Metal. *Physical Review Letters*, 2(9):393–394, May 1959.

[24] R. E. Peierls. *Quantum Theory of Solids.* Clarendon, Oxford, 1964.

[25] L. Pintschovius. Electron phonon coupling effects explored by inelastic neutron scattering. *physica status solidi (b)*, 242:30, 2004.

[26] M. Cardona and M. L. W. Thewalt. Isotope effects on the optical spectra of semiconductors. *Reviews of Modern Physics*, 77(4):1173–1224, Nov 2005.

[27] P. K. Lam, M. M. Dacorogna, and M. L. Cohen. Self-consistent calculation of electron-phonon couplings. *Physical Review B*, 34(8):5065–5069, Oct 1986.

[28] J. Ihm, A. Zunger, and M. L. Cohen. Momentum-space formalism for the total energy of solids. *Journal of Physics C: Solid State Physics*, 12(21):4409–4422, 1979.

[29] D. M. Ceperley and B. J. Alder. Ground State of the Electron Gas by a Stochastic Method. *Physical Review Letters*, 45(7):566–569, Aug 1980.

[30] P. Giannozzi, S. Baroni, N. Bonini, M. Calandra, R. Car, C. Cavazzoni, D. Ceresoli, G. L. Chiarotti, M. Cococcioni, I. Dabo, A. Dal Corso, S. de Gironcoli, S. Fabris, G. Fratesi, R. Gebauer, U. Gerstmann, C. Gougoussis, A. Kokalj, M. Lazzeri, L. Martin-Samos, N. Marzari, F. Mauri, R. Mazzarello, S. Paolini, A. Pasquarello, L. Paulatto, C. Sbraccia, S. Scandolo, G. Sclauzero, A. P. Seitsonen, A. Smogunov, P. Umari, and R. M. Wentzcovitch. QUANTUM ESPRESSO: a modular and open-source software project for quantum simulations of materials. *Journal of Physics: Condensed Matter*, 21(39):395502 (19pp), 2009.

[31] F. Giustino, M. L. Cohen, and S. G. Louie. Electron-phonon interaction using Wannier functions. *Physical Review B*, 76(16):165108, 2007.

[32] N. Marzari and D. Vanderbilt. Maximally localized generalized Wannier functions for composite energy bands. *Physical Review B*, 56(20):12847–12865, Nov 1997.

[33] I. Souza, N. Marzari, and D. Vanderbilt. Maximally localized Wannier functions for entangled energy bands. *Physical Review B*, 65(3):035109, Dec 2001.

[34] J. R. Yates, X. Wang, D. Vanderbilt, and I. Souza. Spectral and Fermi surface properties from Wannier interpolation. *Physical Review B*, 75(19):195121, May 2007.

[35] X. Wang, D. Vanderbilt, J. R. Yates, and I. Souza. Fermi-surface calculation of the anomalous Hall conductivity. *Physical Review B*, 76(19):195109, Nov 2007.

[36] X. Wang, J. R. Yates, I. Souza, and D. Vanderbilt. Ab initio calculation of the anomalous Hall conductivity by Wannier interpolation. *Physical Review B*, 74(19):195118, 2006.

[37] D. R. Hamann and D. Vanderbilt. Maximally localized Wannier functions for GW quasiparticles. *Physical Review B*, 79(4):045109, Jan 2009.

[38] F. Giustino, J. R. Yates, I. Souza, M. L. Cohen, and S. G. Louie. Electron-Phonon Interaction via Electronic and Lattice Wannier Functions: Superconductivity in Boron-Doped Diamond Reexamined. *Physical Review Letters*, 98(4):047005, 2007.

[39] C.-H. Park, F. Giustino, M. L. Cohen, and S. G. Louie. Velocity Renormalization and Carrier Lifetime in Graphene from the Electron-Phonon Interaction. *Physical Review Letters*, 99(8):086804, Aug 2007.

[40] C.-H. Park, F. Giustino, J. L. McChesney, A. Bostwick, T. Ohta, E. Rotenberg, M. L. Cohen, and S. G. Louie. Van Hove singularity and apparent anisotropy in the electron-phonon interaction in graphene. *Physical Review B*, 77(11):113410, Mar 2008.

[41] J. Noffsinger, F. Giustino, S. G. Louie, and M. L. Cohen. First-principles study of superconductivity and Fermi-surface nesting in ultrahard transition metal carbides. *Physical Review B*, 77(18):180507, May 2008.

[42] C.-H. Park, F. Giustino, C. D. Spataru, M. L. Cohen, and S. G. Louie. First-Principles Study of Electron Linewidths in Graphene. *Physical Review Letters*, 102(7):076803, Feb 2009.

[43] J. Noffsinger, F. Giustino, S. G. Louie, and M. L. Cohen. Origin of superconductivity in boron-doped silicon carbide from first principles. *Physical Review B*, 79(10):104511, Mar 2009.

[44] F. Giustino, M. L. Cohen, and S. G. Louie. Small phonon contribution to the photoemission kink in the copper oxide superconductors. *Nature (London)*, 452:975, 2008.

[45] C.-H. Park, F. Giustino, M. L. Cohen, and S. G. Louie. ElectronPhonon Interactions in Graphene, Bilayer Graphene, and Graphite. *Nano Lett.*, 8(12):4229, 2008.

[46] C.-H. Park, F. Giustino, C. D. Spataru, M. L. Cohen, and S. G. Louie. Angle-Resolved Photoemission Spectra of Graphene from First-Principles Calculations. *Nano Lett.*, 9(12):4234, 2009.

[47] A. A. Mostofi, J. R. Yates, Y.-S. Lee, I. Souza, D. Vanderbilt, and N. Marzari. wannier90: A tool for obtaining maximally-localised Wannier functions. *Computer Physics Communications*, 178(9):685 – 699, 2008.

[48] M. Fuchs and M. Scheffler. Ab initio pseudopotentials for electronic structure calculations of poly-atomic systems using density-functional theory. *Computer Physics Communications*, 119:67–98, 1999.

[49] M. L. Cohen. Pseudopotentials and total energy calculations. *Physica Scripta*, 5(T1), 1982.

[50] N. Troullier and J. L. Martins. Efficient pseudopotentials for plane-wave calculations. *Physical Review B*, 43(3):1993–2006, Jan 1991.

[51] J. P. Perdew and A. Zunger. Self-interaction correction to density-functional approximations for many-electron systems. *Physical Review B*, 23(10):5048–5079, May 1981.

[52] D. Vanderbilt. Soft self-consistent pseudopotentials in a generalized eigenvalue formalism. *Physical Review B*, 41(11):7892–7895, Apr 1990.

[53] P. B. Allen and B. Mikovic. In H Ehrenreich, F Seitz, and D Turnbull, editors, *Solid State Phys*, volume 32, page 1. Academic, New York, 1982.

[54] A. B. Migdal. *JETP*, 34:1438, 1958.

[55] E. Kioupakis, P. Rinke, A. Schleife, F. Bechstedt, and C. G. Van de Walle. Free-carrier absorption of Nitrides from first-principles. *Phys. Rev. B*, 81(24):241201, 2010.

[56] S. Y. Savrasov and D. Y. Savrasov. Electron-phonon interactions and related physical properties of metals from linear-response theory. *Physical Review B*, 54, 1996.

[57] J. D. Cloizeaux. Analytical Properties of n-Dimensional Energy Bands and Wannier Functions. *Physical Review*, 135(3A):A698–A707, Aug 1964.

[58] G. Nenciu. Existence of the Exponentially Localised Wannier Functions. *Commun. Math. Phys.*, 91:81–85, 1983.

[59] M. Unser. Sampling—50 Years After Shannon. *Proceedings of the IEEE*, 88(4):569–587, April 2000.

[60] V. Perebeinos, J. Tersoff, and P. Avouris. Effect of Exciton-Phonon Coupling in the Calculated Optical Absorption of Carbon Nanotubes. *Physical Review Letters*, 94(2):027402, Jan 2005.

[61] W. Lochmann and A. Haug. Phonon-assisted Auger recombination in Si with direct calculation of the overlap integrals. *Solid State Communications*, 35(7):553 – 556, 1980.

[62] W. L. McMillan and J. M. Rowell. Lead Phonon Spectrum Calculated from Superconducting Density of States. *Physical Review Letters*, 14(4):108–112, Jan 1965.

[63] P. B. Allen and M. L. Cohen. Pseudopotential Calculation of the Mass Enhancement and Superconducting Transition Temperature of Simple Metals. *Physical Review*, 187(2):525–538, Nov 1969.

[64] R. Knorr and N. Barth. Electron tunneling into disordered thin films. *J. Low Temp. Phys.*, 4:469, 1971.

[65] J. P. Franck, W. J. Keeler, and T. M. Wu. Pressure-dependence of the phonon spectrum of Pb from tunneling measurements. *Solid State Commun.*, 7(5):483 – 486, 1969.

[66] J. Noffsinger and M. L. Cohen. First-principles calculation of the electron-phonon coupling in ultrathin Pb superconductors: Suppression of the transition temperature by surface phonons. *Physical Review B*, 81(21):214519, Jun 2010.

[67] P. B. Allen and R. C. Dynes. Transition temperature of strong-coupled superconductors reanalyzed. *Physical Review B*, 12(3):905–922, 1975.

[68] K. S. Novoselov, D. Jiang, F. Schedin, T. J. Booth, V. V. Khotkevich, S. V. Morozov, and A. K. Geim. Two-dimensional atomic crystals. *Proc. Natl. Acad. Sci. U.S.A.*, 102(10):451, 2005.

[69] K. S. Novoselov, A. K. Geim, S. V. Morozov, D. Jiang, M. I. Katsnelson, I. V. Grigorieva, S. V. Dubonos, and A. A. Firsov. Two-dimensional gas of massless Dirac fermions in graphene. *Nature (London)*, 438(197):7065, 2005.

[70] Y. Zhang, Y.-W. Tan, H. L. Stormer, and P. Kim. Experimental observation of the quantum Hall effect and Berry's phase in graphene. *Nature (London)*, 438(201):7065, 2005.

[71] A. Bostwick, T. Ohta, T. Seyller, K. Horn, and E. Rotenberg. Quasiparticle dynamics in graphene. *Nature Physics*, 3:36, 2007.

[72] Z.-A. Ren, J. Kato, T. Muranaka, J. Akimitsu, M. Kriener, and Y. Maeno. Superconductivity in Boron-doped SiC. *Journal of the Physical Society of Japan*, 76(10):103710, 2007.

[73] E. A. Ekimov, V. A. Sidorov, E. D. Bauer, N. N. Mel'nik, N. J. Curro, J. D. Thompson, and S. M. Stishov. Superconductivity in Diamond. *Nature (London)*, 428(6982):542, April 2004.

[74] E. R. Margine and X. Blase. Ab initio study of electron-phonon coupling in boron-doped SiC. *Appl. Phys. Lett.*, 93:192510, 2007.

[75] M. L. Cohen. The Existence of a Superconducting State in Semiconductors. *Reviews of Modern Physics*, 36(1):240–243, Jan 1964.

[76] K.-W. Lee and W. E. Pickett. Superconductivity in Boron-Doped Diamond. *Physical Review Letters*, 93(23):237003, Nov 2004.

[77] L. Boeri, J. Kortus, and O. K. Andersen. Three-Dimensional MgB_2-Type Superconductivity in Hole-Doped Diamond. *Physical Review Letters*, 93(23):237002, Nov 2004.

[78] Y. Ma, J. S. Tse, T. Cui, D. D. Klug, L. Zhang, Y. Xie, Y. Niu, and G. Zou. First-principles study of electron-phonon coupling in hole- and electron-doped diamonds in the virtual crystal approximation. *Physical Review B*, 72(1):014306, Jul 2005.

[79] X. Blase, Ch. Adessi, and D. Connétable. Role of the Dopant in the Superconductivity of Diamond. *Physical Review Letters*, 93(23):237004, Nov 2004.

[80] H. J. Choi, D. Roundy, H. S., M. L. Cohen, and S. G. Louie. The origin of the anomalous superconducting properties of MgB2. *Nature (London)*, 418(6899):758, 2002.

[81] L. N. Oliveira, E. K. U. Gross, and W. Kohn. Density-Functional Theory for Superconductors. *Physical Review Letters*, 60(23):2430–2433, Jun 1988.

[82] O. J. Wacker, R. Kümmel, and E. K. U. Gross. Time-Dependent Density-Functional Theory for Superconductors. *Physical Review Letters*, 73(21):2915–2918, Nov 1994.

[83] A. R. Beattie and P. T. Landsberg. Auger effect in semiconductors. *Proc. R. Soc. London, Ser. A*, 249(16), 1959.

[84] J. Nagamatsu, N. Nakagawa, T. Muranaka, Y. Zenitani, and J. Akimitsu. Superconductivity at 39K in magnesium diboride. *Nature (London)*, 410:63–64, 2001.

[85] R.O. Jones and O. Gunnarsson. The density functional formalism, its applications and prospects. *Reviews of Modern Physics*, 61:689–716, 1989.

[86] S. Yamanaka, K. i. Hotehama, and H. Kawaji. Superconductivity at 25.5 K in electron-doped layerd hafnium nitride. *Nature Physics*, 392:580–582, 1998.

[87] T. E. Weller, M. Ellerby, S. S. Saxena, R. P. Smith, and N. T. Skipper. Superconductivity in the intercalated graphite compounds C6Yb and C6Ca. *Nature Physics*, 1:39–41, 2005.

[88] L. E. Toth. *Transition Metal Carbides and Nitrides.* Academic Press: New York, 1971.

[89] S.-H. Jhi, J. Ihm, S.G. Louie, and M.L. Cohen. Electronic Mechanism of Hardness Enhancement in Transition-Metal Carbonitrides. *Nature (London)*, 399:132–143, 1999.

[90] A. Y. Liu, R. M. Wentzcovitch, and M. L. Cohen. Structural and electronic properties of WC. *Physical Review B*, 38(14):9483–9489, Nov 1988.

[91] W. Hanke, J. Hafner, and H. Bilz. Phonon Anomalies and Superconductivity in Transition-Metal Compounds. *Physical Review Letters*, 37(23):1560–1564, Dec 1976.

[92] W. Weber. Lattice Dynamics of Transition-Metal Carbides. *Physical Review B*, 8(11):5082–5092, Dec 1973.

[93] P. Allen and M.L. Cohen. Superconductivity and Phonon Softening. *Physical Review Letters*, 29:937–940, 1972.

[94] H. R. Zeller. Effect of Lattice Instabilities on Superconducting and Other Properties in TaC_x. *Physical Review B*, 5(5):1813–1817, Mar 1972.

[95] B.M. Klein, L.L. Boyer, and D.A. Papaconstantopoulos. On the Relationship Between the Phonon Anomalies and the *ab initio* Calclated Fermi Surfaces of TaC and NbC. *Solid State Communications*, 20:937–940, 1976.

[96] B.M. Klein and D. A. Papaconstantopoulos. Electron-Phonon Interaction and Superconductivity in Transition Metals and Transition Metal-Carbides. *Physical Review Letters*, 32:937–940, 1974.

[97] H.G. Smith and W. Glaser. Phonon Spectra in TaC and HfC. *Physical Review Letters*, 25:937–940, 1970.

[98] E.I. Isaev, R. Ahuja, I. Simak, A.I. Lichtenstein, Yu. Kh. Vekilov, B. Johansson, and I.A. Abrikosov. Anomalously enhanced superconductivity and *ab initio* lattice dynamics in transition metal carbides and nitrides. *Physical Review B*, 72:937–940, 2005.

[99] W. Reichardt L. Pintschovius and B. Scheerer. Lattice dynamics of TiC. *Journal of Physics C: Solid State Physics*, 11(8):1557–1562, 1978.

[100] M. Gupta and A.J. Freeman. Role of electronic structure on obsered phonon anomalies of transition-metal carbides. *Physical Review B*, 14, 1976.

[101] N. Wright, A. Horsfall, and K. Vassilevski. Prospoects for SiC electronics and sensors. *Materials Today*, 11(1-2):16, 2008.

[102] W. J. Choyke, H. Matsunami, and G. Pensl. *Silicon Carbide: Recent Major Advances.* Springer-Verlag, Berlin, 2004.

[103] Z.-A. Ren, J. Kato, T. Muranaka, J. Akimitsu, M. Kriener, and Y. Maeno. Superconductivity in Boron-doped SiC. *J. Phys. Soc. Japan*, 76(10):103710, Oct 2007.

[104] E. Bustarret, C. Marcenat, P. Achatz, J. Kacmarcik, F. Levy, A. Huxley, L. Ortega, E. Bourgeois, X. Blase, D. Debarre, and J. Boulmer. Superconductivity in doped cubic silicon. *Nature (London)*, 444(7118):465, November 2006.

[105] K. Ishizaka, R. Eguchi, S. Tsuda, T. Yokoya, A. Chainani, T. Kiss, T. Shimojima, T. Togashi, S. Watanabe, C.-T. Chen, C. Q. Zhang, Y. Takano, M. Nagao, I. Sakaguchi, T. Takenouchi, H. Kawarada, and S. Shin. Observation of a Superconducting Gap in Boron-Doped Diamond by Laser-Excited Photoemission Spectroscopy. *Physical Review Letters*, 98(4):047003, 2007.

[106] C.J. Wort and R. S. Balmer. Diamond as an electronic material. *Materials Today*, 11:22, 2008.

[107] Q. Wahab, T. Kimoto, A. Ellison, C. Hallin, M. Tuominen, R. Yakimova, A. Henry, J. P. Bergman, and E. Janzn. A 3 kV Schottky barrier diode in 4H-SiC. *Appl. Phys. Lett.*, 72:445, 1998.

[108] L. G. Matus, J. A. Powell, and C. S. Salupo. Highvoltage 6HSiC pn junction diodes. *Appl. Phys. Lett.*, 59:1770, 1991.

[109] P. Achatz, J. Pernot, C. Marcenat, J. Kacmarcik, G. Ferro, and E. Bustarret. Doping-induced metal-insulator transition in aluminum-doped 4H silicon carbide. *Appl. Phys. Lett.*, 92:072103, 2008.

[110] J. Serrano, J. Strempfer, M. Cardona, M. Schwoerer-Bohning, H. Requardt, M. Lorenzen, B. Stojetz, P. Pavone, and W.J. Choyke. Determination of the phonon dispersion of zinc blende(3C) silicon carbide by inelastic x-ray scattering. *Appl. Phys. Lett.*, 80(23):4360–4362, 2002.

[111] M. Hoesch, T. Fukuda, J. Mizuki, T. Takenouchi, H. Kawarada, J. P. Sutter, S. Tsutsui, A. Q. R. Baron, M. Nagao, and Y. Takano. Phonon softening in superconducting diamond. *Physical Review B*, 75(14):140508, Apr 2007.

[112] M. Kriener, Y. Maeno, T. Oguchi, Z.-A. Ren, J. Kato, T. Muranaka, and J. Akimitsu. Specific heat and electronic states of superconducting boron-doped silicon carbide. *Physical Review B*, 78(2):024517, Jul 2008.

[113] P. Achatz, J. Pernot, C. Marcenat, G. Ferro J. Kacmarci and, and E. Bustarret. Doping-induced metal-insulator transition in aluminum-doped 4H silicon carbide. *Appl. Phys. Lett.*, 92:072103, 2008.

[114] Y. Kamihara, T. Watanabe, M. Hirano, and H. Hosono. Iron-Based Layered Superconductor La[O1-xFx]FeAs (x = 0.050.12) with Tc = 26 K. *Journal of the American Chemical Society*, 130(11):3296–3297, 2008.

[115] L. Boeri, O. V. Dolgov, and A. A. Golubov. Is LaFeAsO$_{1-x}$F$_x$ an Electron-Phonon Superconductor? *Physical Review Letters*, 101(2):026403, Jul 2008.

[116] M. Le Tacon, M. Krisch, A. Bosak, J.-W. G. Bos, and S. Margadonna. Phonon density of states in NdFeAsO$_{1-x}$F$_x$. *Physical Review B*, 78(14):140505, Oct 2008.

[117] D. J. Singh and M.-H. Du. Density Functional Study of LaFeAsO$_{1-x}$F$_x$: A Low Carrier Density Superconductor Near Itinerant Magnetism. *Physical Review Letters*, 100(23):237003, Jun 2008.

[118] W. E. Pickett. Electronic structure of the high-temperature oxide superconductors. *Reviews of Modern Physics*, 61(2):433–512, Apr 1989.

[119] M. Jia, H. Lan-Tian, Z. Gui-Yao, W. Kang, and C. Chao. Small-Pitch Kagome Hollow-Core Photonic Crystal Fibre. *Chinese Physics Letters*, 25(8):2860, 2008.

[120] M. L. Cohen, M. Schlüter, J. R. Chelikowsky, and S. G. Louie. Self-consistent pseudopotential method for localized configurations: Molecules. *Physical Review B*, 12(12):5575–5579, Dec 1975.

[121] J. Ihm and M. L. Cohen. Equilibrium properties and the phase transition of grey and white tin. *Physical Review B*, 23(4):1576–1579, Feb 1981.

[122] C.-H. Lee, A. Iyo, H. Eisaki, H. Kito, M. T. Fernandez-Diaz, T. Ito, K. Kihou, H. Matsuhata, M. Braden, and K. Yamada. Effect of Structural Parameters on Superconductivity in Fluorine-Free $\mathrm{LnFeAsO}_{1-y}$ $(\mathrm{Ln} = \mathrm{La}, \mathrm{Nd})$. *Journal of the Physical Society of Japan*, 77(8):083704, 2008.

[123] S. Y. Savrasov, D. Y. Savrasov, and O. K. Andersen. Linear-response calculations of electron-phonon interactions. *Physical Review Letters*, 72(3):372–375, Jan 1994.

[124] R. Bauer, A. Schmid, P. Pavone, and D. Strauch. Electron-phonon coupling in the metallic elements Al, Au, Na, and Nb: A first-principles study. *Physical Review B*, 57(18):11276–11282, May 1998.

[125] D. B. Haviland, Y. Liu, and A. M. Goldman. Onset of superconductivity in the two-dimensional limit. *Physical Review Letters*, 62(18):2180–2183, May 1989.

[126] B. G. Orr, H. M. Jaeger, and A. M. Goldman. Transition-Temperature Oscillations in Thin Superconducting Films. *Physical Review Letters*, 53(21):2046–2049, Nov 1984.

[127] J. M. Blatt and C. J. Thompson. Shape Resonances in Superconducting Thin Films. *Physical Review Letters*, 10(8):332–334, Apr 1963.

[128] M. Strongin, R. S. Thompson, O. F. Kammerer, and J. E. Crow. Destruction of Superconductivity in Disordered Near-Monolayer Films. *Physical Review B*, 1(3):1078–1091, Feb 1970.

[129] C. M. Wei and M. Y. Chou. Theory of quantum size effects in thin Pb(111) films. *Physical Review B*, 66(23):233408, Dec 2002.

[130] S. Qin, J. Kim, Q. Niu, and C.-K. Shih. Superconductivity at the Two-Dimensional Limit. *Science*, 324(5932):1314–1317, 2009.

[131] T. Zhang, P. Cheng, W.-J. Li, Y.-J. Sun, G. Wang, X.-G. Zhu, K. He, L. Wang, X. Ma, X. Che, Y. Wang, Y. Liu, H.-Q. Lin, J.-F. Jia, and Q.-K. Xue. Superconductivity in one-atomic-layer metal films grown on Si(111). *Nature Physics*, 6:104, 2010.

[132] Y. Guo, Y.-F. Zhang, X.-Y. Bao, T.-Z. Han, Z. Tang, L.-X. Zhang, W.-G. Zhu, E. G. Wang, Q. Niu, Z. Q. Qiu, J.-F. Jia, Z.-X. Zhao, and Q.-K. Xue. Superconductivity Modulated by Quantum Size Effects. *Science*, 306(5703):1915–1917, 2004.

[133] M. M. Ozer, Y. Jia, Z. Zhang, J. R. Thompson, and H. H. Weitering. Tuning the Quantum Stability and Superconductivity of Ultrathin Metal Alloys. *Science*, 316:1594, 2007.

[134] D. Eom, S. Qin, M.-Y. Chou, and C. K. Shih. Persistent Superconductivity in Ultrathin Pb Films: A Scanning Tunneling Spectroscopy Study. *Physical Review Letters*, 96(2):027005, Jan 2006.

[135] K. Wang, X. Zhang, M. M. T. Loy, T.-C. Chiang, and X. Xiao. Pseudogap Mediated by Quantum-Size Effects in Lead Islands. *Physical Review Letters*, 102(7):076801, Feb 2009.

[136] T. Nishio, T. An, A. Nomura, K. Miyachi, T. Eguchi, H. Sakata, S. Lin, N. Hayãshi, N. Nakai, M. Machida, and Y. Hasegawa. Superconducting Pb Island Nanostructures Studied by Scanning Tunneling Microscopy and Spectroscopy. *Physical Review Letters*, 101(16):167001, Oct 2008.

[137] N. D. Mermin and H. Wagner. Absence of Ferromagnetism or Antiferromagnetism in One- or Two-Dimensional Isotropic Heisenberg Models. *Physical Review Letters*, 17(22):1133–1136, Nov 1966.

[138] M. L. Cohen, M. Schlüter, J. R. Chelikowsky, and S. G. Louie. Self-consistent pseudopotential method for localized configurations: Molecules. *Physical Review B*, 12(12):5575–5579, Dec 1975.

[139] A. A. Khajetoorians, W. Zhu, J. Kim, S. Qin, H. Eisele, Z. Zhang, and C.-K. Shih. Adsorbate-induced restructuring of Pb mesas grown on vicinal Si(111) in the quantum regime. *Physical Review B*, 80(24):245426, Dec 2009.

[140] U. Schwingenschlögl and I. A. Shelykh. Quantum size effects in Pb layers with absorbed Kondo adatoms: Determination of the exchange coupling constant. *Physical Review B*, 80(3):033101, Jul 2009.

[141] F. Yndurain and M. P. Jigato. First Principles Calculation of Localized Surface Phonons and Electron-Phonon Interaction at Pb(111) Thin Films. *Physical Review Letters*, 100(20):205501, May 2008.

[142] C. Brun, I-P. Hong, Fran çois Patthey, I. Yu. Sklyadneva, R. Heid, P. M. Echenique, K. P. Bohnen, E. V. Chulkov, and W.-D. Schneider. Reduction of the Superconducting Gap of Ultrathin Pb Islands Grown on Si(111). *Physical Review Letters*, 102(20):207002, May 2009.

[143] T.-L. Chan, J. R. Chelikowsky, K.-M. Ho, C.-Z. Wang, and S. Zhang. The effect of interface on quantum confinement and electronic structure across Pb/Si(111) junction. to be published.

[144] J. M. Kosterlitz and D. J. Thouless. Ordering, metastability and phase transitions in two-dimensional systems. *J. Phys. C*, 6(7):1181, 1973.

[145] A. Yazdani. Thin Films: Lean and mean superconductivity. *Nat. Phys.*, 2:151–152, 2006.

[146] N. D. Mermin and H. Wagner. Absence of Ferromagnetism or Antiferromagnetism in One- or Two-Dimensional Isotropic Heisenberg Models. *Physical Review Letters*, 17(22):1133–1136, Nov 1966.

[147] R. Heid, K.-P. Bohnen, I. Yu. Sklyadneva, and E. V. Chulkov. Effect of spin-orbit coupling on the electron-phonon interaction of the superconductors Pb and Tl. *Phys. Rev. B*, 81(17):174527, May 2010.

[148] R. Szczsniak. On the Coulomb pseudopotential for Al and Pb superconductors. *Phys. Status Solidi B*, 244(7):2538–2542, 2007.

[149] B. Mitrović, H. G. Zarate, and J. P. Carbotte. The ratio $\frac{2\Delta_0}{k_B T_c}$ within Eliashberg theory. *Physical Review B*, 29(1):184–190, Jan 1984.

[150] J. Noffsinger, F. Giustino, B. D. Malone, C.-H. Park, S. G. Louie, and M. L. Cohen. EPW: A program for calculating the electron-phonon coupling using maximally localized Wannier functions. *Computer Physics Communications*, 181(12):2140 – 2148, 2010.

[151] C. Kumpf, O. Bunk, J. H. Zeysing, M. M. Nielsen, M. Nielsen, R. L. Johnson, and R. Feidenhans'l. Structural study of the commensurate-incommensurate low-temperature phase transition of Pb on Si(111). *Surface Science*, 448(2-3):L213 – L219, 2000.

[152] M. Rafiee and S. Jalali Asadabadi. Quantum size effects in Pb/Si(111) thin films from density functional calculations. *Computational Materials Science*, 47(2):584 – 592, 2009.

[153] A Eichler, J Wittig, and Z Angew. *Physics*, 25:319, 1968.

[154] H. Kawamura and K. Tachikawa. Measurement of superconductivity under high pressures. *Cryogenics*, 20(10):564 – 566, 1980.

[155] T. M. Wu. Effect of pressure on the transition temperature of Pb. *Physics Letters A*, 30(6):347 – 348, 1969.

[156] P. Vashishta and J. P. Carbotte. Superconductivity in Pb under pressure. *Journal of Low Temperature Physics*, 18:457–466, 1975. 10.1007/BF00116136.

[157] Ricardo R. L. Zucca and Y. R. Shen. Wavelength-Modulation Spectra of Some Semiconductors. *Phys. Rev. B*, 1(6):2668–2676, Mar 1970.

[158] B. Welber, C. K. Kim, Manuel Cardona, and Sergio Rodriguez. Dependence of the indirect energy gap of silicon on hydrostatic pressure. *Solid State Communications*, 17(8):1021 – 1024, 1975.

[159] Lorin X. Benedict, Eric L. Shirley, and Robert B. Bohn. Theory of optical absorption in diamond, Si, Ge, and GaAs. *Phys. Rev. B*, 57(16):R9385–R9387, Apr 1998.

[160] Stefan Albrecht, Lucia Reining, Rodolfo Del Sole, and Giovanni Onida. Ab Initio Calculation of Excitonic Effects in the Optical Spectra of Semiconductors. *Phys. Rev. Lett.*, 80(20):4510–4513, May 1998.

[161] Michael Rohlfing and Steven G. Louie. Electron-Hole Excitations in Semiconductors and Insulators. *Phys. Rev. Lett.*, 81(11):2312–2315, Sep 1998.

[162] Michael Rohlfing and Steven G. Louie. Electron-hole excitations and optical spectra from first principles. *Phys. Rev. B*, 62(8):4927–4944, Aug 2000.

[163] Giovanni Onida, Lucia Reining, and Angel Rubio. Electronic excitations: density-functional versus many-body Green's-function approaches. *Rev. Mod. Phys.*, 74(2):601–659, Jun 2002.

[164] Emmanouil Kioupakis, Murilo L. Tiago, and Steven G. Louie. Quasiparticle electronic structure of bismuth telluride in the *GW* approximation. *Phys. Rev. B*, 82(24):245203, Dec 2010.

[165] F. Bassani and G. Pastori Parravicini. *Electronic States and Optical Transitions in Solids.* Pergamon Press, 1975.

[166] L. Hedin and S. Lundqvist. *Solid State Phys.*, 23:1, 1970.

[167] Mark S. Hybertsen and Steven G. Louie. Electron correlation in semiconductors and insulators: Band gaps and quasiparticle energies. *Phys. Rev. B*, 34(8):5390–5413, Oct 1986.

[168] S. G. Louie. In S. G. Louie and M. L. Cohen, editors, *Conceptual Foundations of Materials: A Standard Model for Ground- and Excited-State Properties*, page 9. Elsevier, Amsterdam, 2006.

[169] Zachary H. Levine and Douglas C. Allan. Linear optical response in silicon and germanium including self-energy effects. *Phys. Rev. Lett.*, 63(16):1719–1722, Oct 1989.

[170] G. G. Macfarlane, T. P. McLean, J. E. Quarrington, and V. Roberts. Fine Structure in the Absorption-Edge Spectrum of Si. *Phys. Rev.*, 111(5):1245–1254, Sep 1958.

[171] Rubin Braunstein, Arnold R. Moore, and Frank Herman. Intrinsic Optical Absorption in Germanium-Silicon Alloys. *Phys. Rev.*, 109(3):695–710, Feb 1958.

[172] P. Lautenschlager, P. B. Allen, and M. Cardona. Temperature dependence of band gaps in Si and Ge. *Phys. Rev. B*, 31(4):2163–2171, Feb 1985.

[173] Feliciano Giustino, Steven G. Louie, and Marvin L. Cohen. Electron-Phonon Renormalization of the Direct Band Gap of Diamond. *Phys. Rev. Lett.*, 105(26):265501, Dec 2010.

[174] H. D. Barber. Effective mass and intrinsic concentration in silicon. *Solid-State Electronics*, 10(11):1039 – 1051, 1967.

[175] K. L. Shaklee and R. E. Nahory. Valley-Orbit Splitting of Free Excitons? The Absorption Edge of Si. *Phys. Rev. Lett.*, 24(17):942–945, Apr 1970.